

---

[All ETDs from UAB](#)

[UAB Theses & Dissertations](#)

---

2021

## Characterization Of Color Centers In Diamond For Laser Applications

Shova Devi Subedi  
*University of Alabama at Birmingham*

Follow this and additional works at: <https://digitalcommons.library.uab.edu/etd-collection>



Part of the [Arts and Humanities Commons](#)

---

### Recommended Citation

Subedi, Shova Devi, "Characterization Of Color Centers In Diamond For Laser Applications" (2021). *All ETDs from UAB*. 930.

<https://digitalcommons.library.uab.edu/etd-collection/930>

This content has been accepted for inclusion by an authorized administrator of the UAB Digital Commons, and is provided as a free open access item. All inquiries regarding this item or the UAB Digital Commons should be directed to the [UAB Libraries Office of Scholarly Communication](#).

CHARACTERIZATION OF COLOR CENTERS IN DIAMOND FOR LASER  
APPLICATIONS

by

SHOVA D SUBEDI

SERGEY B. MIROV, COMMITTEE CHAIR

SHANE AARON CATLEDGE

VLADIMIR V. FEDOROV

PATRICK KUNG

MUHAMMAD MAQBOOL

MARY ELLEN ZVANUT

A DISSERTATION

Submitted to the graduate faculty of The University of Alabama at Birmingham,  
in partial fulfillment of the requirements for the degree of  
Doctor of Philosophy

BIRMINGHAM, ALABAMA

2021

Copyright by  
Shova D Subedi  
2021

# CHARACTERIZATION OF COLOR CENTERS IN DIAMOND FOR LASER APPLICATIONS

SHOVA D SUBEDI

PHYSICS

ABSTRACT

Diamond has been gaining a lot of interest in the field of photonics such as quantum optics, nano-photonics, quantum computation, magnetometry, sensing, laser development, and color center physics as it provides a remarkable platform to combine its non-linear optical properties in conjunction with the unique optical and spin properties of its color centers. Besides that, energetic pulsed lasers operating in the visible to near IR spectral range are mostly obtained from non-linear frequency conversion which is less efficient, expensive, and requires nonlinear crystal with excellent optical quality, a special cut to meet the perfect phase-matching condition. Another alternative is dye lasers but these are less common due to less tunability, the toxicity of the gain medium, and the requirement of high maintenance. Because of the wide band gap and compactness of its crystal structure, diamond serves as a host for several hundreds of color centers. Some of them exhibit excellent optical properties such as stable photoluminescence, long lifetime, high transition cross-section, broad tunability range, and most importantly the photo-thermal and chemical stability. Furthermore, the diamond itself is an unrivaled host with the highest thermal conductivity of any bulk material known. Some of the color centers are very promising for laser applications and lasers based on those centers could span the whole visible to the near-infrared spectral range.

Nitrogen-Vacancy (NV) color centers in diamond are one of the most widely studied solid-state defects, which have received attention in recent years due to their impressive optical and spin characteristics. One of the major challenges for many applications is the photoionization processes of NV centers between negative and neutral charge states. The rate of photoionization depends on the intensity and wavelength of the pump photon. However, there is still no clear understanding of several aspects of these photoionization processes. In addition to spectroscopic characterization, non-linear absorption properties and extent of saturation with pump intensities were studied. The temporal dynamics of saturation and photoionization were examined at different wavelengths using the pump-probe technique and a model describing the photoionization processes was developed.

Another promising color center for laser application is GR1, which is one of the most common but poorly studied centers in diamond. Passive Q-switching of Ruby laser was demonstrated using these centers but a detailed understanding of spectroscopic and laser properties of GR1 in diamond color center crystals is not available. These centers are strongly luminescent, photo-thermo stable, feature broad absorption, and emission bands, and can serve as laser active optical centers and saturable absorbers for passive Q-switching of popular Alexandrite and Ti:Sapphire laser cavities. A detailed study and analysis of spectroscopic and laser properties of these centers were carried out in this work.

Diamond has outstanding Raman properties in comparison to other commonly used Raman gain media. Diamond Raman lasers (DRLs) are highly efficient and the average output of multi-tens of watts in pulsed and kilowatt range in CW regime have been reported. Mostly, DRL are demonstrated in simple intra-cavity and external cavity

configurations with the major focus on power scaling. Different unconventional geometries like backscattering, and distributed feedback gain, could result in even higher efficiencies and output energies. Stimulated Raman scattering often results in pulse shortening. Raman lasing of pure synthetic diamond was studied under single frequency 532 nm pump radiation to compare efficiency and pump pulse shortening capabilities in several cavities that allow single, double pass, and multi-pass Stokes amplification.

Keywords: Color centers, Spectroscopy, Pump-probe spectroscopy, Absorption saturation, Stimulated Raman scattering, Backscattering, Distributed feedback

## DEDICATION

I dedicate this work to my amazing parents, Tum Lal Subedi and Kamala Subedi, my husband Dr. Krishna Karki, my brother Ashish and my sister Smiriti, who never got tired of supporting me and provide me the strength and comfort.

## ACKNOWLEDGMENTS

I wish to express my deep gratitude to my advisors Dr. Sergey Mirov and Dr. Vladimir Fedorov for their knowledge, expertise, never-ending support, guidance, and encouragement without which my academic accomplishment would not be possible. I would like to thank Dr. Martyshkin, Dr. Peppers, and Dr. Gafarov for helping me to conduct experiments, enlightening me with their hard-earned skill and experience. I sincerely appreciate committee members Dr. Zvanut, Dr. Catledge, Dr. Maqbool, and Dr. Kung for providing the learning opportunities in various disciplines and giving valuable feedbacks.

I heartily thank Dr. Krishna Karki, my better half, whose relentless support, encouragement, and work participation are the source of motivation for me. I would also like to thank current graduate students in our lab, Saugat Ghimire, Rick Watkins, and Taylor Kesterson, with them I had a chance to share knowledge, experience, and laughter.

I am also grateful to all the faculty members, staff, and fellow students at the UAB physics department who helped me in many ways throughout this time. I will cherish the time spent here at UAB and will remain in my memory forever.

## TABLE OF CONTENTS

ABSTRACT.....	ii
DEDICATION.....	v
ACKNOWLEDGMENTS .....	vi
TABLE OF CONTENTS.....	vii
LIST OF FIGURES .....	x
LIST OF TABLES .....	xx
CHAPTER 1 .....	1
INTRODUCTION TO DIAMOND AND ITS COLOR CENTERS.....	1
1.1 Background and Motivation.....	1
1.2 Physical Properties of Diamond.....	2
1.3 Energy Levels of Defect Centers in Diamond .....	6
1.4 Physical Properties of Color Centers in Diamond .....	8
1.5 Interaction of Radiation with Atom in the Crystal.....	10
1.5.1 Spectroscopic Method: The Füchtbauer–Ladenburg Equation.....	10
1.5.2 Experimental Approach.....	14
1.5.3 Theory of Vibronic Transitions: Electron-Phonon Coupling.....	16
1.6 Literature Review of Diamond and Its Color Centers.....	21
1.7 Problem Statements.....	25
1.8 Objectives of Research.....	27
CHAPTER 2 .....	31

PHOTO INDUCED IONIZATION PROCESSES IN NV <sup>0</sup> AND NV <sup>-</sup> CENTERS.....	31
2.1 Application of NV <sup>0</sup> and NV <sup>-</sup> Centers in Photonics .....	31
2.2 Introduction to NV <sup>0</sup> and NV <sup>-</sup> Centers.....	32
2.3 Description of Sample Preparation .....	36
2.4 Room Temperature Absorption Measurements .....	36
2.5 Room Temperature Photoluminescence Measurements .....	38
2.5.1 Emission Spectra under Pulsed and CW 532nm Pump Excitations.....	38
2.5.2 Low Temperature PL Spectra and Kinetics Measurements .....	41
2.6 Estimation of Absorption and Emission Cross-sections .....	45
2.7 Absorption Saturation Under 532 nm Excitation.....	47
2.8 Laser Experiments under 532 nm Pulse Excitation .....	50
2.9 Pump-Probe Experiment at Different Probe Wavelengths .....	52
2.10 Absorption Saturation Measurement under 633 nm Pump.....	57
2.11 Model Describing Saturation and Pump-Probe Kinetics .....	59
2.12 Conclusion of Chapter 2.....	63
CHAPTER 3 .....	65
EXCITATION KINETICS OF GR1 CENTERS.....	65
3.1 Background .....	65
3.2 Spectroscopic Properties of GR1 Centers .....	66
3.3 Sample Preparation and Experimental Setup .....	68
3.4 Visible and NIR Absorption Spectra.....	69
3.5 Thermal Annealing of the Sample with GR1 centers .....	71
3.6 Emission under Pulsed 633 nm Excitation.....	74
3.7 Pump-probe experiment under nanosecond excitation .....	75
3.8 Absorption saturation under 633 nm pulsed excitation.....	81
3.9 Non-selective Fabry-Pérot cavity setup .....	89
3.10 Laser Experiment with LiF:F <sub>2</sub> <sup>+++</sup> Crystals.....	92
3.10.1 Introduction .....	92
3.10.2 Sample preparation and Experimental details .....	94

3.10.3 Absorption of $F_2^{+**}$ centers in LiF .....	96
3.10.4 Laser characterization of $F_2^{+**}$ CCs in LiF .....	98
3.11 Conclusions of CHAPTER 3 .....	102
CHAPTER 4 .....	104
LASER APPLICATIONS OF DIAMOND .....	104
4.1 Introduction .....	104
4.2 Undoped Diamond Samples Description .....	106
4.3 Multi-pass Amplification of Raman Stokes .....	107
4.4 Double Pass Amplification for the 1st Stokes .....	111
4.4.1 Set-up With a Single Pass Pumping .....	111
4.4.2 Set-up With a Double Pass Pumping .....	115
4.5 Single-pass for 1 <sup>st</sup> Stokes .....	117
4.5.1 Normal Incidence for Backscattering Geometry .....	117
4.5.2 Non-normal Incidence for the Distributed Feedback Geometry .....	120
4.6 Conclusion of Chapter 4.....	124
CHAPTER 5 .....	127
CONCLUSIONS.....	127
5.1 Summary of the Results and Conclusions.....	127
5.2 Future implementation .....	131
APPENDIX A.....	133
A.1. Calibration of Photoluminescence Spectra.....	133
A.1.1 $NV^-$ PL Spectra Calibration .....	134
A.1.2 GR1 PL spectra calibration .....	136
LIST OF REFERENCES .....	137

## LIST OF FIGURES

Figure 1.1. Classification of the diamond based on the type of nitrogen impurity.....	4
Figure 1.2 Schematic diagram of the electronic energy levels splitting of color center in the unrelaxed tetrahedral configuration and in the presence of spin orbit coupling (for NV centers) and dynamic Jahn Teller distortion (for GR1 center).....	6
Figure 1.3 Splitting of the degenerate energy levels in the presence of electron and lattice field creating the manifolds 1 and 2.....	11
Figure 1.4 Representation of an emission band as a combination of multiple broadened transitions at different frequencies range. ....	13
Figure 1.5 Scheme showing incident light of intensity $I_0(\nu)$ traversing through the medium of thickness L at frequency ' $\nu$ '. ....	15
Figure 1.6 Configuration coordinate (Q) diagram of absorption (Abs) and emission (Em) transitions between ground level ( $E_a$ ) and first excited state ( $E_b$ ). The energy of the zero-phonon line (ZPL), Stokes' shift, and width of the absorption and emission ( $\Delta_{\text{FWHM}}$ ), and Franck-Condon Shift $\Delta$ .....	17
Figure 2.1 Diamond lattice is shown by a cube (black outline) with NV center where substitutional nitrogen (purple sphere) and a vacancy (white sphere) are adjacent to each other. ....	33

Figure 2.2 Energy level of  $NV^-$  and  $NV^0$  centers in the band gap of diamond and two-step photoionization mechanism of  $NV^-$  and  $NV^0$  centers. Energy separations between two energy states are shown by double-sided arrows. Single arrow line shows optical transition (absorption and radiative decay) and dashed arrow lines show non-radiative decay via intersystem crossing (ISC). ..... 34

Figure 2.3 (A) Transmission spectrum of the sample at room temperature through 0.29 mm side and corrected to Fresnel reflection loss, (B) Corresponding absorption spectrum showing absorption bands of  $NV^-$  and N3 color centers. .... 37

Figure 2.4. Design of the experimental setup to conduct luminescence measurements. For low-temperature measurements, the sample was placed in a closed-cycle cryostat which is capable to tune the temperature down to 10K. .... 38

Figure 2.5. (A) The calibrated emission spectra were measured under CW (red solid curve) and pulsed (blue dashed curve) 532 nm excitations and normalized to 1 for comparison. Under pulsed excitation, some of  $NV^-$  centers are photoionized to  $NV^0$  showing ZPL at 575 nm and associated vibronic band. (B) Emission spectra (500 to 670 nm) normalized at  $NV^-$  ZPL (~638 nm) at different pulsed pump energies. .... 39

Figure 2.6 The emission spectrum of NV centers at low temperature (12K) under 532nm pulsed excitation, which is calibrated to the sensitivity of detection platform used and normalized to 1. .... 42

Figure 2.7 PL kinetics of NV centers in diamond under 532 nm pulsed excitation (i) at pump beam wavelength, (ii) at 576 nm (near the ZPL of  $NV^0$  centers), (iii) at 638 nm (near the ZPL of  $NV^-$  centers), (iii) at 680 nm (near the peak of emission

band), (iv) at 850 nm (near the tail of PL spectrum) measured at (A) 300K (room temperature) (B) 92 K, and (C) 12K.....	43
Figure 2.8. Room temperature absorption and calibrated emission spectra of the NV <sup>-</sup> centers normalized to 1. ....	45
Figure 2.9. The experimental setup to conduct absorption saturation measurement (A). Variation of a 532 nm pump beam transmission through the sample as a function of a pump energy density (B) (i) calculated using Frantz-Nodvik equation (red dash) and (ii) measured (blue circles). ....	49
Figure 2.10. Cavity setup and pumping scheme used for laser oscillation under longitudinal pumping by 532 nm and 633 nm pulsed radiation. The Fabry-Perot resonator shown above was a flat-flat cavity made by a high reflector (HR) and Fresnel reflection (17%) from crystal surface as an output coupler. ....	50
Figure 2.11. Schematic diagram of the pump-probe experiment where the direction of pump pulse and CW probe are shown by green and red arrow line, respectively.....	52
Figure 2.12. Signal measured at probe beam wavelength at 632 nm using (i) 532 nm pump beam and probe beam simultaneously, (ii) probe beam only (after blocking the 532 nm pump beam) in (A) microsecond time scale and (B) millisecond time scale.....	54
Figure 2.13. Signal measured at probe beam wavelength at 670 nm using (i) probe beam only (after blocking the 532 nm pump beam) and (ii) 532 nm pump beam and probe beam simultaneously.....	55

Figure 2.14. Comparison of the evolution of normalized $\Delta k/k_0$ kinetics under 532 nm pumping at probe wavelengths (i) at 632 nm and (ii) at 670 nm.....	56
Figure 2.15. The dependence of 633 nm pump transmission through the sample as a function of a pump energy fluence (i) calculated using Frantz-Nodvik equation (red dashed line) and (ii) measured from the experiment (blue circles).....	58
Figure 2.16 Illustration of the energy levels of $NV^0$ and $NV^-$ centers and corresponding population densities and cross-sections used to describe the proposed model of saturation and pump-probe experiments.....	60
Figure 3.1. The energy level of GR1 centers in diamond as described in the literature. The green arrows show absorption from the ground level and the red arrow shows radiative decay. Various non-radiative decay channels are shown by the yellow dotted arrow lines.....	67
Figure 3.2. Photos of the HD and LD samples (A) from top view when samples were sitting on $3 \times 3$ mm <sup>2</sup> sides and (B) through view when samples were sitting on $3 \times 1$ mm <sup>2</sup> sides. The black spot seen on the LD sample was due to optical damage during intense optical excitation.....	68
Figure 3.3. (A) Transmission spectra of HD (curve i) and LD (curve ii) samples at room temperature; (B) GR1 absorption spectra of the HD and LD samples normalized near 630 nm. There is an additional band near 480 nm, which may partially overlap with the GR1 absorption band.....	70

Figure 3.4 Absorption spectra of HD samples through 1 mm side before and after four different annealing steps to show the change in the distribution of color centers concentration.....	72
Figure 3.5 Absorption spectra (in arbitrary units) of HD sample before and after four different annealings (A) normalized at the maximum of 470 nm band, (B) their difference from the absorption after 4 <sup>th</sup> annealing (to reveal true GR1 absorption band), (C) normalized at a maximum of GR1 absorption, and (D) their difference from the absorption spectra after 4 <sup>th</sup> annealing (to reveal true 480 nm band). .....	73
Figure 3.6. The normalized (i) absorption band and (ii) emission band of GR1 centers were measured under pulsed 633 nm excitation and calibrated with respect to the sensitivity of the spectrometer-detector system.....	75
Figure 3.7. Experimental setup of the pump-probe experiment. Green and red arrow paths represent the probe and pump beams directions, which travelled collinearly through the sample. The mirror FM2 and a red dichroic filter separate the probe from the pump. The transmission of the probe is collected by fiber cable and directed to the monochromator - PMT combination.....	76
Figure 3.8. The kinetics of 658 nm CW probe beam at (A) nanosecond, (B) microsecond, and (C) millisecond timescales for HD and LD samples are shown in orange (curves (i)) and blue (curves (ii)), respectively. ....	78
Figure 3.9. The kinetics of 532 nm CW probe beam at (A) nanoseconds and (B) millisecond timescales for HD (curves (i)) and LD (curves (ii)) samples. ....	79

Figure 3.10. Energy level diagram of GR1 centers. The straight arrows show optical absorption, and the curly arrows show the possible relaxation channels involved in the recovery of the GR1 centers based on the model proposed using 658 nm and 532 nm probe kinetics profile of LD and HD samples. ....	80
Figure 3.11 Experimental setup for absorption saturation measurement at 633 nm. ....	82
Figure 3.12 Measured transmission of the pump signal through the samples at different input energy fluence (shown by the orange circles for LD and purple circles for HD). The measured data for LD is fitted as a slow saturable absorber. ....	83
Figure 3.13. Room temperature (i) absorption cross-section and (ii) emission cross-section, where the emission cross-section was calculated using the reciprocity method and Füchtbauer–Ladenburg equation.....	86
Figure 3.14. Non-selective cavity design to test lasing of GR1 centers under longitudinal 633 nm pumping by pulse pump laser at. The pump is focused by a spherical CaF <sub>2</sub> lens into the sample placed in a cavity formed by a high reflector (HR) and an output coupler (OC). ....	89
Figure 3.15. Non-selective cavity design to test lasing in GR1 centers for transverse pumping by pulses 633 nm pump laser. The pump is focused in a ~4mm line by cylindrical CaF <sub>2</sub> lens into the sample placed in a cavity formed by a high reflector (HR) and an output coupler (OC). ....	90
Figure 3.16. F <sub>2</sub> + center in ionic LiF lattice is a defect center with an electron trapped by two neighboring anion vacancies.....	93

Figure 3.17 Absorption spectrum of the studied LiF sample which was irradiated in 1998 (A) showing absorption band of F2 +** and F <sub>2</sub> centers, (B) absorption band of hydroxyl group OH <sup>-</sup> , measured in 1998, and (C) A current photo of the sample stored at room temperature for more than 20 years after irradiation. ....	95
Figure 3.18. (A) Transmission and (B) absorption spectra of LiF crystal (doped and Gamma irradiated in 1998), and (C) change in concentration of F2 +** CCs over the span of two decades. ....	97
Figure 3.19. Transmission spectra of LiF sample (doped and Gamma irradiated) measured through 7.5mm side (blue curve) and simulated through 25mm side (red curve). ....	98
Figure 3.20. Schematic diagram of experiment used to demonstrate lasing in LiF crystal. ....	99
Figure 3.21. (A) Normalized and calibrated spectral profile of photoluminescence (dash-dot) and lasing (solid) and (B) Temporal profiles of the 633nm pump pulse (solid line) and output of the laser cavity (dot line) and photoluminescence (dash-dot) measured with a fast Si photodiode detector. ....	100
Figure 3.22. (A) Pump density-dependent spectral profile of lasing signal of LiF: F2 +** from the cavity at room temperature. Spectra were collected by varying the pump excitation intensity. (B) Dependence of maximum signal near lasing wavelength 920 nm with input pump energy density. ....	101
Figure 4.1. Experimental setup used for multi-pass amplification of the first and second Stokes at 573 nm and 620 nm, respectively, under 532 nm pumping. ....	108

Figure 4.2. (A) The spectral position of pump, 1 <sup>st</sup> Stokes, and 2 <sup>nd</sup> Stokes. (B) Output-input characteristics for the first Stokes, the second Stokes, and the total output of the cavity for sample D2 (6 mm path length).....	109
Figure 4.3. Temporal beam profiles of input un-depleted pump (red line), depleted pump (black line), 1 <sup>st</sup> Stokes (blue line), and 2 <sup>nd</sup> Stokes (green line) were measured near the threshold for the 2 <sup>nd</sup> Stokes by 300 ps fast PIN detector. ....	110
Figure 4.4. Photos of output beams of the 1 <sup>st</sup> Stokes from the cavity for samples (A) D2 which is wedged in one plane and (B) D3 (which is wedged in both planes). (C) Total (1 <sup>st</sup> and 2 <sup>nd</sup> Stokes) output-input performance of D2 and D3 samples. ....	111
Figure 4.5. Experimental setup used for the two-pass (per round trip) 573 nm first Stokes amplification and a single-pass pumping. ....	112
Figure 4.6. Output-input characteristic for double-pass first Stokes and single-pass pumping. ....	114
Figure 4.7. (A) Time profile of undistorted pump pulse (red line) first stokes near-threshold (black curve) and much above threshold (blue curve) as measured by 250 ps pin detector. (B) Dependence of pulse duration of single pulse first stokes vs input pump power. ....	115
Figure 4.8. Experimental setup used for two-pass amplification for the first Stokes at 573 nm under double-pass 532 nm pumping. ....	115

Figure 4.9. Output-input dependence of the DRL based on D3 sample (7 mm, parallel facets) in the cavity that enables double passes both for the pump and the 1 <sup>st</sup> Stokes. ....	116
Figure 4.10 (A) Temporal profile of the input pump pulse (blue line), first Stokes near the threshold (34 mW) (black curve) and much above threshold 116 mW (red curve) as measured by 250 ps PIN detector. (B) Dependence of pulse duration of a single pulse of the first Stokes vs input pump power. ....	117
Figure 4.11. Experimental setup used for multi-pass amplification for the first Stokes at 573 nm and single-pass 532 nm pumping. ....	118
Figure 4.12. Output-input characteristics of DRL for the 1 <sup>st</sup> Stokes single-pass amplification for normal incidence. ....	119
Figure 4.13. (A) Temporal profile of the input pump pulse (blue dash line) and the first Stokes near-threshold (orange curve) as measured by 250 ps pin detector. (B) Dependence of the pulse duration of the single pulse first Stokes on input pump power.....	120
Figure 4.14 Interfering beams intersecting at an angle $\theta_m$ inside the crystal to create the dynamic grating.....	121
Figure 4.15. The setup was used to obtain a Raman laser at non-normal incidence. ....	122
Figure 4.16 (A) Output-input characteristic of the DRL setup used in Figure 15. (b) Temporal profile of un-depleted pump (red dashed-dotted line), depleted pump (blue dotted line), and first stokes (solid black line).....	123

Figure A.1 Graph showing the spectra of the lamp measured (black curve) and standard (blue curve), the total transmission of the two orange filters (green curve), and photoluminescence of the NV centers measured (red curve) and calibrated (purple curve)..... 135

Figure A.2 Graph showing the spectra of the lamp measured (red curve) and standard (blue curve), the transmission of the filter (pink curve), and photoluminescence of the GR1 centers measured (black curve) and calibrated (green curve). ..... 136

## LIST OF TABLES

Table 1-1. Most common color centers in diamond [7].....	1
Table 1-2. Physical parameters of diamond relevant to its performance as a Raman gain medium and host for many color centers. ....	3
Table 1-3. Raman properties of diamond and other commonly used Raman crystals. ....	5
Table 1-4. Summary of physical and spectroscopic properties of NVs and GR1 centers in diamond crystals. ....	9
Table 2-1. PL lifetimes of NV centers at different wavelengths and temperatures .....	44
Table 2-2. Spectroscopic parameters associated with transition ${}^3E \leftrightarrow {}^3A$ of $NV^-$ color center in diamond. ....	47
Table 3-1. Various spectroscopic parameters for GR1 center estimated from the experiments. ....	88
Table 4-1. Transmission parameter of cavity mirrors used at the pump, first and second Stokes wavelengths.....	108
Table 4-2. Pulse durations and energies of the pump, and Raman laser in the forward and backward directions near threshold. ....	120

# CHAPTER 1

## INTRODUCTION TO DIAMOND AND ITS COLOR CENTERS

### 1.1 Background and Motivation

During the past decade, diamond has emerged as one of the most exciting materials of study within the field of photonics [1]. Unique and robust properties make it a highly desirable material for many applications, including high-frequency micro- and nano electromechanical systems, nonlinear optics, magnetic and electric field sensing, and biomedicine. Diamond, as an attractive platform for on-chip photonics, combines the advantages of a high refractive index ( $n = 2.4$ ) and low absorption losses within its large transmission window (from the ultraviolet to far-infrared) [2]. It offers a unique opportunity to combine nonlinear photonics with quantum optics: for instance, diamond nonlinearities could allow for frequency translation (to the telecom wavelength range) and pulse shaping of single photons generated by its numerous color centers, which are often emitted in the visible to near-infrared region. These processes promise the coalescence of quantum information science with classical optical information-processing systems on the same chip.

Other areas of applications of visible pulsed lasers are biomedical imaging and STED microscopy. Such applications often have stringent requirements on the linewidth, wavelength, and pulse duration, which are not directly available from typical solid-state

sources. One method of accessing these wavelengths is to use Raman lasers [3]. The use of diamond as fast optoelectronic switches has been reported in the literature and the mechanical and thermal design of diamond "heat sink" substrates for semiconductor laser diodes is advancing rapidly [4].

The color of diamonds originates from atomic substitutions within the diamond lattice called ‘color centers’. Diamond can accommodate an enormous number of defect centers consisting of impurity atoms and intrinsic vacancies each with very unique optical properties [5]. There are several hundred color centers in diamond identified and most of them are detectable based on emission and absorption spectroscopies. The most common color centers, their notation, and structure are listed in Table 1-1. Recently, the quantum community has invested an enormous effort to interface special defects in diamond known as color centers with photonic resonators and waveguides [2]. Diamond with color centers is also favorable material in the field of “atomic physics” since the technology of its growth, nanofabrication, and ionizing treatment for obtaining a desirable concentration of color centers are well established [6]. In addition, a uniquely high thermal stability of intrinsic color centers in diamond makes them of great interest as laser active centers for practical visible and near-infrared tunable lasers.

Table 1-1. Most common color centers in diamond [7].

Centers	Structure	ZPL energy (eV)	Possible to observe			Ref
			Abs	PL	CL	
GR1	V <sup>0</sup>	1.673	Yes	Yes	Yes	[8,9]
ND1	V <sup>-</sup>	3.15	Yes	No	No	[8]
H3	[N-V-N] <sup>0</sup>	2.463	Yes	Yes	Yes	[10]

NV	[N-V] <sup>-</sup>	1.945	Yes	Yes	No	
	[N-V] <sup>0</sup>	2.156	Yes	Yes	Yes	[8]
N3	[3N-V] <sup>0</sup>	2.98	Yes	Yes	Yes	[8,11]

Among all the defect centers in diamond, the most interesting negatively charged nitrogen-vacancy (NV<sup>-</sup>) defect center is considered a potential solid-state alternative to trapped ions for quantum computing. It has been investigated for almost two decades, often in relation to applications in quantum computing and quantum sensing [12]. Laser threshold magnetometry was recently proposed as a novel way of measuring magnetic fields with NV center ensembles, enabling higher contrast and stronger output signals using stimulated emission. A highly sensitive molecular detection platform based on broadly tunable visible to near-infrared radiation sources would be of interest in the scientific community.

## 1.2 Physical Properties of Diamond

The lattice structure of the gain medium is very pertinent to Raman lasing because it dictates the available vibrational modes and frequency shift. Carbon is a group IV element in the periodic table with the electronic configuration  $1s^2 2s^2 2p^2$  configuration. Carbon atoms in the diamond lattice are bonded by  $sp^3$  hybridized orbitals. It is a perfectly covalent lattice and dipole moment is absent, resulting in the fact that diamond lattice does not absorb photons in the one-phonon spectral region. The intrinsic absorption occurs in two- and three- phonon absorption regions (2.5  $\mu\text{m}$  to 5  $\mu\text{m}$ ) [5]. Because of the stiff lattice and light weight of carbon atoms, high Debye temperature provides a larger and narrower

Raman shift with respect to other counterparts. Because of a wide band gap, multi-photon and free-carrier absorption losses in diamond are absent. The major physical properties of diamonds are presented in Table 1-2.

Table 1-2. Physical parameters of diamond relevant to its performance as a Raman gain medium and host for many color centers.

<b>Parameters</b>	<b>Symbol</b>	<b>Unit</b>	<b>Single crystal</b>	<b>Polycrystal</b>
<b>Thermal conductivity at 300 K</b>	k	$\text{Wm}^{-1}\text{K}^{-1}$	>2000	-
<b>Thermal conductivity at 500 K</b>	k	$\text{Wm}^{-1}\text{K}^{-1}$	1100	1100
<b>Expansion coefficient at 300 K</b>	$\alpha$	$\times 10^6 \text{K}^{-1}$	$1.0 \pm 0.1$	$1.0 \pm 0.1$
<b>Expansion coefficient at 1000 K</b>	$\alpha$	$\times 10^6 \text{K}^{-1}$	$4.4 \pm 0.1$	$4.4 \pm 0.1$
<b>Bandgap</b>	$E_g$	eV	5.47	5.47
<b>Refractive index at 1064 nm</b>	n	-	2.39	2.39
<b>Thermo optic coefficient</b>	dn/dt	$\times 10^{-6} \text{K}^{-1}$	9.6	9.6
<b>Dielectric constant</b>	D		-	$5.68 \pm 0.15$
<b>Absorption coefficient at 1064 nm</b>	k	$\text{cm}^{-1}$	< 0.05	< 0.07
<b>Birefringence</b>	$n_e - n_o$		$10^{-4}$	
<b>Specific heat capacity at 300 K</b>	C	$\text{JKg}^{-1}\text{K}^{-1}$	520	520
<b>Density</b>	$\rho$	$\times 10^3 \text{Kgm}^{-3}$	3.52	3.52
<b>Nonlinear refractive index at 515 nm</b>	$n_2$	$\times 10^{-15} \text{cm}^2\text{W}^{-1}$	1.3	$1.4 \pm 0.2$

$\chi^{(3)}$ nonlinear susceptibility at 515 nm	$\chi^{(3)}$	$\times 10^{-21} \text{ m}^2 \text{ V}^{-1}$	2.7	
Lattice parameter at 300K	a	Å	3.567	3.567
Nearest Neighbor distance	d	Å		
Bond length	d	Å	1.54	1.54
Number density	n	$\times 10^{17}$ centers $\text{cm}^{-3}$	1.76	1.76

Diamonds are classified in terms of nitrogen concentration present in the sample, which is shown in Figure 1.1. Nitrogen impurities in the form of substitutional (Ns), A aggregates (N-N), and B aggregates (4N-V) are readily available in most natural diamonds. Two major synthesis processes have enabled the production of consistently engineered synthetic diamonds: high pressure and high temperature (HPHT) synthesis and chemical vapor disposition (CVD) where the desired concentration of nitrogen and other impurities can be incorporated.

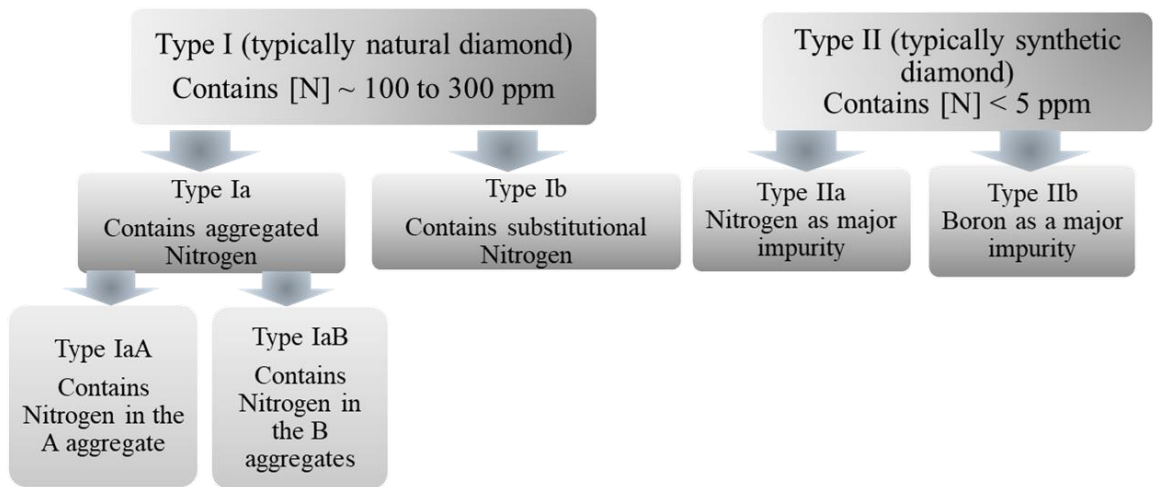


Figure 1.1. Classification of the diamond based on the type of nitrogen impurity.

Single crystal synthetic diamonds available nowadays are essentially free of impurity centers and dislocations, which helps to minimize absorption losses and enables the ultimate power scaling capability. In order to compare the performance of various Raman gain crystals, Lubeigt et al (2010) [13] introduced a terminology called “figure of merit (FoM)” as given in the equation (1.1). FoMs and parameters on which they depend per equation (1.1) are depicted in Table 1-3. As one can see, FoM for a diamond is two orders of magnitude higher than for other commonly used Raman gain media. Also, higher the FoM, the smaller is the thermal lensing, the lower the threshold, and the higher would be the gain [14].

$$FoM = \frac{k g_R l}{\Delta\lambda \frac{dn}{dt}} \quad (1.1)$$

Table 1-3. Raman properties of diamond and other commonly used Raman crystals.

<b>Parameters</b>	<b>Diamond</b>	<b>Ba(NO<sub>3</sub>)<sub>2</sub></b>	<b>KGd(WO<sub>4</sub>)<sub>2</sub></b>	<b>YVO<sub>4</sub></b>
Raman Shift ( $\Delta\lambda$ ) ( $cm^{-1}$ )	1332	1047	768	892
Raman gain (g) @ 1.064 $\mu m$ ( $cmGW^{-1}$ )	17	11	4.4	5
Thermal conductivity (k) @RT ( $Wm^{-1}K^{-1}$ )	2000	1.2	2.6	5.2
Transparency window ( $\mu m$ )	0.23-100	0.3-1.8	0.3-5	0.4-5
Typical length (mm)	6-8	~20	25	3
dn/dt ( $\times 10^{-6} K^{-1}$ )	9.6		-10	3
Raman FOM	1440	1	3	20

### 1.3 Energy Levels of Defect Centers in Diamond

As the defect centers are created, the structure of the energy levels will be changed due to additional perturbations. The type of interaction imposed in the crystal will depend on the symmetry of the defect and unpaired electrons in the valence orbitals. The degeneracy of the energy levels will be lifted depending on the strength of the interaction acting at the defect point.

The symmetry imposes that the four carbon atoms surrounding the vacancy are initially equivalent. This ideal, unrelaxed neutral vacancy has four dangling hybrids orbitals from neighboring carbon atoms next to the vacancy pointing inwards, and in tetrahedral symmetry ( $T_d$ ), these give rise to a nondegenerate energy level belonging to a one-electron state of  $a_1$  symmetry, which falls just above the top of the valence band. The triply degenerate states belonging to the  $t_2$  symmetry representation occurs deep in the band gap.

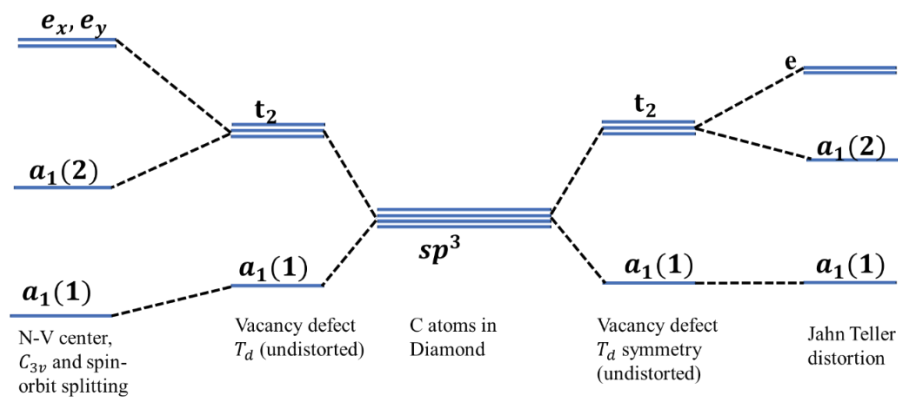


Figure 1.2 Schematic diagram of the electronic energy levels splitting of color center in the unrelaxed tetrahedral configuration and in the presence of spin orbit coupling (for NV centers) and dynamic Jahn Teller distortion (for GR1 center).

The representation of electronic energy levels of neutral vacancy (GR1) in unrelaxed tetrahedral and dynamics Jahn Teller distortion is illustrated in Figure 1.2. The surrounding four atoms relax outward by 0.2 Å in the GR1. The  $a_1$  state has the lowest energy and is filled with two of the four electrons of the dangling bonds. The other two electrons occupy the localized  $t_2$  state. The energy levels induced by these states fall well inside the band gap. The  $a_1$  state often appears as a resonance state near the top of the valence band. The ground state of GR1 is  $^1E (a_1^2 t_2^2)$ , where  $a_1$  and  $t_2$  represent the electron orbitals formed from the four tetrahedral  $sp^3$  dangling bonds to the vacancy, while the excited state is denoted as  $^1T_2 (a_1^2 t_2^2)$  [15]. The neutral vacancy undergoes a Jahn-Teller distortion with an energy gain of 0.36 eV. This effect is known to be dynamic at room temperature [16]. Such a partially filled degenerate electronic state  $t_2$  is unstable under Jahn-Teller distortion which lowers the symmetry of the structure. The  $t_2$  triply degenerate state then splits into a nondegenerate  $a_1(2)$  state and a doubly degenerate ‘e’ state. The two electrons that occupied the  $t_2$  state will therefore be in the  $a_1(2)$  state, and the  $e$  state will remain unoccupied.

On the other hand, the NV color center consists of substitutional nitrogen of a carbon atom adjacent to a vacancy. This defect has a  $C_{3v}$  symmetry meaning spatially invariant under the  $C_{3v}$  symmetry transformations. In this case,  $a_1(1)$  further goes below the valence band minimum and the degenerated triplet  $t_2$  splits to  $a_1$  and  $e = \{e_x, e_y\}$  by spin-orbit coupling and spin-spin interaction as shown at the left side of Figure 1.2.  $NV^0$  has five electrons (two from nitrogen lone pair and three from adjacent dangling bonds) with ground state  $^2E (a_1^2 e^1)$  and excited state  $^2A (a_1^1 e^2)$  and corresponding energy

separation is 2.15 eV. Similarly,  $NV^-$  has extra electron from some donor in the crystal and its ground and excited states  ${}^3A_2 (a_1^2 e^2)$  and  ${}^3E (a_1^1 e^3)$ , respectively, are separated by 1.945 eV. The charge and spin density are unevenly distributed among the three-carbon dangling bonds near the vacancy and the nitrogen lobe in the ground state while it is significantly redistributed toward the nitrogen lobe in the excited state. Consequently, the permanent dipole moments of the ground and excited state significantly change which shifts the separation between energy levels in the presence of external electric fields. It allows external fields to modulate fluorescence intensities to enhanced contrast capability.

#### 1.4 Physical Properties of Color Centers in Diamond

Color centers in diamond had been considerably studied and several hundreds of defect centers have been detected and identified based on emission and absorption spectroscopies. Ultrawide bandgap of diamond (5.5 eV) provides a huge transmission window ranging from UV(250 nm) to FWIR (100  $\mu\text{m}$ ) spectral range. Besides that, excellent thermal and mechanical properties make diamond an unrivaled host. Most of the centers are photostable and chemically inert. The color centers associated with vacancy and nitrogen impurities have absorption bands from 350 nm to roughly 750 nm with a lifetime varying from several nanoseconds to tens of nanosecond range. Most of the commercially available lasers can be used as pump sources for optical excitation. The impurity centers in diamond are known to be strongly luminescent at a wide range of temperatures with no temperature quenching. The quantum efficiency of fluorescence is large even at room temperature. Similarly, the electron-phonon coupling between electrons

at the defect site results in a significant broadening of absorption and emission bands as well as in a large difference in the configuration coordinates of the minima of the adiabatic potentials. This difference results in large Stokes' shift between luminescence and absorption bands with bandwidth reaching up to 65% of the central wavelength. Their unique properties can be exploited in many photonics applications.

Table 1-4. Summary of physical and spectroscopic properties of NVs and GR1 centers in diamond crystals.

Parameters	Symbol	Unit	NV <sup>-</sup>	NV0	GR1
<b>Typical Concentration</b>	[N]	$\times 10^{17}$ centers $\text{cm}^{-3}$	1-10	1-10	1-10
<b>Absorption</b>					
<b>Transition</b>			$^3A_2 \rightarrow ^3E$	$^2E \rightarrow ^2A$	$^1E \rightarrow ^1T_2$
<b>Zero phonon line</b>	ZPL	nm	638	575	741
<b>Transition</b>					$^1A \rightarrow ^1T_2$
<b>Zero phonon line</b>	ZPL	nm			744
<b>Absorption band</b>		nm	470 to 650	420 to 600	520-750
<b>Central wavelength</b>	$\lambda_{ab}$				
<b>Absorption bandwidth (FWHM)</b>	$\Delta\lambda_{ab}$	nm	~100	~100	~158
<b>Absorption cross section at ZPL</b>	$\sigma_{ab}$	$\times 10^{-17} \text{ cm}^2$	$4 \pm 1$	$1.8 \pm 0.4$	NA
<b>Emission</b>					
<b>Transition</b>			$^3E \rightarrow ^3A_2$	$^2A \rightarrow ^2E$	$^1T_2 \rightarrow ^1E$
<b>Emission band</b>		nm	620 to 850	550 to 800	720 to 1100
<b>Central wavelength</b>	$\lambda_{em}$	nm	700	650	780
<b>Emission bandwidth (FWHM)</b>	$\Delta\lambda_{em}$	nm	~100	~100	~200
<b>Emission cross section at <math>\lambda_{em}</math></b>	$\sigma_{em}$	$\times 10^{-17} \text{ cm}^2$	3.5	1.7	NA
<b>Lifetime at 300K</b>	$\tau_{RT}$	ns	12	$20 \pm 2$	1.1

<b>Lifetime at 77K</b>	$\tau_{77}$	ns	-	$19 \pm 2$	4
------------------------	-------------	----	---	------------	---

## 1.5 Interaction of Radiation with Atom in the Crystal

### 1.5.1 Spectroscopic Method: The Füchtbauer–Ladenburg Equation

When characterizing the spectroscopic properties of these materials, the relationship between the spontaneous emission spectrum and the emission cross-section can be modeled using the Füchtbauer-Ladenburg (FL) approximation. We consider a 2-level system with a well-justified assumption that the central frequency of transition ( $\nu_0$ ) is much bigger than the spectral bandwidth of the transition ( $\nu_0 \gg \Delta\nu$ ). In such a situation, Einstein's approach can be used to obtain cross-sections and other spectroscopic parameters. Einstein considered an important generalization for the situation that the upper and lower level may have degeneracies, i.e. that they actually consist of multiple levels, each having the same energy. This situation often occurs for the electronic states of isolated atoms or ions. However, in most practical cases the absorption and emission bands consist of multiple optical transitions. In these cases, the inequality  $\nu_0 \gg \Delta\nu$  is not always justified and special considerations are needed.

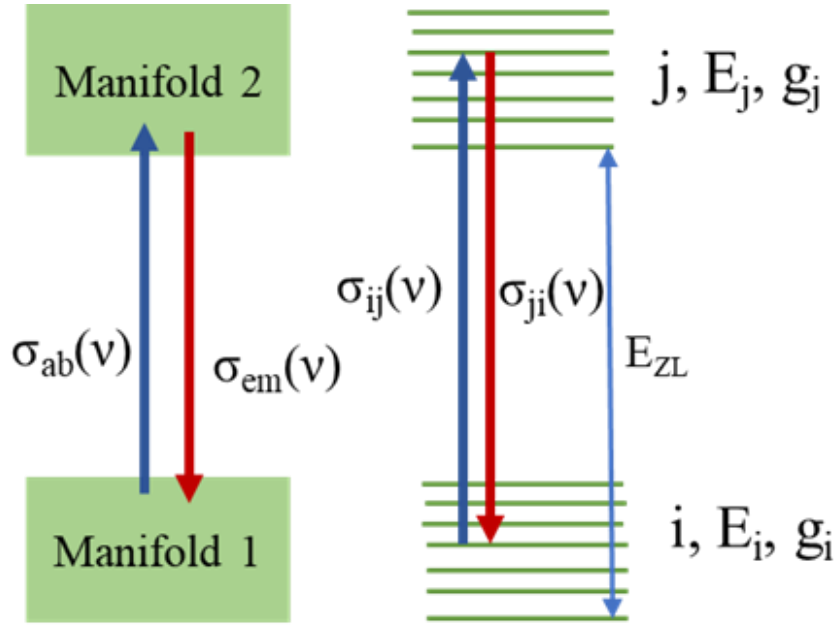


Figure 1.3 Splitting of the degenerate energy levels in the presence of electron and lattice field creating the manifolds 1 and 2.

In a real crystal, the interaction of laser-active ions with the lattice field partly removes the degeneracies as shown in Figure 1.3. There are therefore Stark level manifolds with a spread of level energies. As this splitting can be comparable to (or larger than) the thermal energy  $k_B T$ , the average population fractions for the sublevels differ according to a Boltzmann distribution. Fundamental radiation quantities are different for individual levels and individual transition within the manifold. Füchtbauer and Ladenburg proposed another way of determining emission cross-sections of laser gain medium based on the assumption that (i) all energy levels of manifold 2 have the same radiative lifetime ( $\tau_{rad}$ ) and (ii) transition linewidth of individual transition ( $i \leftrightarrow j$ ) is much smaller than the central frequency  $\Delta\nu_{ij} \ll \nu_{0,ij}$ . In this case the emission cross-section can be written as,

$$\sigma_{ji}(\nu) = \frac{c^2}{8\pi n^2 \tau_{rad} \nu_{0,ji}^2} g_{ji}(\nu), \quad (1.2)$$

where  $g_{ij}(\nu)$  is the lineshape of the gain profile and  $\tau_{rad}$  is the radiative lifetime of the state  $i$ . Emitted fluorescence intensity due to the ( $j \rightarrow i$ ) transition over the frequency interval  $d\nu$  is

$$I_{ji}(\nu)d\nu = G \frac{N_i}{\tau_{rad}} h\nu g_{ji}(\nu) d\nu, \quad (1.3)$$

where  $G$  is a calibration factor that accounts for the fraction of the fluorescence which is collected by the optical detection platform;  $N_i$  is the population density in the  $i$  sublevel ( $N_i = N_{tot} f_i$ ). Solving the equation (1.2) for  $g_{ji}(\nu)$  and substituting into the equation (1.3)

$$I_{ji}(\nu)d\nu = GN_j \frac{8\pi n^2 \nu_{0,ji}^2}{\tau_{rad}} h\nu \sigma_{ji}(\nu) d\nu \quad (1.4)$$

If the total measured emitted power is,

$$\int \frac{\sum_{ij} I_{ij}(\nu)}{h\nu} = G \frac{N_{tot}}{\tau_{rad}} \quad (1.5)$$

and measured emission is,

$$I(\nu) = \sum_{i,j} I_{ji}(\nu) \quad (1.6)$$

Then,

$$\sigma_{ij}(\nu) = \frac{c^2}{8\pi n^2 \nu_{ij}^3} \frac{I_{ij}(\nu)}{GN_{tot} f_i} = \frac{c^2}{8\pi n^2 \nu_{ij}^3} \frac{I_{ij}(\nu)}{\tau_{rad} \int \frac{I(\nu)}{h\nu} d\nu} \quad (1.7)$$

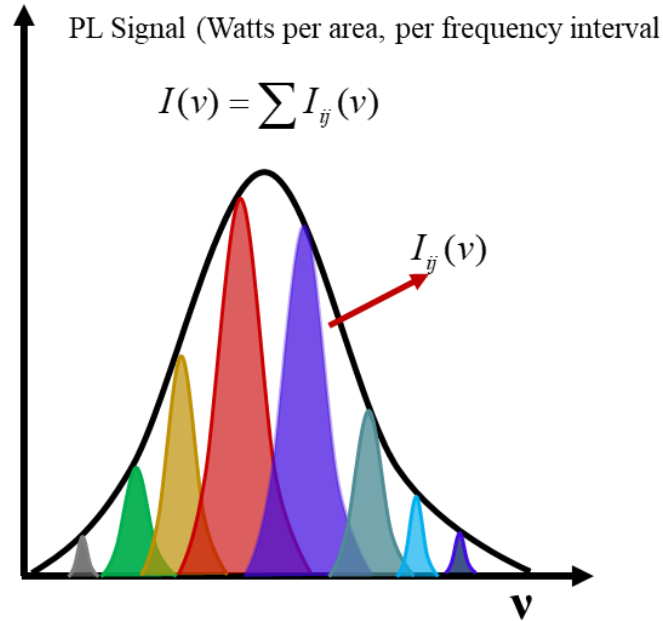


Figure 1.4 Representation of an emission band as a combination of multiple broadened transitions at different frequencies range.

If the total cross-section of emission is the sum of all possible transitions between manifolds from all levels  $I$  to all levels  $j$ ,

$$\sigma_{em}(\nu) = \sum_{i,j} f_j \sigma_{ji}(\nu) \quad (1.8)$$

Then,

$$\sigma_{em}(\nu) = \frac{c^2}{8\pi n^2 \nu_{ij}^3} \frac{I(\nu)}{\tau_{rad} \int \frac{I(\nu)}{h\nu} d\nu} \quad (1.9)$$

This expression for emission cross-section is based on fluorescence intensity calibrated over a frequency interval  $d\nu$ . If fluorescence is calculated in photon flux

$I_{ph}(\nu) = I(\nu)/h\nu$  than:

$$\sigma_{em}(\nu) = \frac{c^2}{8\pi n^2 \nu_{ij}^3} \frac{I_{ph}(\nu)}{\tau_{rad} \int I_{ph}(\nu) d\nu} \quad (1.10)$$

A more useful form of this equation is to express it in terms of wavelength, which becomes,

$$\sigma_{em}(\lambda) = \frac{\lambda_{ij}^5}{8\pi c n^2} \frac{I(\nu)}{\tau_{rad} \int \lambda I(\nu) d\nu} \quad (1.11)$$

The equation (1.11) is Füchtbauer–Ladenburg relation and  $I(\lambda)$  is spectral fluorescence distribution (W / m<sup>2</sup> / wavelength range).

### 1.5.2 Experimental Approach

One of the experimental approaches to obtain spectroscopic parameters associated with the optical transition is linear absorption spectroscopy based on Beer-Lambert law. When a light wave propagates in an absorbing medium, its intensity will be attenuated during propagation due to absorption in the medium. It depends on the frequency of the incident light. Experimentally, as shown in Figure 1.5, the amount of light absorbed by the medium is determined by measuring transmittance by taking the ratio of transmitted intensity over incident light intensity  $\left[ \frac{I(\nu)}{I_0(\nu)} \right]$ . The measured transmittance is further

utilized to find spectroscopic parameters via the Beer-Lambert relation (equation (1.12)). According to the Beer-Lambert law, over the optical spectral region, the absorption and amplification of the radiation at frequency  $\nu$  in the medium could be described by the equation,

$$I(\nu) = I_0 e^{k(\nu)L} \quad (1.12)$$

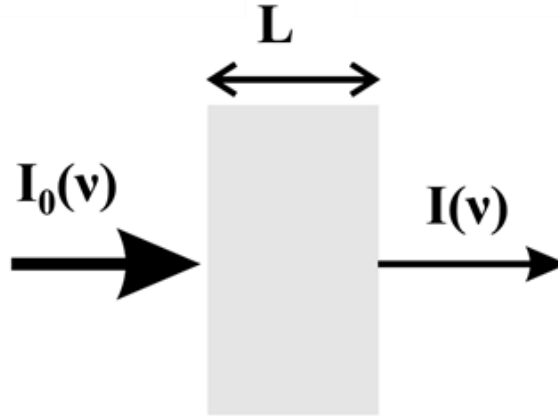


Figure 1.5 Scheme showing incident light of intensity  $I_0(\nu)$  traversing through the medium of thickness  $L$  at frequency ' $\nu$ '.

Where  $I(\nu)$ ,  $I_0(\nu)$  are intensities of the transmitted and initial light intensity, respectively;  $L$  is the thickness of the medium,  $k(\nu)$  is the absorption coefficient for  $k < 0$  or gain coefficient if  $k > 0$ . It signifies the characteristic optical centers and concentration. In the case when absorption or emission bands result from the electronic transitions within active centers (such as doped ions, atoms, or point defects) the absorption and gain coefficients are linearly dependent on center concentrations ( $N$ ). Therefore, the important spectroscopic parameters are emission ( $\sigma_{em}$ ) and absorption ( $\sigma_{ab}$ ) cross-sections, which describe the intrinsic characteristic of optical centers.

$$\sigma(\nu)_{ab(em)} = \frac{k(\nu)_{ab(em)}}{N} \quad (1.13)$$

### *1.5.3 Theory of Vibronic Transitions: Electron-Phonon Coupling*

In the previous section, the motion of electrons is considered in the static periodic potential that would arise if ions were frozen in their equilibrium position. However, the reality is that the vibrational nature of lattice vibration gives significant broadening of the absorption and emission spectra. In this model, lattice vibrates around the equilibrium position that gives different interaction potential and electron vibration gives rise to a different vibrational level in each electronic state. Transitions between energy levels in crystals involve a change in electronic state and vibrational state, which is termed “vibronic” coupling. Energy levels in diamond crystals characteristically possess strong vibronic coupling, resulting in broad energy bandwidth of the transitions which leads to the broad absorption and emission spectral features, making these media attractive for laser application. The excited state population decays with the radiative lifetime only in the absence of other non-radiative relaxation processes. One of the important channels for relaxation of the upper-level population is phonon emission.

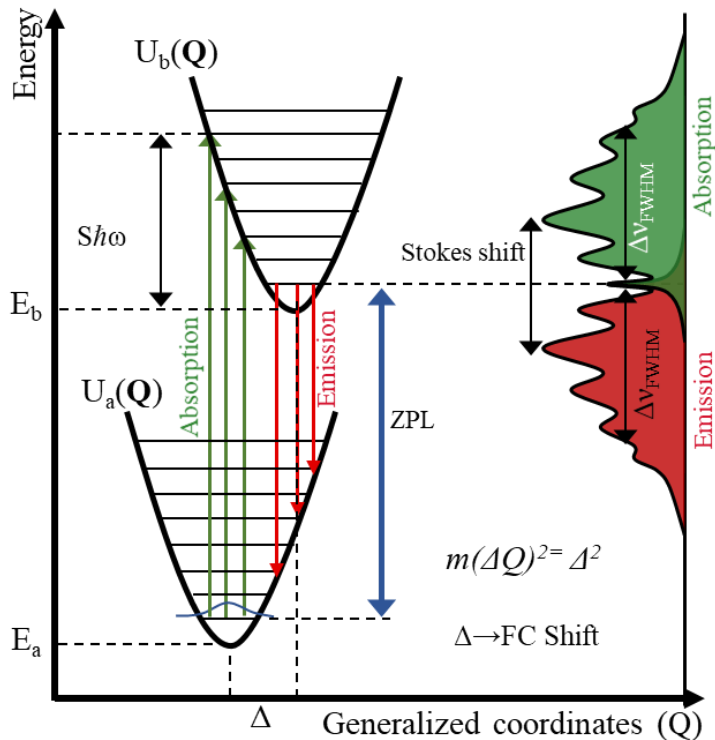


Figure 1.6 Configuration coordinate ( $Q$ ) diagram of absorption (Abs) and emission (Em) transitions between ground level ( $E_a$ ) and first excited state ( $E_b$ ). The energy of the zero-phonon line (ZPL), Stokes' shift, and width of the absorption and emission ( $\Delta V_{FWHM}$ ), and Franck-Condon Shift  $\Delta$ .

A common tool for the representation and understanding of vibronic transitions is the configuration coordinate diagram shown in Figure 1.6. This model is based on assumption that the nearest environment of the impurity ion oscillates harmonically about its equilibrium position and each level is represented by a harmonic oscillator potential which divides the electron states into vibrational sublevels. The absorption and emission spectra resulting from these transitions involve changes in electron state as well as phonon energy. The zero-phonon line energy ( $E_{ZPL}$ ) corresponds to transitions that do not involve phonon interactions. These transitions occur between the bottoms of the harmonic

oscillator potentials and are more easily measured at low temperatures due to the narrower energy.

Two main parameters which describe the electron-phonon coupling are (i) the Huang-Rhys parameter  $S$  and (ii) the effective phonon energy  $\hbar\omega$ . The parameter  $S$  gives the strength of coupling and the higher the value of  $S$  the stronger is the coupling between electrons and phonons.  $S$  is defined as the average number of phonons of energy  $\hbar\omega$  emitted as a result of the absorption process and given as;  $S = \frac{\omega\Delta^2}{2\hbar}$ ; where  $\Delta$  is the Franck-Condon shift. Both parameters  $S$  and  $\hbar\omega$  are related to the energy separation between the absorption and emission peaks called Stokes' shift  $\Delta E$ .

$$\Delta E = (2S - 1)\hbar\omega \quad (1.14)$$

In this case, the total Hamiltonian of the system includes additional energy terms resulting from the motion of the atomic nuclei around the equilibrium position.

$$H_A = T_E(\vec{r}) + V(\vec{r}, \vec{Q}) + T_N(\vec{Q}), \quad (1.15)$$

where  $T_E$  is the electron kinetic energy,  $T_N$  is the nuclear kinetic energy, and  $V(r, Q)$  includes all interactions between electrons and nuclei. Electronic and nuclear coordinates are denoted by  $r$  and  $Q$  respectively. In the Born-Oppenheimer approximation, a heavy nucleus does not have enough time to relax during the electronic transition. So, transition takes place vertically to any of the vibronic levels and changes vibrational properties of the

system which results in a new equilibrium position. Approximate eigenstates of the Hamiltonian are Born-Oppenheimer states which take the form,

$$\Psi_{n,v}^{BO} = \phi_n(r, Q) \Theta_v(Q), \quad (1.16)$$

where  $\phi_n(r, Q)$  is the eigenfunction of the electron Hamiltonian at fixed  $Q$ .

$$H_e(Q) = T_e + V(\vec{r}, \vec{Q}) \quad (1.17)$$

When applied to the electron eigenstate this yields,

$$H_e(Q) \Psi_e(\vec{r}, \vec{Q}) = U_n(\vec{Q}) \Psi_e(\vec{r}, \vec{Q}), \quad (1.18)$$

where  $U_n(Q)$  is the energy of interaction between the nucleus and the  $n$  electron and is represented by the potential energy curve as shown in Figure 1.6. Using  $E_{n,v}$  to represent the approximate total energy eigenvalue of this Born-Oppenheimer state, one can obtain:

$$[T_N + U_n(Q)] \Theta_{n,v}(Q) = E_{n,v} \Theta_{n,v}(Q) \quad (1.19)$$

Within electric-dipole transitions between Born-Oppenheimer states result in unpolarized absorption cross-section and following the derivation with the same notation as used in [17]:

$$\sigma_{ji}(\omega) = \frac{g_i \pi}{3 \hbar \epsilon_0 c} \omega_{ij} |\vec{\mu}_{ji}|^2 G(\Omega) \quad (1.20)$$

The line shape function  $G(\Omega)$  for Strong coupling limit, i.e.  $S \gg 1$ , approximate line shape function as follows:

$$G(\Omega) = \frac{1}{\sqrt{2\pi S\omega^2(2\bar{n}+1)}} \exp\left[-\frac{(\Omega-S)^2}{2\pi S\omega^2(2\bar{n}+1)}\right] \quad (1.21)$$

Where  $\bar{n}$  is the phonon occupation number at thermal equilibrium and  $2\bar{n} + 1 = \coth(\hbar\omega/2kT)$ . Full-width at half maximum of the line-shape function in eq (47) is given as,

$$\Delta\nu_{FEWHM} = \left[ (8 \ln 2) S \omega^2 \coth(\hbar\omega/2kT) \right]^{1/2} \quad (1.22)$$

As the temperature increases, absorption and emission bands spread out more. So, the broadening becomes more pronounced at higher temperatures as more phonon states are occupied. The probability of transitions between vibrational energy levels depends on the overlap of the quantum mechanical wave functions of the two levels. For the materials with a strong electron-phonon coupling and small overlap exhibit quenching of luminescence which results in the increase in the rate of non-radiative relaxation of excited species. The strength of the zero-phonon line transition is such that

$$\frac{I_{ZPL}}{I_{tot}} = \exp\left[-S \coth\left(\frac{\hbar\omega}{2kT}\right)\right], \quad (1.23)$$

where  $I(ZPL)$  is the area under the zero-phonon line absorption, and  $I(total)$  is the area under the complete absorption or luminescence band of the transition. There is a common relationship between absorption and the emission band within the limit of the linear approximation of electron-phonon coupling.

$$I_{ab}(\nu) = I_{em}(\nu)(2\nu_{ZPL} - \nu), \quad (1.24)$$

where  $I_{ab}(\nu) = K(\nu)/\nu$  and  $I_{em}(\nu) = const * E(\nu)/\nu^3$ .  $\nu_{ZPL}$  is the frequency of the ZPL transition,  $K(\nu)$  is the absorption coefficient, and  $E(\nu)$  is the spectral density of the luminescence at frequency  $\nu$ .

## 1.6 Literature Review of Diamond and Its Color Centers

Diamond Raman laser (DRL) was demonstrated not more than a decade ago and now the output characteristics of Raman lasers are bettering at a rapid pace. DRL with very high power and excellent beam qualities have already been reported with very high efficiencies which are needed to meet growing technological demands in applications as diverse as material processing, environmental and remote sensing, and optical communication [18]. Also, because of high thermal conductivity, the intra-cavity use of diamond as a heat spreader in semiconductor devices enables the demonstration of Watt-level output power [19].

Although SRS had previously been observed in a natural diamond as early as 1963 [20,21], SRS was not observed in synthetic diamond until 2004. In [22], Stokes and anti-Stokes laser lines were observed in a nanosecond and picosecond IR laser pumped

polycrystalline diamond crystal. In 2005, the operation of pulsed diamond Raman microchip laser pumped by laser diode radiation was demonstrated for the first time [23]. With the rapid progress in growth technology, along with the excellent thermo-mechanical properties, single-crystal diamond started to be used to produce Raman laser. In 2008, Mildren et al [24] reported an external cavity diamond Raman laser with output at 573 nm using Q-switched pulses at 532nm. The conversion efficiency was only 13% and authors were limited to work near the threshold due to pump-induced damage at the crystal surface. This was a significant achievement in the development of diamond's role in laser engineering and later significant improvement in output with 0.67 mJ at 573nm was demonstrated and corresponding conversion efficiency was 63% [25].

Sabella et al [26] obtained a maximum of 2W Stokes output at 1240 nm (eye-safe region) using 3.4 W of 10 ns Q-switched pulses at 1064 nm with a slope efficiency of 84% which is near the quantum limit (~86%). Feve et al [27] then demonstrated an impressive 24.5W average Raman output power at a wavelength of 1193 nm. The performance of an anti-reflection coated crystal at normal incidence with a Brewster cut sample was compared. The highest average output power, to our knowledge, was documented in the pulsed regime, which was pumped with a very sophisticated, cryogenically cooled, Q-switched Yb:YAG laser, delivering up to 340 W into the external diamond Raman laser cavity. Similarly, mode-locked diamond Raman laser synchronously pumped by a mode-locked laser running at 532 nm and pulse duration 26 ps. The diamond laser generated up to 2.2 W of average power with output pulses of duration 21 ps at a yellow wavelength of 573 nm [28]. Several other articles reported noteworthy results in terms of efficiency and

output power in the picosecond pulse regime [29,30]. Using a low-Q ring cavity, 2.75 W of first-Stokes at 1240 nm was achieved with 59% overall conversion efficiency under synchronous pumping with 4.8 W radiation of mode-locked laser at 1064 nm [30]. Also, Michelle et al (2015) [31] reported a synchronously-pumped femtosecond diamond Raman laser operating at 890 nm and pulse compression to 65 fs with a slope efficiency of 32%. The system was pumped using a mode-locked Ti:Sapphire laser at 796 nm and a pulse duration of 194 fs.

The continuous wave (CW) diamond Raman laser was demonstrated in 2010 by Lubeigt et al [13]. Low-birefringence synthetic single-crystal diamond was used in intracavity of Nd:YVO<sub>4</sub> laser and CW output power of 200 mW was achieved at the Raman wavelength (1240 nm). Also, the output power of 2.8 W was obtained in quasi-CW mode and 1.6 W Raman output with purely CW Raman output by Lubeigt et al in 2011 [32]. Later significantly high output of tens to hundreds of watts in CW and quasi-CW regimes were reported in various publications [33–35]. Recently in 2019, 1.2 kW of quasi-CW diamond Raman laser was demonstrated by Antipov et al [36] for durations 7 times longer than the thermal lens time constant. The optical-to-optical efficiency obtained for conversion from a 1.06  $\mu\text{m}$  pump to the 1.24  $\mu\text{m}$  first Stokes was 53%.

In 1985, laser action of H3 centers (a vacancy adjacent to two substitutional nitrogen atoms) in natural diamond was reported at room temperature [37] using a plane-plane resonator formed by the Fresnel reflection from crystal surfaces. The output energy of 171  $\mu\text{J}$  at 530 nm was obtained under 1.27 mJ pump pulses (13% efficiency). Later the laser effects of H3 centers were also demonstrated in synthetic diamond [38]. The

saturation of absorption of GR1 centers under Ruby laser radiation was reported in [39]. The ruby laser in a free-running regime with 3 to 4  $\mu\text{s}$  pulses was converted to giant-pulse of (0.3 to 0.5  $\mu\text{s}$ ) by using a plate of a natural diamond with GR1 centers as a Q-switcher. This result indicates the possibility of producing stationary population inversion and non-linear absorption at high energy-pumping densities in diamond with color centers [39].

Another publication on detection of stimulated emission from  $\text{NV}^-$  centers in diamond in which the authors observed both spectrally and time-resolved spontaneous emission reduction of  $\text{NV}^-$  centers under probe laser pulse at wavelengths in the phonon side band (PSB) and interpreted that as a result of stimulated emission in the PSB [40]. Amplification by stimulated emission of nitrogen-vacancy centers in a diamond-loaded fiber cavity was demonstrated in [41]. The amplification of the transmission of a cavity-resonant seed laser at 721 nm when the cavity is pumped at 532 nm was observed and it was attributed to stimulated emission. Hence, a diamond-loaded open tunable fiber-cavity system can be a potential contender for the realization of lasing with  $\text{NV}^-$  centers [41]. Other defect structures based on substitutional atoms in covalent materials, including other color centers in diamond, can be expected to furnish stable color-center lasers operating at high temperatures. With significant progress in fabrication technology and an improved understanding of color center, its properties could enable a renewed interest in color center diamond lasers [42].

## 1.7 Problem Statements

Visible laser oscillations based on direct stimulated emission are only a few and these are difficult to produce by indirect methods. Highly energetic lasers working at the longer near-IR (NIR) and IR wavelengths are more common since they are typically more efficient than visible lasers. As the effective wavelength becomes shorter, the effort required to operate a laser increases exponentially. Most of the available visible pulsed laser radiation is obtained by nonlinear frequency conversion. This involves focusing high-power NIR lasers into nonlinear crystals whose atoms interact with the intense laser light to convert some of the NIR energy to visible light. Nonlinear conversion is only efficient at very high intensities ( $\sim$  tens of megawatts/cm<sup>2</sup>) and for long path lengths, which represents a part of the difficulty in converting NIR to visible light [43]. Such a high pump intensity generates large heat loads in the gain medium which can lead to several problems such as thermal lensing, thermal and optical damage, deformation, and eventually fracture. Another alternative for visible pulse laser is dye lasers but these are less common nowadays due to a lot of drawbacks it carries like narrow tunability range, the toxicity of the dye medium, extensive maintenance requirement, and less compactness.

Diamond crystals with intrinsic and impurity perturbed color centers like (NV<sup>0</sup>, NV<sup>-</sup> and GR1) are promising media for lasing spanning over visible (550 nm) to near-infrared range (1050 nm) of the optical spectrum. Additionally, the wide optical transparency range and robust mechanical, thermal, and optical properties of diamond render it an attractive host for color center lasers. However, a comprehensive laser

characterization of color centers in diamond is still lacking. To examine the prospect of color center laser in diamond further studies are needed.

Despite the success of diamond Raman lasers and an early proposal for a lasers based on diamond defects, and the demonstration of cavity coupling of an NV laser has not been demonstrated so far. Indeed, photo-ionization of the  $NV^- \leftrightarrow NV^0$  is induced by strong light pulses [44]. For most of the applications, a thorough understanding of optical excitation and relaxation dynamics is particularly important. Nitrogen-Vacancy (NV) defect centers in diamond have drawn so much interest for their applications in quantum information and sensing. Despite the ongoing improvements in sensitivity and the range of new applications, much about the NV basic physics remains unresolved. It is vital to understand the NV centers basic physics in order to fully exploit their potential [6]. There are several published articles where PI rate at different wavelength was studied [45]. Another article published in *Nature Communications* reported stimulated emission in  $NV^-$  centers and those articles pointed out that lasing in  $NV^-$  center could be possible at an appropriate wavelength [40].

GR1 is a very common and interesting CC but studies were performed only on natural diamonds. GR1 CCs are believed to be quenched strongly in the presence of other centers. The passive Q-switching of the Ruby laser was achieved using GR1 centers in natural diamond in 1995 [39]. Although the absorption saturation characteristic of GR1 center at 694 nm was studied in [39], a complete picture of the saturation behavior is not known yet.

Raman lasers in backscattering geometry are highly efficient and easy to arrange it in a gaseous medium. However, the threshold for backscattering amplification is very high typically above the optical damage threshold of most of the solid-state crystals. In general, and output characteristic strongly requires single-frequency pump radiation.

Common ways to generate energetic short pulses are Q switching and mode-locking methods. But Q-switched pulses are 5-10 ns and more while mode-locked regime results in the picosecond to femtosecond pulses. So sub-nanosecond pulse (<1ns) regime is difficult to achieve. In general, ultrashort pulse lasers like picoseconds and femtoseconds have spectrally broad linewidth which limits its application in the field that requires narrow linewidth. Also, laser systems capable to operate in temporal regimes ranging from several hundreds of picoseconds to sub-nanoseconds are very intricate and expensive.

## 1.8 Objectives of Research

The purpose of the present study is to explore and determine the possibilities of using color center diamond crystals as laser gain media capable to cover visible to near-infrared (550 nm to 1050 nm) spectra range as well as their potential application as saturable absorber media. Also, since undoped diamond crystals are unique Raman media, it is of great interest to study the effects of Raman lasing in forward, backscattering, and distributed feedback scattering geometries. Stimulated Raman scattering (SRS) can also be an effective means for the generation of new wavelengths, attain pulse shortening of Stokes pulses with respect to the pump pulses arising from pulse reshaping [46].

In this work, we considered two charge states of NV centers (neutral and negative) and a neutral vacancy center GR1 in diamond for the study. Their unique properties can be exploited in many photonics and optoelectronics applications. We studied and evaluated the possibility of their use as an active, photoluminescence, and Raman gain medium, as well as a saturable absorber for passive Q-switching. Our major objectives are listed below:

- Study and characterize NV center's various spectroscopic and laser properties, as well as photoionization dynamics at several wavelengths
- Test lasing effect in  $NV^-$  centers under pumping using pump pulses at different wavelengths.
- Construct a model using this information that explains the mechanisms of the population of the excited level and photoionization and recombination dynamics of  $NV^-$  and  $NV^0$  centers.
- Perform detailed characterization of spectroscopic properties and obtain parameters such as absorption, emission cross-sections, radiative lifetime, the efficiency of quantum yield under visible excitation, and conduct laser experiments, of GR1 centers.
- Study linear and non-linear optical properties and excited state dynamics of GR1 centers and test possible lasing effects.
- Use this information to construct a model and compare possible ESA at different wavelengths of several diamond samples with different GR1 concentrations.
- Utilize unique Raman properties of diamond crystal and get Raman laser with high output efficiency.

- Compare output performance of Raman lasers in different cavities and dependence of pulse shortening on cavity parameters.
- Test the possibility of stimulated Raman amplification in backscattering geometry and obtain picosecond to sub-nanosecond single pulses.
- Study diamond Raman laser in a simple distributed feedback geometry and achieve pulse shortening to sub-nanosecond time scale.

This thesis contains five chapters including the current Chapter 1 Introduction where all the detail about the background, properties, problems statements, and objectives are discussed. In chapter 2, a detailed characterization of the spectroscopic and laser properties of NV centers is discussed. Similarly, photo-induced ionization dynamics of NV centers between negative and neutral charge states is investigated at different wavelengths and different pump intensities, and a model describing the observed features is presented. Chapter 3 reports on various spectroscopic properties (absorption and emission band, transition cross-sections, radiative lifetime), and non-linear laser properties like absorption saturation, and relaxation dynamics using absorption saturation and pump-probe kinetics of GR1 samples. It also discusses our unsuccessful attempts to obtain lasing in GR1 using several cavity resonators. Later the same cavity setup was used with LiF:  $F_2^{+**}$  color centers as the gain medium and lasing were successfully realized. The fourth chapter is based on the study of output power and temporal profiles of Raman Stokes laser using undoped diamond crystals in different cavities. It also includes results on backscattering and

distributed feedback geometry of pumping. The last chapter includes a summary and conclusions of all chapters and future implementation of the conducted work.

## CHAPTER 2

### PHOTO INDUCED IONIZATION PROCESSES IN $NV^0$ AND $NV^-$ CENTERS

#### 2.1 Application of $NV^0$ and $NV^-$ Centers in Photonics

Among numerous color centers in diamond, the nitrogen-vacancy (NV) center is the one that drew the most interest. The negatively charged nitrogen-vacancy centers in diamond exhibit optically induced spin polarization which attracts a lot of attention in many fields of applications. The stable photoluminescence (PL) and optically measurable and controllable spin states of  $NV^-$  centers underpin many exciting applications of the  $NV^-$  center in fields such as magnetic sensing, biological imaging, quantum information processing, ultrasensitive nanoscale magnetic field sensing, nanoscale imaging magnetometry, and so on [47–51]. Nanodiamond with NV centers has been studied for several biomedical applications due to their inherent biocompatibility and low cytotoxicity [52]. NV center is a solid-state qubit with a favorable coherence time at room temperature ( $\sim 1$ ms), which is very important in quantum computation. The control of the quantum qubit is largely dependent on the electronic structure and charge state of the NV centers, radiative and non-radiative transition rates between two charge states, and coupling of these states with the external laser field. The laser application and quantum bit operation and readout work via optical excitation; thus, understanding the absorption and dynamics of relaxation from the excited state are highly important [49]. Moreover, interesting laser properties such as high gain coefficient, large emission, and absorption cross-sections, high quantum

efficiency and photo-thermal stability, make NV color centers promising as laser-active optical centers.

Despite the first successful lasing achieved on H3 color centers (at 530 nm) in natural and synthetic diamonds and recent success of diamond Raman lasers [37], demonstration of cavity coupling and realization of an NV laser has not been demonstrated so far in the peer-reviewed journal [40]. Also, the charge state dynamics of the nitrogen-vacancy (NV) center in diamond under intense pulse illumination plays a key role in a wide range of applications, yet this area of physics is poorly understood. In this chapter, we quantitatively investigate laser characteristics and photoionization dynamics between two charge states of NV centers using ns-pulse excitation and transmission of CW probe at various wavelengths.

## 2.2 Introduction to $NV^0$ and $NV^-$ Centers

NV center occurs in more than one charge state and among them two charge states namely, neutrally charged  $NV^0$ , with a zero-phonon line at 575 nm (2.156 eV) and negatively charged,  $NV^-$ , with a zero-phonon line at 637 nm (1.945 eV) are detected with optical excitation [45]. The NV center consists of a substitutional nitrogen atom adjacent carbon vacancy in the diamond lattice as shown in Figure 2.1. In the figure, a nitrogen atom substituting a carbon atom is shown by the purple sphere and the neighboring carbon vacancy by a white sphere. The center has trigonal  $C_{3v}$  symmetry with the substitutional nitrogen-lattice vacancy pair oriented along diagonal [111] direction which also can be seen in Figure 2.1 [8,53,54].

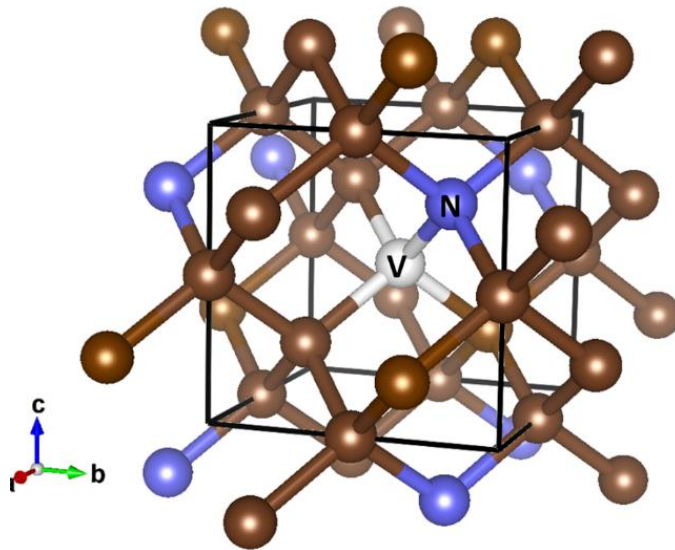


Figure 2.1 Diamond lattice is shown by a cube (black outline) with NV center where substitutional nitrogen (purple sphere) and a vacancy (white sphere) are adjacent to each other.

The electronic structure of NV centers is built from three electrons from the neighboring carbon bond electrons and two electrons from the substitutional nitrogen for the neutral charge state  $NV^0$  and one more electron from some donor centers for the negative charge state  $NV^-$  [53]. Both charge states can be detected and observed in diamonds under optical excitation. The ground and excited states of  $NV^-$  centers are spin triplets ( $S=1$ ) with principle zero-phonon line (ZPL) at 637 nm (1.945 eV), and phonon-assisted sidebands of the fluorescence extend up to 800 nm. The corresponding radiative transition is  ${}^3E \rightarrow {}^3A_2$  with a lifetime of 12 ns [42,55,56]. Similarly,  $NV^0$  has total spin ( $S=1/2$ ) and the spectrum of  $NV^0$  has a zero-phonon line located at 575 nm and is accompanied by strong Stokes shifted vibronic bands extending up to 750 nm for transition  ${}^2A \rightarrow {}^2E$ .

The current understanding of mechanisms involved in photochromism of the NV centers is schematically illustrated in Figure 2.2. The excited state energy level of  $NV^-$  is situated only  $\sim 0.6$  eV below the conduction band (CB) of the diamond. Because of this vicinity, with the absorption of the second photon the excited electron can be promoted to the CB, instead of decaying radiatively (red arrow line) or non-radiatively (yellow dashed line) back to the ground state  $^3A_2$ , thereby photoionizing  $NV^-$  centers to  $NV^0$  centers in the ground state and leaving a free electron in the CB. During the reverse process,  $NV^0$  absorbs one photon to bring the electron to the excited state, and a second photon brings an electron from the valence band (VB) to the ground state of  $NV^0$ , ionizing it to  $NV^-$  and leaving a hole behind in the VB [45,50,53,57,58].

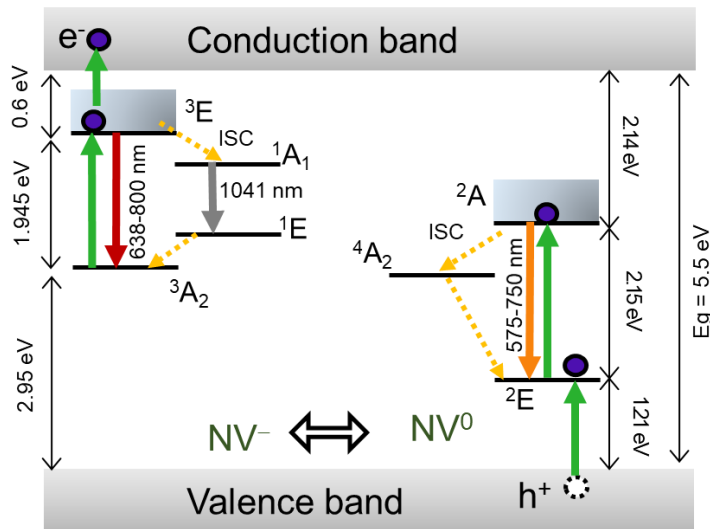


Figure 2.2 Energy level of  $NV^-$  and  $NV^0$  centers in the band gap of diamond and two-step photoionization mechanism of  $NV^-$  and  $NV^0$  centers. Energy separations between two energy states are shown by double-sided arrows. Single arrow line shows optical transition (absorption and radiative decay) and dashed arrow lines show non-radiative decay via intersystem crossing (ISC).

On the top of thermal stability of  $NV^-$  centers and stable luminescence associated with  ${}^3E \rightarrow {}^3A_2$  transition,  $NV^-$  centers have a high emission cross-section [59–62], ~99% quantum efficiency of fluorescence [42,56,59,60]. Hence, one can assume that  ${}^3E \rightarrow {}^3A_2$  transition of  $NV^-$  centers could have been a potential channel for laser action [59,63]. However, competing photoionization (PI) processes or ESA in  $NV^-$  centers, may mitigate lasing action of the center [53].

In 2019, the authors of [40] reported on the detection of stimulated emission from NV centers in diamond. They observed both spectrally- and time-resolved spontaneous emission reduction of  $NV^-$  centers under probe laser pulse at wavelengths in the phonon side band (PSB) and interpreted that as a result of stimulated emission in the PSB. Also, the transition from stimulated emission to photo-ionization was observed when the stimulating laser wavelength was reduced from 700 nm to 620 nm. It was also shown experimentally that light with a wavelength above 650 nm does not induce net photoionization of  $NV^-$  centers. The photoionization between  $NV^-$  and  $NV^0$  has been shown to be induced by strong light pulses. The results are based on indirect implication where reduction in ZPL intensities of NVs was attributed to the possible stimulated process of  $NV^-$  centers. However, the possibility of direct measurement of optical gain and lasing using NV centers is still elusive [40]. In the current research, we studied various laser-related optical properties of NV centers and dynamics of optical excitation and relaxation at different wavelengths. For that, we performed absorption saturation and pump-probe experiments using a diamond sample with  $NV^-$  color centers to clarify the suitability of diamond with  $NV^-$  centers for lasing.

### 2.3 Description of Sample Preparation

The employed sample to study NV center ionization dynamics was a bulk diamond grown by micro-plasma enhanced chemical vapor deposition (CVD) technique by Element Six (UK) Ltd. The substitutional initial nitrogen concentration [N] was provided to be 200-300 ppm. The sample was electron irradiated and annealed several times at various temperatures ranging from 400 °C to 1200 °C to remove an interstitial carbon, create NV centers by mobilizing vacancies and anneal out additional vacancy clusters [61]. The sample was of size  $0.29 \times 3 \times 3 \text{ mm}^3$  and was polished on both  $3 \times 3 \text{ mm}^2$  facets. It has a very deep purplish-pink coloration.

The sample was highly concentrated with roughly a uniform distribution of centers throughout the crystal volume and maintained good optical quality. For many quantum applications, single isolated NV centers are typically studied. Samples with sparse NV single centers or samples with a small concentration are required in order to obtain a precise and accurate readout. However, for bulk laser applications, NV ensembles with large numbers of centers are beneficial to reach maximum possible gain and efficient laser operation.

### 2.4 Room Temperature Absorption Measurements

Room temperature transmission spectra were measured at room temperature using Shimadzu UV-VIS-NIR-3101PC spectrophotometer. The measured spectrum corrected to the Fresnel reflection is depicted in Figure 2.3(A) and was taken through 0.29 mm path-

length at a slow-scanning speed of 100 nm/min with 1 nm spectral resolution. The corresponding absorption spectrum is shown in Figure 2.3(B). An absorption profile of pure CVD grown diamond near the band gap edge was taken as a baseline and was subtracted from the measured absorption spectrum [64]. The resultant absorption coefficient ( $k$ ) is presented in units of  $\text{cm}^{-1}$ . In Figure 2.3 (B), the absorption band spanning over 500 - 660 nm with a peak at  $\sim 576$  nm is due to  $\text{NV}^-$  centers. The absorption coefficient is  $k \sim 137 \text{ cm}^{-1}$  near the maximum of  $\text{NV}^-$  absorption. Given the fact that there is a very high concentration of nitrogen in the sample, it is obvious that the nitrogen impurities are present not only as a single substitutional center but also as aggregate centers. We believe that the additional absorption band appeared with a maximum at around 380 nm and positioned in the UV region is due to the absorption of  $\text{N}_3$  centers (a vacancy surrounded by three substitutional nitrogen atoms). The absorption coefficient near the peak of this band was measured to be  $k \sim 150 \text{ cm}^{-1}$  [37].

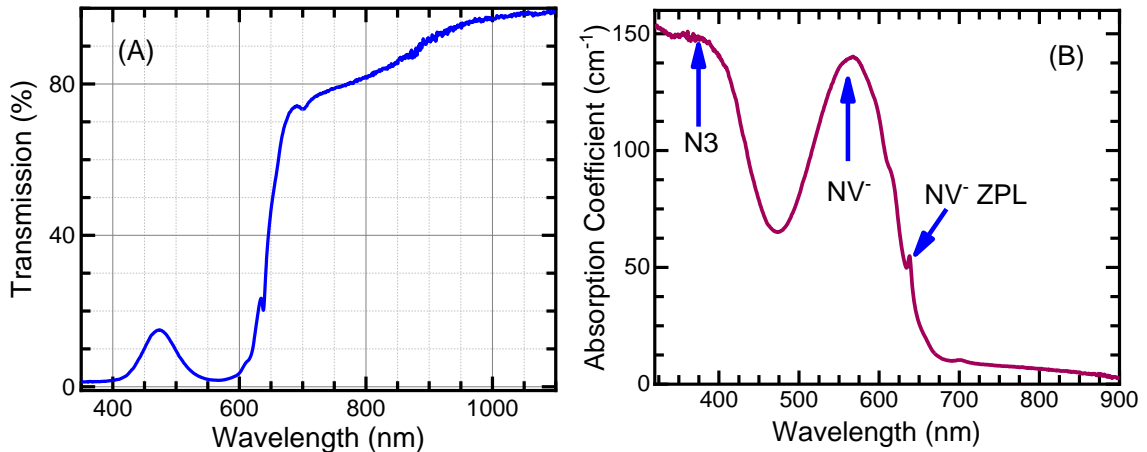


Figure 2.3 (A) Transmission spectrum of the sample at room temperature through 0.29 mm side and corrected to Fresnel reflection loss, (B) Corresponding absorption spectrum showing absorption bands of  $\text{NV}^-$  and  $\text{N}_3$  color centers.

## 2.5 Room Temperature Photoluminescence Measurements

### 2.5.1 Emission Spectra under Pulsed and CW 532nm Pump Excitations

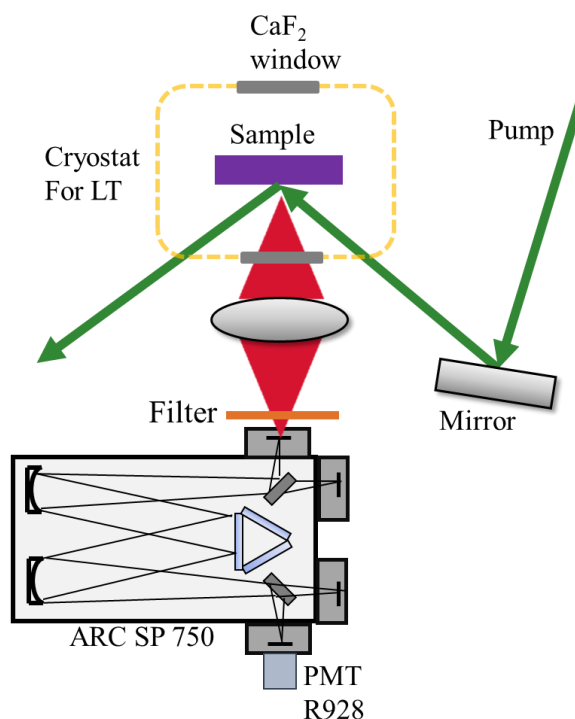


Figure 2.4. Design of the experimental setup to conduct luminescence measurements. For low-temperature measurements, the sample was placed in a closed-cycle cryostat which is capable to tune the temperature down to 10K.

The emission spectra of the NV centers were studied under pulsed and continuous wave (CW) 532 nm laser excitation. The second harmonic (532 nm) of Spectra-Physics Quanta-Ray Nd:YAG Q-switched pulsed laser operating at 10 Hz repetition rate and a diode-pumped solid-state (DPSS) Nd:YAG CW laser emitting at 532 nm was employed as the excitation sources. The measurements were carried out using Acton Research Spectra-Pro 750 monochromator which had a triple grating turret with monochromator/spectrograph of 750 mm focal length. A photomultiplier tube (Model

R928 from Hamamatsu) was used as a detection platform which has a sensitivity over 400 - 900 nm spectral range. The signal collected by PMT was further integrated and amplified using Boxcar gated integrator (Stanford Research System Model# SR 250) and lock-in amplifier (EG&G Model# 7260 DSP) to increase the signal to noise ratio, respectively, for pulsed and CW excitations. Optical long pass filters (orange) with cut-on wavelength at 550 nm were mounted at the entrance slit to eliminate the overlap of the pump and second-order diffraction signal with the emission spectrum.

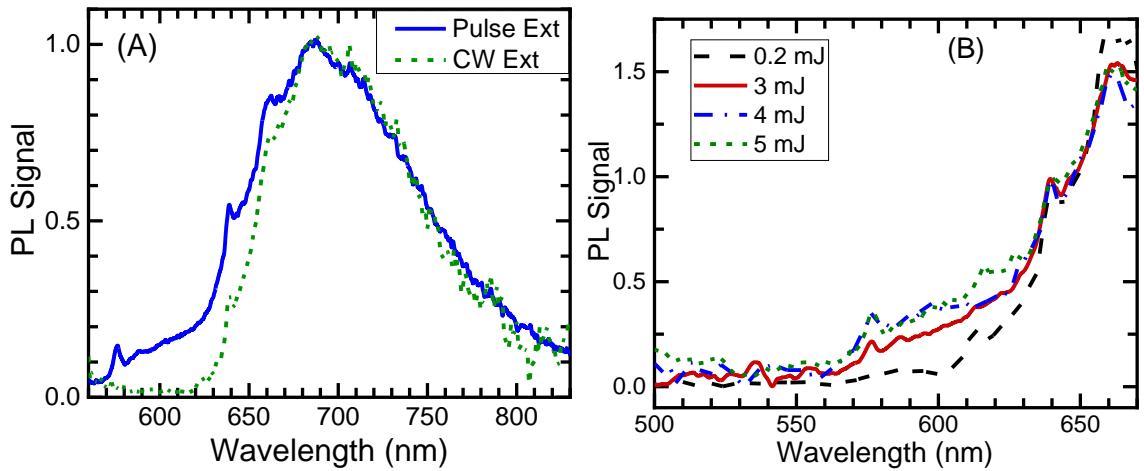


Figure 2.5. (A) The calibrated emission spectra were measured under CW (red solid curve) and pulsed (blue dashed curve) 532 nm excitations and normalized to 1 for comparison. Under pulsed excitation, some of  $NV^-$  centers are photoionized to  $NV^0$  showing ZPL at 575 nm and associated vibronic band. (B) Emission spectra (500 to 670 nm) normalized at  $NV^-$  ZPL ( $\sim 638$  nm) at different pulsed pump energies.

The normalized fluorescence spectra of the sample with  $NV^-$  center ZPL at 638 nm and a wide phonon-assisted side band with a maximum at  $\sim 700$  nm under 532 nm CW excitation (green dotted curve) and pulsed excitation (blue solid curve) are shown in Figure 2.5 (A). The measured PL spectra were calibrated with respect to the sensitivity of the used

spectrometer-detector combination using 45W Quartz Halogen Tungsten Lamp (Oriel standard calibration lamp model# 63358) and normalized to 1. The average pump power for both CW and pulse excitations was ~100 mW. During the pulsed excitation, the emitted signal was integrated during gate width of 5 ns and delay of 100 ns after the trigger. For the CW luminescence measurement, the signal was chopped by using a mechanical chopper and amplified using a lock-in amplifier at 20 mV sensitivity. The entrance and exit slits were open to ~250  $\mu\text{m}$  during both measurements.

Due to a high peak intensity of the pulsed beam, the intensity of ZPL of  $\text{NV}^-$  decreases while ZPL of  $\text{NV}^0$  at 575 nm starts to appear. Because of the heavily available donor, substitutional nitrogen (Ns), all the NV centers essentially are in a negative charge state which can be seen in the emission spectrum under CW excitation. The  $\text{NV}^0$  ZPL and its vibronic band are completely absent in this case. This suggests the photoionization (PI) of  $\text{NV}^-$  to  $\text{NV}^0$  which is accompanied by an increase of PL signal in the range of 575-630 nm due to the phonon-assisted side band of  $\text{NV}^0$  centers.

In Figure 2.5(B), we compared the emission profile in 500 nm to 670 nm spectral range under different energies of the pump pulse. For the very small pump pulse (0.2 mJ),  $\text{NV}^0$  emission is not visible. As the pump energy increases from 0.2 mJ to 5mJ, the strength of ZPL of  $\text{NV}^0$  centers and its PSB increases, and that of  $\text{NV}^-$  slightly decreases. The measurements had shown the enhancement of ZPL of  $\text{NV}^0$  centers and PSB with the increase in the pulse pump power. These results imply the existence of threshold pump intensity for photoionization. Our results are in agreement with the results published in N.

Aslam et al (2013) and L. Hacquebard et al (2018), where authors reported a strong dependence of PI rate on the input pump power and the wavelength [53,58].

### *2.5.2 Low-Temperature PL Spectra and Kinetics Measurements*

Spectroscopic characterization of photoluminescence was performed at low temperature (12K) using the setup shown in Figure 2.4 using the Acton Research monochromator SP 750 and R928 PMT detector. The sample was mounted in the Helium close-cycle cryostat and vacuumed down to  $10^{-6}$  torr with the help of turbo molecular vacuum pump. In the normalized emission spectra of  $NV^{-}$  center under pulsed excitation at 532 nm are presented. The pump energy used for the measurement was 10 mJ. The grating used had 600 grooves per millimeters (gmm) and the signal was integrated for gate width of 6 ns and 100 ns gate delay. We can see a sharper ZPL at 638 nm than that at room temperature. DFT calculations showed that quasi-local vibration modes appear at about 65 meV in which the carbon and nitrogen atoms vibrate the most around the vacancy and these modes appear in the absorption and PL spectra as bump features [49]. Upon comparing room and low-temperature spectra measured under pulsed excitation with pump  $\sim 10$  mJ (see Figure 2.5(A) and Figure 2.6), we can see a significant reduction in the vibronic side band of the  $NV^0$  centers at 12K. The relative intensity of ZPLs of  $NV^0$  is much smaller ( $\sim 5$  times) than that of  $NV^{-}$ . However, the ratio of ZPLs was about the same for spectra measured at room temperature. That suggests a smaller rate of photoionization of  $NV^{-}$  to  $NV^0$  at low temperature.

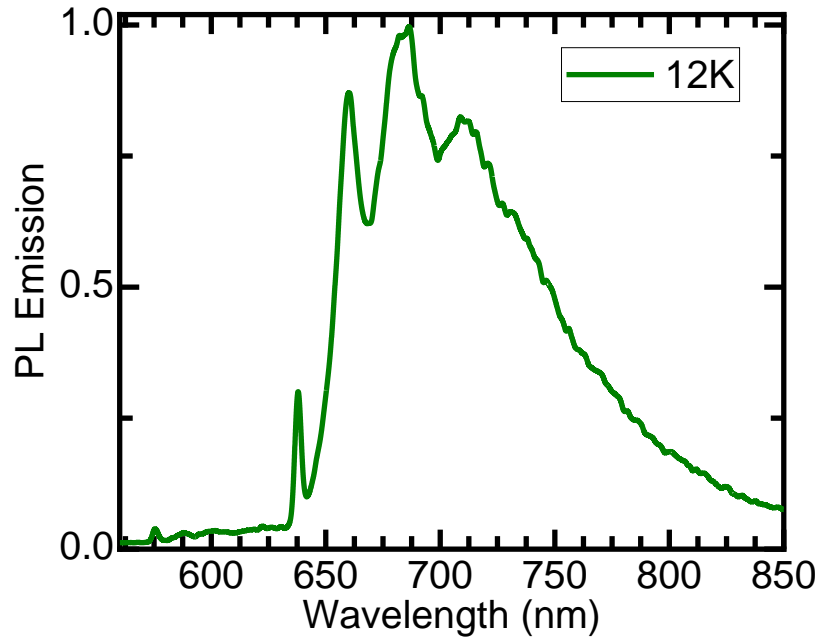


Figure 2.6 The emission spectrum of NV centers at low temperature (12K) under 532nm pulsed excitation, which is calibrated to the sensitivity of detection platform used and normalized to 1.

The temporal profile of PL decay was measured at temperatures ranging from 12K to 300K. We studied the kinetics of the PL signal at different wavelengths and determine the temperature dependence of the total lifetime of the excited states of  $NV^0$  and  $NV^-$ . The 532 nm pulsed excitation with a pulse duration of 10 ns was utilized. In this case, the pump pulse was shorter than the excited state lifetimes of both charge states of the NV centers as provided in the literature. The setup used for the kinetics measurements was similar to that shown in Figure 2.4. The photomultiplier tube R928 is again used to detect the signal which has a rise time of 2.2 ns. The resulting waveforms after pump excitation are recorded using a 1 GHz oscilloscope and are illustrated in Figure 2.7(A), (B), and (C).

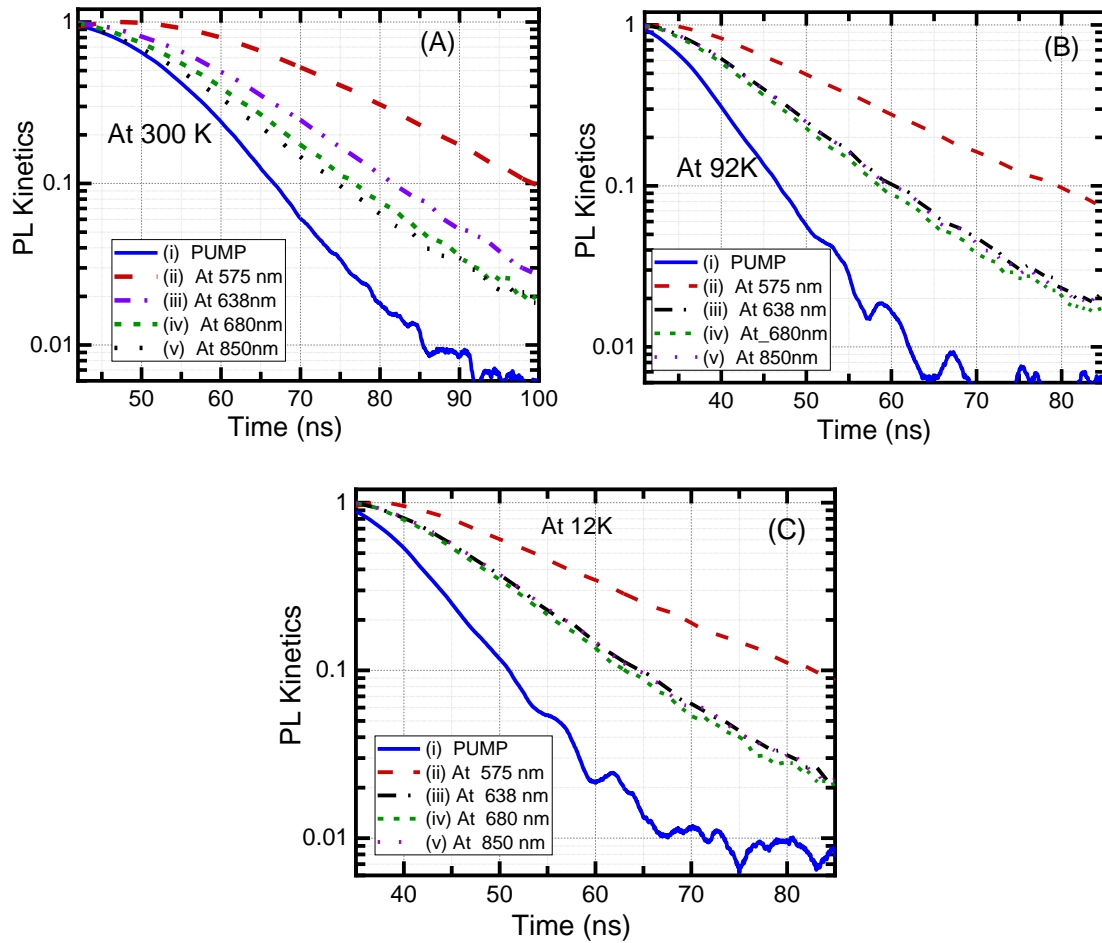


Figure 2.7 PL kinetics of NV centers in diamond under 532 nm pulsed excitation (i) at pump beam wavelength, (ii) at 576 nm (near the ZPL of  $NV^0$  centers), (iii) at 638 nm (near the ZPL of  $NV^-$  centers), (iii) at 680 nm (near the peak of emission band), (iv) at 850 nm (near the tail of PL spectrum) measured at (A) 300K (room temperature) (B) 92 K, and (C) 12K.

The lifetimes were measured at different wavelengths by placing the grating in the monochromator at that specific wavelength setting and using the Spectrasense PC software. The decay lifetimes measured at 576 nm (ZPL of  $NV^0$  centers), 638 nm (ZPL of  $NV^-$  centers), 700 nm (near the maximum of emission band), and 850 nm (near the tail of emission band) are estimated from measurements and are presented in Table 2-1. The blue

curve shows the temporal profile of the pump radiation measured at the pump wavelength, which represents the Gaussian lineshape. All the PL kinetics show a single exponential decay with a lifetime of 18.8 ns at room temperature (330K) near 576 nm, which is close to the reported lifetime of 19 ns of  ${}^2A \rightarrow {}^2E$  transition of  $NV^0$  center [58]. Similarly, the PL decay lifetime of  $NV^-$  corresponding to the transition  ${}^3E \rightarrow {}^3A_2$  at room temperature was estimated to be 12.4 ns which is close to the 12 ns lifetime of  $NV^-$  centers reported in the literature [40,56]. These results further support the ionization of  $NV^-$  centers under pulsed 532 nm excitation. If we compare the lifetimes at different wavelengths, there is not much temperature quenching of both charge states meaning non-radiative relaxation is not very likely and quantum efficiency of luminescence of NV centers at room temperature is close to unity. Also, at low-temperature quantum efficiency approaches 100%, and that the measured lifetimes are approximately equal to the radiative lifetime.

Table 2-1. PL lifetimes of NV centers at different wavelengths and temperatures

Wavelengths	Measured PL lifetime ( $\tau$ )		
	300K	92K	10K
576 nm ( $NV^0$ )	18.8 ns	19.8 ns	19.8 ns
638 nm	14.8 ns	11.8 ns	11.7 ns
780 nm	12.4 ns	11.8 ns	11.7 ns
850 nm ( $NV^-$ )	12.4 ns	11.8 ns	11.6 ns

## 2.6 Estimation of Absorption and Emission Cross-sections

The absorption (green line) and calibrated emission bands (red line) of  $\text{NV}^-$  centers, corresponding to transition  ${}^3\text{E} \leftrightarrow {}^3\text{A}_2$ , are shown in Figure 2.8.

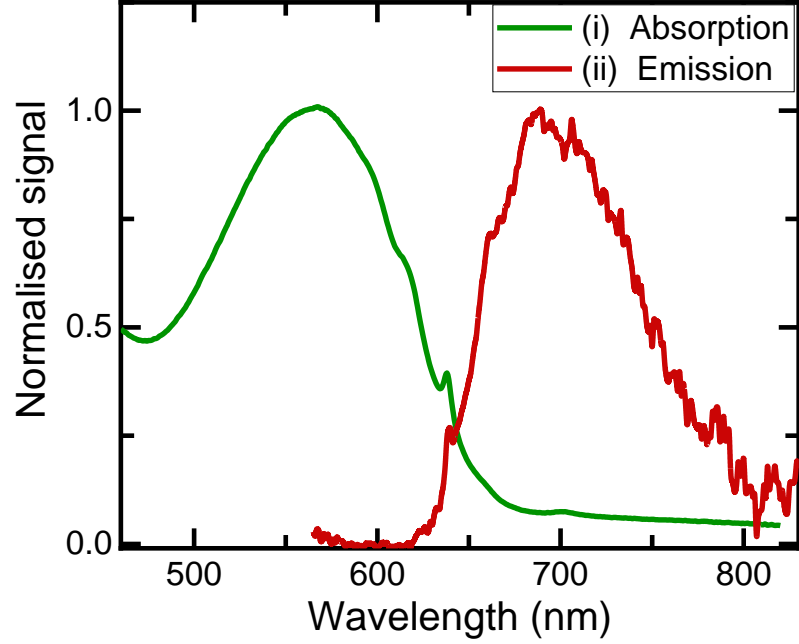


Figure 2.8. Room temperature absorption and calibrated emission spectra of the  $\text{NV}^-$  centers normalized to 1.

The measured emission spectrum and kinetics were further utilized to estimate the parameters associated with the  ${}^3\text{E} \rightarrow {}^3\text{A}_2$  transition to allow calculation of emission cross-section using the method adapted for Gaussian shape profiles [65]:

$$\sigma_{em}(v_{0,em}) = \frac{c^2 A_{21}}{8\pi n^2 v_{0,em}^2} g_{em}(v_{0,em}) \quad (2.1)$$

$$\sigma_{ab}(v_{0,ab}) = \frac{g_2}{g_1} \frac{c^2 A_{21}}{8\pi n^2 v_{0,ab}^2} g_{ab}(v_{0,ab}) \quad (2.2)$$

In equations (2.1) and equation (2.2),  $g_{em}(\nu_{0,em})$  and  $g_{abs}(\nu_{0,abs})$  are form-factors of emission and absorption bands, respectively, which are  $\sqrt{4\ln 2/\pi}/\Delta\nu$  at central frequencies for a Gaussian distribution, where  $\Delta\nu$  is full width at half maximum and  $A_{21}$  is Einstein's coefficient of spontaneous emission. As the quantum yield of  $NV^-$  centers in bulk diamond is close to unity as we see from our kinetics measurement as well as in literature ( $\phi \approx 1$ ) [51], we can use the decay lifetime  $\tau = 12.4$  ns obtained from PL kinetics to determine  $A_{21}$ . Moreover,  $n = 2.4$  is the refractive index of diamond, and  $g_1 = 1$  and  $g_2 = 2$  are degeneracies of the ground and excited states, respectively. The estimated value of absorption and emission cross-sections is  $2.8 \times 10^{-17} \text{ cm}^2$  and  $4.3 \times 10^{-17} \text{ cm}^2$  at the maximum of absorption and emission bands, correspondingly. We further calculated the absorption cross-section at the pump wavelength (532 nm) to be  $2.4 \times 10^{-17} \text{ cm}^2$  using the estimated value of absorption cross-section near the maximum of absorption band and measured absorption spectrum from Figure 2.3(B). Our result is within the error-bar with cross-section  $((3.1 \pm 0.8) \times 10^{-17} \text{ cm}^2)$  published in ref [66]. The stimulated emission cross-sections at the maximum are slightly larger than the reported value  $((3.6 \pm 0.1) \times 10^{-17} \text{ cm}^2)$  in ref [42], where it was calculated using the Füchtbauer-Ladenburg equation and used 13 ns as a radiative lifetime. The stimulated emission cross-section at the maximum reported in ref [62] is about 7 times higher than our estimated value. However, different fabrication procedures and different combinations of color centers could have some influence on inhomogeneous broadening and maximum emission and absorption cross-sections. Using the value of absorption cross-section at the peak and absorption coefficient

from Figure 2.3(a), the concentration of  $NV^-$  centers is found to be  $\sim 25$  ppm ( $4.5 \times 10^{18} \text{ cm}^{-3}$ ).

Table 2-2. Spectroscopic parameters associated with transition  ${}^3E \leftrightarrow {}^3A$  of  $NV^-$  color center in diamond.

Transition	Parameters	Symbol	Unit	Value
${}^3A_2 \rightarrow {}^3E$	Central wavelength	$\lambda_0^{ab}$	nm	558
	Bandwidth at FWHM	$\Delta\lambda_{ab}$	nm	130
	Cross-section at $\lambda_0^{em}$	$\sigma_{ab}$	$\times 10^{-17} \text{ cm}^2$	2.8
${}^3E \rightarrow {}^3A_2$	Central wavelength	$\lambda_0^{em}$	nm	703
	Bandwidth at FWHM	$\Delta\lambda_{em}$	nm	100
	Cross-section at $\lambda_0^{em}$	$\sigma_{em}$	$\times 10^{-17} \text{ cm}^2$	4.3

## 2.7 Absorption Saturation Under 532 nm Excitation

The experiments conducted above have shown a clear sign of strong photoionization of  $NV^-$  center under pulse excitation and its strong dependence on the input pump intensity or pump energies. The PI of neutral ( $NV^0$ ) and negative ( $NV^-$ ) charge states as well as possible ESA processes can play a major role in quenching the possible stimulated process and lasing. Hence, it is very critical to understand the dynamics of ESA and PI with changes in pump energy density. For this purpose, we performed absorption saturation experiments based on the measurement of the transmission of incident radiation through the sample for different incident energy fluences. In general, fractional absorption of incident light decreases with the increase of pump intensity, and the system should become more transparent to the incident light. At sufficiently high intensity (typically

above saturation intensity), the transmission will saturate and becomes relatively constant despite any further increase in intensity. This condition is reached when the density of pump photons is significantly higher than the density of the center concentration. If there is no other absorption process happening, then transmission of the pump will saturate at some level.

The experimental setup to conduct absorption saturation measurement is shown in Figure 2.9 (A). Here, we used a 532 nm pump pulse beam with a repetition rate of 10 Hz. The beam diameter of the pump beam at the sample was 1.6 mm which was measured by using the knife-edge measurement technique at the position of the sample. A combination of a half-wave plate and a Glan prism was used to vary the incident pump fluence. The incoming pump beam was split into two beams where Detector 1 (joule meter) would measure reference beam or input beam and Detector 2 (power meter) measures output or transmitted pump beam. First, measurements by Detector 1 and Detector 2 were calibrated without the sample at the position shown in Figure 2.9 (A). After calibration, the transmission of pump energy fluence is measured by taking the ratio of transmitted pump fluence through the sample and the incident pump fluence. The solid red curve (ii) in Figure 2.9 depicts transmission measured at different pump energy fluences. As pump energy increases, the transmission increases from its initial value of  $T_0 \approx 3\%$  and saturates at  $T_s \approx 10\%$  for higher energy fluence. Transmission is less sensitive at higher pump fluence ( $>100 \text{ mJ/cm}^2$ ). We compare our measured transmission with that predicted by the Frantz-Nodvik equation given in equation [67] and represented by a blue dashed curve (i).  $E_s(\nu) = h\nu/\sigma_{\text{abs}}(\nu)$  is saturation fluence calculated at pump wavelength 532 nm, whose

value is  $15.5 \text{ mJ/cm}^2$ , where  $\sigma_{\text{abs}} \approx 2.4 \times 10^{-17} \text{ cm}^2$  is the absorption cross-section at 532 nm measured using the absorption spectrum, and  $T_0 = 3\%$  is the initial transmission extracted from the transmission spectrum measured by spectrophotometer.

$$T = \frac{E_s}{E_{in}} \ln \left[ 1 + \left( e^{\frac{E_{in}}{E_s}} - 1 \right) T_0 \right] \quad (2.3)$$

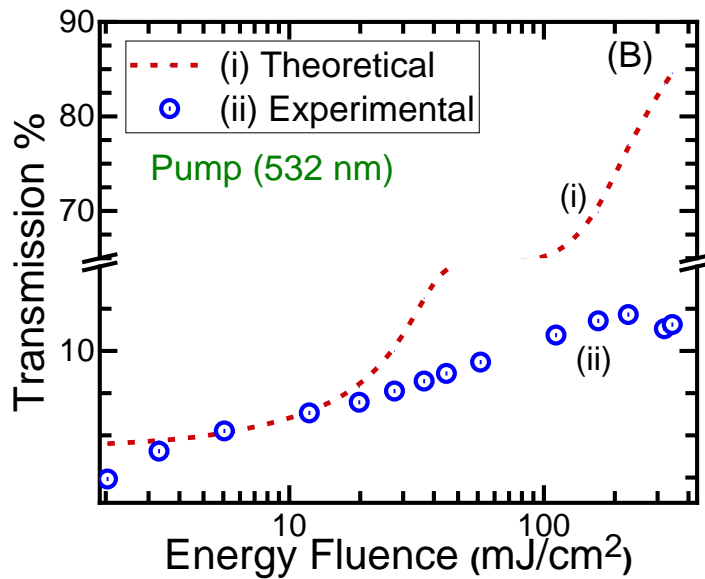
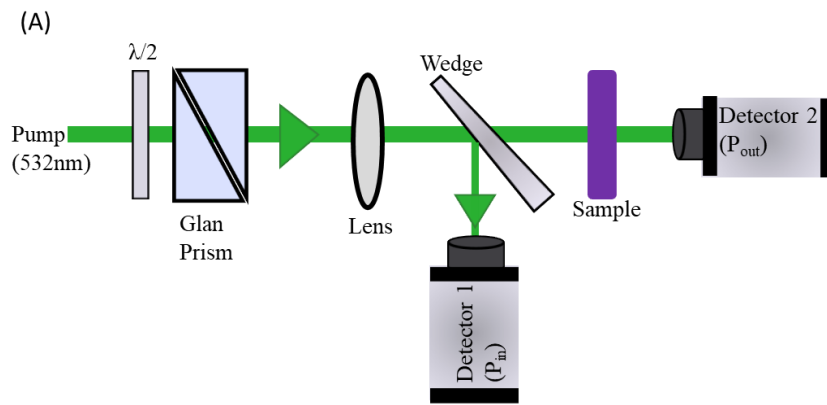


Figure 2.9. The experimental setup to conduct absorption saturation measurement (A). Variation of a 532 nm pump beam transmission through the sample as a function of a pump energy density (B) (i) calculated using Frantz-Nodvik equation (red dash) and (ii) measured (blue circles).

It can be seen from Figure 2.9 (B) that as pump energy density increases, the measured transmission strongly deviates from the values calculated using the Frantz-Nodvik equation. That suggests strong absorption of pump photon even after sufficient bleaching of  $NV^-$  ground state. One of the possible mechanisms could be induced long-term bleaching of the centers when an electron absorbs photons and is then trapped at some impurity center. That will decrease the overall concentration of NV centers. However, transmission spectra measured before and immediately after long 532 nm pulsed illumination did not show any changes. Another possible mechanism for such a small transmission is PI and/or ESA. The latter mechanism is further supported by photoionization of  $NV^-$  and formation of  $NV^0$  centers as illustrated in Figure 2.3(c).

## 2.8 Laser Experiments under 532 nm Pulse Excitation

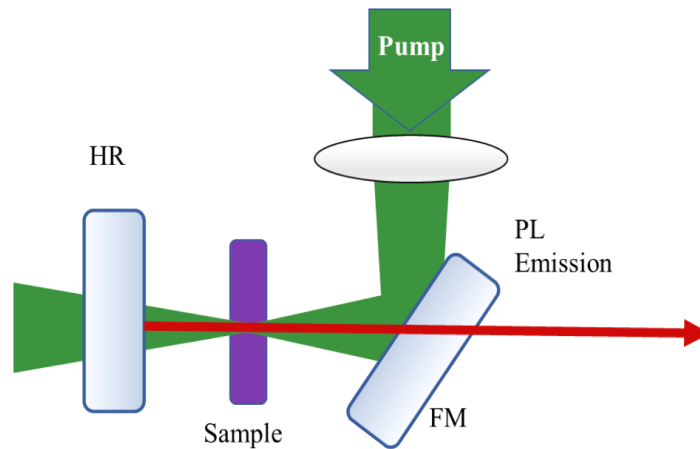


Figure 2.10. Cavity setup and pumping scheme used for laser oscillation under longitudinal pumping by 532 nm and 633 nm pulsed radiation. The Fabry-Perot resonator shown above was a flat-flat cavity made by a high reflector (HR) and Fresnel reflection (17%) from crystal surface as an output coupler.

We utilized several nonselective Fabry-Perot laser cavities and one of them is depicted in Figure 2.10. The flat-flat linear Fabry-Perot cavities were formed by HR ( $R > 99\%$  @ 600-800 nm) mirror and the Fresnel reflection (17%) from the output facet of the sample and had a cavity length of  $\sim 1$  cm. Diamond color center crystal of 2.9 mm thickness was used as a gain medium. Besides that, a semi-confocal cavity replacing the HR mirror with a gold-coated mirror of radius of curvature ( $r = 50$  mm) was also utilized to test the lasing. The sample was pumped with pulse radiation under second harmonics of Nd:YAG at 532 nm ( $\sim 8.5$  ns) operating at a 10 Hz repetition rate. Pump radiation was focused into the cavity by using a convex spherical lens to coincide with the cavity mode. The pump density  $> 560$  mJ/cm<sup>2</sup> was used to excite the centers which is about 30 to 40 times above saturation energy density (15.5 mJ/cm<sup>2</sup>) at pump beam wavelength. The cavity output was separated from the pump and taken out using a folding mirror (FM) shown in Figure 2.10 and measured using a fast Si-detector (rise time  $\sim 1$  ns) and the power meter. The spectral profile of cavity output of the NV<sup>-</sup> centers emission was also measured at different pump densities and compared using monochromator SP 750 and PMT R928.

However, we were not successful in detecting stimulated emission or lasing under 532 nm pumping. We tested laser oscillation at different focusing conditions of the pumps and different stable cavity lengths and optimized feedback and minimize loss by fine-tuning of samples and cavity mirrors.

## 2.9 Pump-Probe Experiment at Different Probe Wavelengths

It is well established that photoionization rates between  $NV^-$  and  $NV^0$  centers strongly depend on the laser field wavelength [40,53,58]. To study the dynamics of absorption at possible oscillation wavelengths after excitation, we performed a pump-probe experiment using 532 nm pump pulses and two CW probe beams at 632 nm (HeNe laser) and 670 nm (fiber-pigtailed diode laser). The temporal resolution of the pump-probe experiments was larger than the upper-level lifetime of both  $NV^0$  and  $NV^-$  centers ( $\sim 20$  ns).

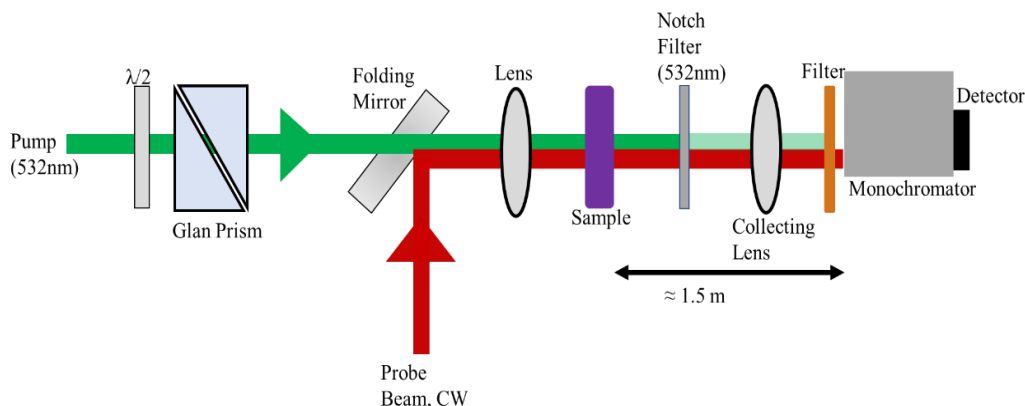


Figure 2.11. Schematic diagram of the pump-probe experiment where the direction of pump pulse and CW probe are shown by green and red arrow line, respectively.

The schematic diagram of the optical setup utilized for the pump-probe experiment is shown in Figure 2.11. The second harmonic of Nd:YAG pulsed pump laser radiation of 7 mJ average power with 10 Hz repetition rate along with the CW probe beams of  $\sim 5$  mW power was utilized. The beam size of the green pulse near the sample was measured to be 1.6 mm in diameter, which gives  $\sim 350$  mJ/cm<sup>2</sup>/pulse energy density. This is the range of the pump densities where the absorption of the pump saturates (see Figure 2.9). Such a high energy density would activate any long-lived kinetics induced by localizing electrons

at trap centers if any present. A series of optical filters and notch filters were used to block the scattered pump beam from the detector. The transmitted signals at probe beam wavelengths were measured by the Spectrapro-300i monochromator along with a PMT detector (PM tube R928 from Hamamatsu in housing PD439 from Acton Research Corporation)) and recorded by an oscilloscope.

Figure 2.12 (A) and (B) show the decay dynamics of the signal measured at 632 nm probe wavelength at the different temporal range, where curves ‘i’ represent the steady-state transmission of CW probe beam (632 nm HeNe) and curves (ii) show induced change in transmission of the probe beam due to the pump excitation. For the curves (i) measurements pump beam was blocked by a beam dump and allowed the probe to transmit through the sample. Similarly, for curves (ii) measurements, both pump and probe beam are sent collinearly. Measured transmissions in Figure 2.12 (A) and (B) were corrected for Fresnel reflection, which is ~17% from each crystal surface and 34% in total. Steady-state transmissions of 632 nm, curves (i), are consistent with the initial transmissions measured using a spectrophotometer (see Figure 2.3(A)). In the presence of the 532 nm pump pulse, the transmission of the 632 nm probe beam increases from the initial value ~26% to ~40%.

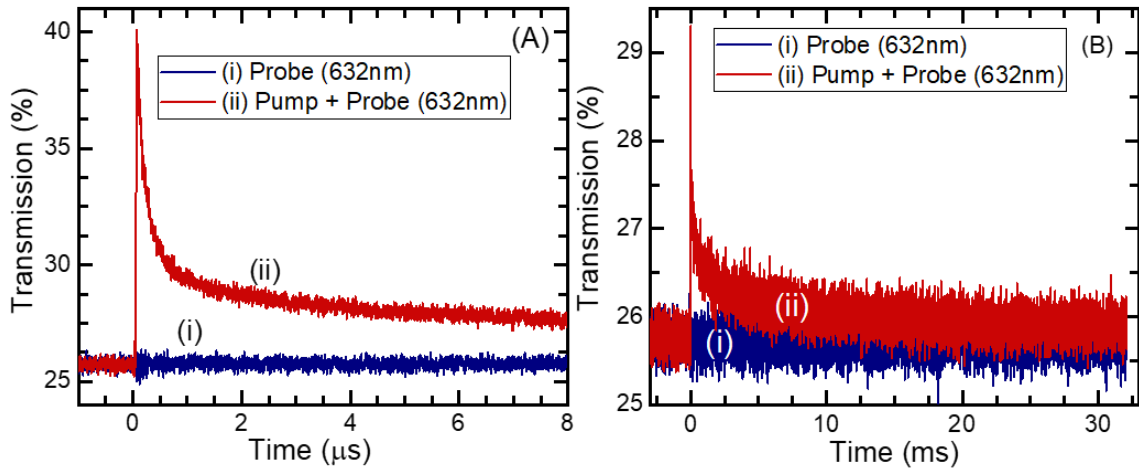


Figure 2.12. Signal measured at probe beam wavelength at 632 nm using (i) 532 nm pump beam and probe beam simultaneously, (ii) probe beam only (after blocking the 532 nm pump beam) in (A) microsecond time scale and (B) millisecond time scale.

The pump-induced change in transmission of the probe beams gives the picture of the temporal evolution of the population density of the corresponding center. Since absorption of  $NV^0$  at 632 nm is close to zero, as one can see from Figure 2.3(A), the absorption of the probe beam at 632 nm is primarily the result of  $NV^-$  centers and could be used to test the dynamic of the  $NV^-$  centers concentration. In addition, the kinetics at 632 nm Figure 2.12(A) and (B)) reveals a multi-exponential behavior with “fast” decay and “slow” decay channels. There is no residual absorption between the pulses of 100 ns.

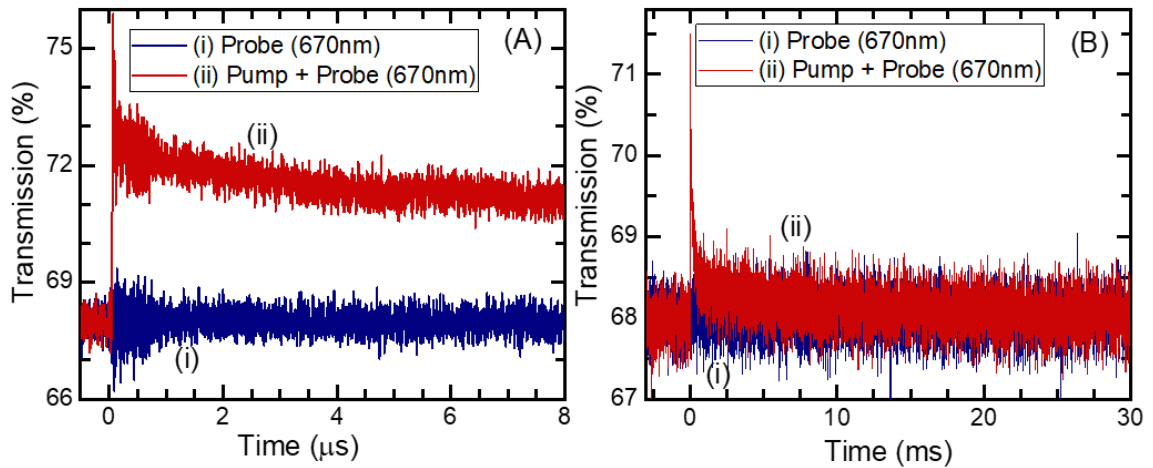


Figure 2.13. Signal measured at probe beam wavelength at 670 nm using (i) probe beam only (after blocking the 532 nm pump beam) and (ii) 532 nm pump beam and probe beam simultaneously.

On the other hand, 670 nm probe beam transmission increases from ~50% to ~56% after the pump pulse. A spike in Figure 2.13(A) curve ‘ii’ is overlapped with the NV<sup>-</sup> luminescence signal reaching the detector. There could be some influence of “parasitic photoluminescence signal” on the probe beam at this wavelength but it could be neglected completely after 20 ns of transmission kinetics. There is no relaxation stage kinetic at 670 nm corresponding to “fast” decay ( Figure 2.13(A) and (B)), implying that absorption at 670 nm is induced by another color center. We can see the transmission recovery to the steady-state level (curves (ii) in Figure 2.13(A) and (B) between the pulses (100 ms) for 670 nm kinetics. Centers recover to the initial level which implies no residual absorption or long-term bleaching (>100 ms) for a 10 Hz repetition rate. It is noteworthy that at both wavelengths, we observed an increase in the probe transmissions. This indicates that any induced absorption is smaller than bleaching due to the ionization process. The recovery time is different for two probe beams and the 670 nm signal recovers two times faster.

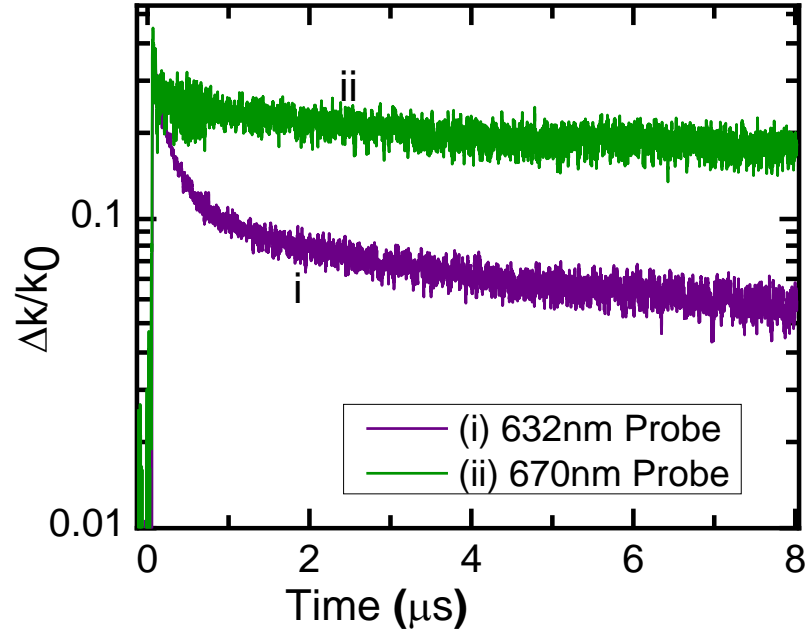


Figure 2.14. Comparison of the evolution of normalized  $\Delta k/k_0$  kinetics under 532 nm pumping at probe wavelengths (i) at 632 nm and (ii) at 670 nm.

The temporal recovery of the initial concentration of the ionized centers could be analyzed using  $\Delta k/k_0$  plots (see Figure 2.14), where  $\Delta k$  is the change of the absorption coefficient and  $k_0$  is the initial absorption coefficient at the probe wavelength. If there is only one type of center present,  $\Delta k/k_0$  ratio does not depend on cross-section and  $\Delta k/k_0 \sim \Delta n/n_0$  is the same for all wavelengths, where  $\Delta n/n_0$  represents fractional population inversion. The probe kinetics at 632 nm could be fit by two exponential curves with 250 ns and 12  $\mu$ s time constants. The fast decay time is close to the reported lifetime of the metastable level of  $NV^-$  centers [67]. The slow kinetics could be explained by the capture of the electron after ionization of  $NV^-$  centers by a deep trap followed by a slow recovery process. The recovery time of the absorption at 670 nm was calculated to be 24  $\mu$ s. Kinetics

of transmission of different probe beams show that the ionization and bleaching process involves different channels indicated by different recovery times.

### 2.10 Absorption Saturation Measurement under 633 nm Pump

As it is reported in many peer-reviewed articles, that the rate of PI is strongly dependent on wavelength and there is a switching between PI and stimulated process at 620 nm, we could get insight into some new aspects when changing pump wavelength to 633 nm. In an attempt to mitigate PI processes of  $NV^-$  centers, we decided to test a 633 nm pulsed laser pump as our new excitation source. This wavelength should excite  $NV^-$  but not  $NV^0$ , which could help mitigate the back-and-forth PI processes. Raman shifted radiation of the second harmonic of Nd:YAG laser from a deuterium cell at 633 nm was used for pumping. The pump source had a 10 ns pulse duration and operated at a 10 Hz repetition rate. We performed an absorption saturation measurement as described in section 2.2 and measured the transmission of the pump at different input intensities of 633 nm pump pulses. The measured transmission corrected for Fresnel reflection level is plotted as a blue circle in Figure 2.15. We compared our measured transmission with that predicted by the Frantz-Nodvik equation given in equation (2.3) [68] and represented by a red dashed curve 'i' in Figure 2.15. Saturation fluence is calculated using  $E_s(\nu) = h\nu / \sigma_{abs}(\nu)$  at pump wavelength 633 nm, whose value is  $30.2 \text{ mJ/cm}^2$ , where  $\sigma_{abs} \approx 1.1 \times 10^{-17} \text{ cm}^2$  is the absorption cross-section at 632 nm estimated using the absorption spectrum, and  $T_0 = 25.7\%$  is the initial transmission extracted from the transmission spectrum measured by spectrophotometer after correction to Fresnel reflection.

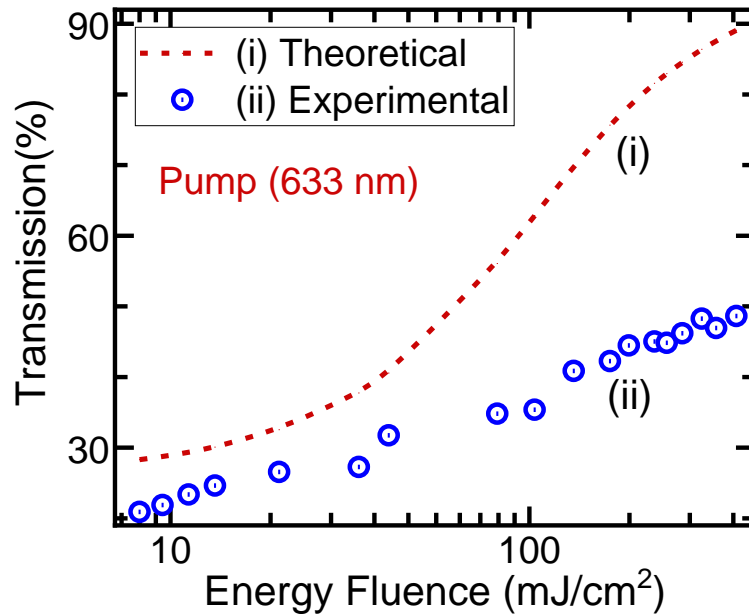


Figure 2.15. The dependence of 633 nm pump transmission through the sample as a function of a pump energy fluence (i) calculated using Frantz-Nodvik equation (red dashed line) and (ii) measured from the experiment (blue circles).

The saturated transmission level under 633 nm was significantly higher than that measured under 532 nm pumping (see Figure 2.9). The transmission at 633 nm increased from  $T_0 \approx 21\%$  to  $T_s \approx 48\%$  for pulses with energy fluence  $>300 \text{ mJ/cm}^2$ . We measured a strong saturation of the absorption at the 633 nm pump, which was stronger than that under 532 nm excitation. However, the saturated transmission near  $400 \text{ mJ/cm}^2$  is still  $\sim 2$  times smaller than it would be when calculated using the Frantz-Nodvik equation. It shows that the PI is still present. Furthermore, to detect any long-lived photoionization or bleaching of the centers, we measured transmission before and immediately after (within less than a minute) illumination of the sample under a 633 nm pump. We irradiated the sample at sufficiently high energy fluence ( $>3 \text{ J/cm}^2/\text{pulse}$ ), which is near the optical damage threshold, for about twenty minutes. Our measurement shows no change in the

transmission profile meaning no long-lived residual absorption. However, additional experiments are required to estimate the ratio of excited and ionized color centers.

We used a non-selective Fabry-Perot resonator consisting of a gold-plated concave mirror ( $R = 5\text{cm}$ ) working as a high reflector and polished facet of the sample as an output coupler (Fresnel reflection  $\sim 17\%$ ). The length of the cavity was  $\sim 3.5\text{cm}$ . The spectral profile of the  $\text{NV}^-$  centers emission did not show any notable change up to the pump energy density of  $0.5\text{ J/cm}^2$ .

### 2.11 Model Describing Saturation and Pump-Probe Kinetics

The results from the saturation and pump-probe experiments are summarized as follows:

- Variation of the transmission values at 532 nm from small pump signal to pulse energy density  $E = 350\text{ mJ/cm}^2$  was relatively small: from  $T_0 = 0.03$  to  $T_s = 0.1$ .
- The transmission values at 632 nm from small pump signal to pulse energy density  $E = 400\text{ mJ/cm}^2$  was measured to be  $T_0 = 0.20$  and  $T_s = 0.48$ , respectively.
- There was no excited state absorption at 632 nm and 670 nm probe wavelengths.
- The absence of the laser oscillation under 532 nm excitation indicates low population densities of the  $\text{NV}^0$  and  $\text{NV}^-$  color centers upper laser levels.

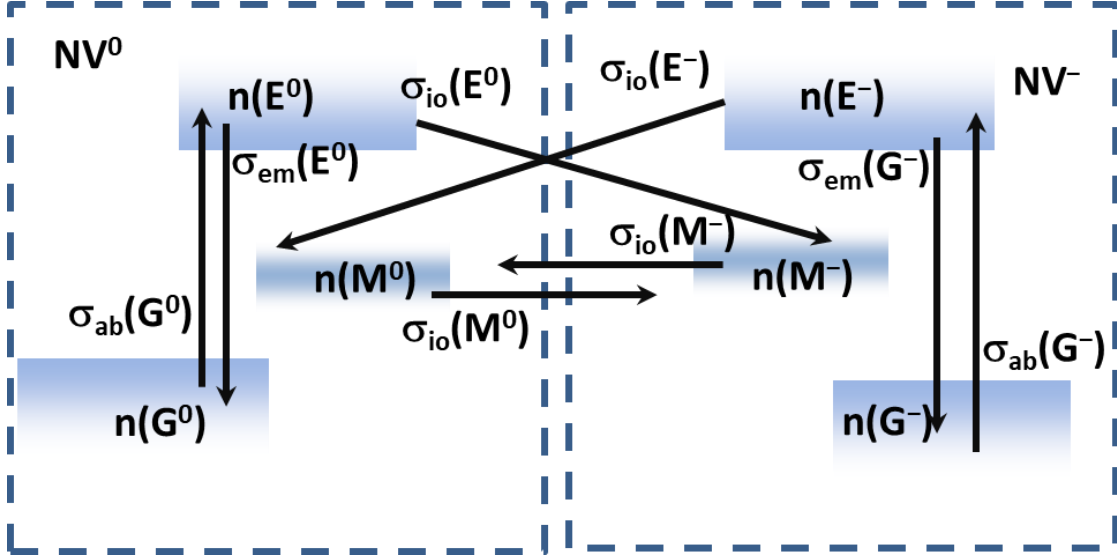


Figure 2.16 Illustration of the energy levels of  $NV^0$  and  $NV^-$  centers and corresponding population densities and cross-sections used to describe the proposed model of saturation and pump-probe experiments.

One of the models describing the results from the saturation and pump-probe measurements is shown in Figure 2.16. The proposed model considered both  $NV^0$  and  $NV^-$  centers as a three-level system. The rate equations that govern the rate of change of electrons on each level are:

$$\begin{cases}
 \dot{n}(G^0) = -I_p \sigma_{ab}(G^0)n(G^0) + I_p \sigma_{em}(E^0)n(E^0) \\
 \dot{n}(G^-) = -I_p \sigma_{ab}(G^-)n(G^-) + I_p \sigma_{em}(E^-)n(E^-) \\
 \dot{n}(E^0) = I_p \sigma_{ab}(G^0)n(G^0) - I_p \sigma_{em}(E^0)n(E^0) - I_p \sigma_{io}(E^0)n(E^0) \\
 \dot{n}(E^-) = I_p \sigma_{ab}(G^-)n(G^-) - I_p \sigma_{em}(E^-)n(E^-) - I_p \sigma_{io}(E^-)n(E^-) \\
 \dot{n}(M^0) = I_p \sigma_{io}(E^-)n(E^-) - I_p \sigma_{io}(M^0)n(M^0) + I_p \sigma_{io}(M^-)n(M^-) \\
 \dot{n}(M^-) = -I_p \sigma_{io}(E^0)n(E^0) + I_p \sigma_{io}(M^0)n(M^0) - I_p \sigma_{io}(M^-)n(M^-)
 \end{cases} \quad (2.4)$$

Where,  $n(G^0)$ ,  $n(E^0)$ ,  $n(M^0)$  and  $n(G^-)$ ,  $n(E^-)$ ,  $n(M^-)$  are densities at ground state (G), excited state (E), and metastable state (M) of  $NV^0$  and  $NV^-$  color centers,

correspondingly, where superscript denotes charge state of the center. Similarly,  $\sigma_{ab}(G^0)$ ,  $\sigma_{ab}(G^-)$  and  $\sigma_{em}(E^0)$ ,  $\sigma_{em}(E^-)$  are absorption and emission cross-section of ground and excited states of  $NV^0$  and  $NV^-$ , respectively. In Figure 2.16, arrows show all the possible excitation, emission, and PI paths for  $NV^0$  and  $NV^-$ , which we considered in our model. We consider only photo-induced processes and disregard relaxation processes under excitation. Under high-density excitation pulses at times (i.e.  $\tau \gg 1/I_p\sigma_{io}$ ) the populations reach saturation levels, and all the time derivatives will be equal to zero. This gives:

$$n(G^0) + n(G^-) + n(E^0) + n(E^-) = 0 \quad (2.5)$$

$$n(M^-) = n(M^0) \left[ \sigma_{io}(M^0) / \sigma_{io}(M^-) \right] \quad (2.6)$$

$$n(M^0) + n(M^-) = N_{total} \quad (2.7)$$

In the case when  $\sigma_{io}(M^0) \approx \sigma_{io}(M^-) \equiv \sigma_{io}$  the transmission of the excitation beam changes from the initial value  $T_0 = e^{-\sigma_{ab}(G^-)LN_{total}}$  to saturated level  $T_s = e^{-\sigma_{io}LN_{total}}$ .

This model is also in good agreement with results reported in ref [53]. In this paper, it was reported that the ratio of the photoionization rates for  $NV^- \rightarrow NV^0$  process and for  $NV^0 \rightarrow NV^-$  processes are  $\sim 0.4$  at 540 nm excitation wavelength. If we will use this ratio for photoionization processes and change of transmission at 532 nm from  $T_0 = 3\%$  to  $T = 10\%$  from our experiment, we could find the relation between absorption and photoionization cross-sections as  $\sigma_{io}(M^-) \approx 0.5\sigma_{ab}(G^-)$  at 532 nm. It is noteworthy that this ratio does not depend on other parameters of the model.

In the case when  $\sigma_{io}(M^0) \approx 0$  (i.e.  $\sigma_{io}(M^0) \ll \sigma_{io}(M^-)$ ), the population  $n(M^-) = 0$ , and all the centers will be localized at  $n(M^0) \approx N_{\text{total}}$ , where the absorption at pump wavelength is neglectable  $\sigma_{io}(M^0) \approx 0$ . In this case, the transmission of the excitation pulse will increase from the initial value  $T_0$  to 1 for high pump intensity. This case was observed under 632 nm excitation. It is also in agreement with the data reported in [53] where the photoionization rate for  $NV^- \rightarrow NV^0$  process was significantly bigger than that for  $NV^0 \rightarrow NV^-$ .

This model also describes the recovery dynamic of  $\Delta k/k_0$  at 632 nm. As we have discussed above, after excitation the ratio of the concentrations at metastable levels  $n(M^0)/n(M^-)$  is  $\sim 0.4$  using equation  $n(M^-) = n(M^0) \left[ \sigma_{io}(M^0) / \sigma_{io}(M^-) \right]$  and data reported in ref [53]. The recovery of the absorption to the initial level will consist of decays of the metastable states of  $NV^0$  and  $NV^-$  centers. The decay of time of the  $n(M^-)$  was measured to be  $\tau(M^-) = 250$  ns at room temperature [67], while recovery time for  $NV^- \rightarrow NV^0$  process is significantly slower ( $>10$   $\mu$ s) [45]. In this case,  $\Delta k/k_0$  should be multi-exponential with a “fast” decay rate of 250 ns and amplitude ratio between “slow” and “fast” kinetics  $n(M^0)/n(M^-) \approx 0.4$ . As one can estimate from Figure 2.14, the amplitude ratio for the fast and slow kinetics at 632 nm is approximately 0.4. This indicates strong PI of  $NV^-$  and rising population to the metastable state of  $NV^0$  centers.

The absence of “fast” kinetics for the pump-probe experiments at 670 nm results probably from the strong influence on absorption from other color centers. As one can see from Figure 2.3(A), there is an overlap between  $NV^-$  color centers absorption band with

another band with a maximum of ~700 nm. The analysis of the induced photo effects at this wavelength requires additional study.

## 2.12 Conclusion of Chapter 2

In conclusion, we have measured absorption and emission spectra of  $\text{NV}^-$  centers in a CVD grown diamond sample at room temperature and calculated the absorption and emission cross-sections to be  $2.8 \times 10^{-17} \text{ cm}^2$  and  $4.3 \times 10^{-17} \text{ cm}^2$  at the maximum of absorption and emission side bands, respectively. The estimated cross-section values are in close agreement with reported values documented in the prior literature [61]. Based on the absorption spectra measured and absorption cross-section, the concentration of  $\text{NV}^-$  centers in the diamond sample was estimated to be ~25 ppm ( $4.53 \times 10^{18} \text{ cm}^{-3}$ ).

We observed some threshold for photoionization and there was an appearance of ZPL of  $\text{NV}^0$  along with a broad PSB under pulsed excitation due to photoionization of  $\text{NV}^-$  to  $\text{NV}^0$ . We also estimated the decay lifetime of the excited state of  $\text{NV}^-$  to be 12.4 ns and that of  $\text{NV}^0$  to be 18.8 ns from PL kinetics at room temperatures. Saturated transmission of 532 nm pump pulse was only ~10% even at energy flux much higher than saturation level and we did not detect any induced long-term bleaching of the centers.

In a pump-probe experiment, the transmission kinetics at 632 nm reveal a “fast” decay process with ~250 ns recovery time and a “slow” decay process with ~12  $\mu\text{s}$  recovery time. On the other hand, only a “slow” (recovery time 24  $\mu\text{s}$ ) decay channel appeared in the kinetics of transmission at 670 nm. This indicates different decay channels involved after photoionization of  $\text{NV}^-$  centers under green excitation. Centers recovery to

the steady-state level between the pulses shows no residual absorption or long-lived bleaching for 10 Hz repetition rate. We did not detect long-lived photo-ionization or bleaching of the centers after irradiating under strong 532 nm pump density. Transmission saturates to ~48% level under 633 nm pump which was stronger than that under 532 nm pumping. Pumping at 633 nm with sufficiently high intensity leads to accumulation of electrons in metastable state of  $NV^0$  center resulting in a higher saturation of transmission.

We set up a resonator using the polished face of the sample and gold-plated concave mirror and measured spectral profile at different pump intensities. We did not measure a notable change in full width at half maximum (FWHM) of emission band. That implies the population of the excited state of  $NV^-$  is still small since we do not see stimulated processes or lasing. However, additional experiments are required to estimate the ratio of excited and ionized color centers. The results presented here are significant, given the current interest in using the center as a single-photon source as well as for quantum computing as they draw attention to the important issue of the photochemical stability of the centers.

## CHAPTER 3

### EXCITATION KINETICS OF GR1 CENTERS

#### 3.1 Background

The neutral vacancy (GR1) in diamond is one of the important but poorly studied defect centers in diamond. These centers are known to be stable over a wide range of concentrations. These centers are very common optical centers. They are easily created by ionizing irradiation [15,69,70] and play a crucial role in processes of diffusion and formation of other color centers in diamond. Another important aspect of these centers is their optical absorption and luminescence properties. Neutral vacancy centers are a promising media with a great potential for a wide range of photonics applications due to their thermal and photochemical stability as well as interesting optical properties [5]. The center is associated with a strong and sharp GR1 line at 1.673 eV and other series of lines (GR2 to GR8) in the absorption spectrum. Various other centers related to vacancies (such as NV, SiV, GeV, and so on) are widely studied for many applications in quantum information and precision sensing. A detailed understanding of the excitation kinetics of these vacancy centers can be directly and indirectly advantageous in such fields [71].

### 3.2 Spectroscopic Properties of GR1 Centers

These centers are strongly luminescent at and above room temperature and are thermally stable at temperatures of several hundred degrees Celsius [37,60]. The center has a tetrahedral ( $T_d$ ) point symmetry [72]. The orbital degeneracy is lifted by dynamic Jahn-Teller interactions [71,73]. The energy level structure of GR1 is shown in Figure 3.1 [72–75]. The ground state is  $^1E$  and another closely placed energy level denoted as  $^1A_1$  is separated by 8 meV from the ground level [8,74]. The transition from the ground level  $^1E$  to the first excited state  $^1T_2$  features a sharp zero phonon line (ZPL) at 1.673 eV (741 nm) with a phonon-assisted absorption band within the red spectral region [3,10,12]. The origin of the weak ZPL at 1.665 eV (744 nm) is attributed to the thermally populated  $^1A_1$  state from the  $^1E$  level [7,9,72,76]. The additional lines, designated by GR2 to GR8, are observed in the absorption spectrum between 411 nm and 430 nm due to transitions to higher excited states [77]. However, no resonant photoluminescence was identified corresponding to the transitions from the GR2-8 excited states to the ground state [15]. The direct (632.8 nm) and indirect excitations (410 nm to 435 nm) via GR1 and GR2-GR8 absorption bands resulted in the same PL corresponding to the GR1 emission [78]. Under GR2-GR8 excitation, the GR1 center relaxes non-radiatively to the first excited state followed by a characteristic GR1 PL [78,79]. The PL lifetime was reported to be 2.5 ns and 1.1 ns at 70 K and 300 K, respectively. The estimated radiative lifetime was 182 ns at 70 K which implies non-radiative transition as a dominant relaxation channel [80]. Previously reported time-resolved spectroscopy under nanosecond excitation of the GR1 center showed nearly

uniform decay constant with no susceptible quenching as featured by other nitrogen and vacancy related centers [70,81].

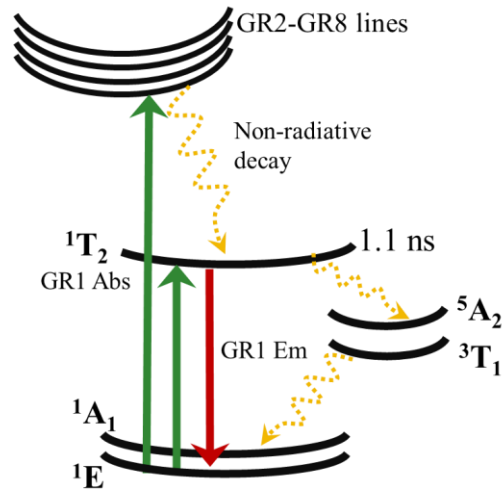


Figure 3.1. The energy level of GR1 centers in diamond as described in the literature. The green arrows show absorption from the ground level and the red arrow shows radiative decay. Various non-radiative decay channels are shown by the yellow dotted arrow lines.

A successful demonstration of Q-switching of Ruby laser cavity using GR1 centers [39] indicates the possibility of GR1 centers utilization for laser applications. However, for applications such as gain media and passive Q-switching of laser cavities, it is very crucial to fully understand the relaxation process after excitation to the  $^1T_2$  level. The present research reports on the optical characterization, nonlinear absorption, and relaxation processes in crystals with different concentrations of GR1 centers. The feasibility of color center diamond crystals as active gain media with frequency tunability in the visible to the near infrared region as well as Q-switching of laser cavities has been analyzed. Due to the energy transfer process, the optical transition of GR1 centers is strongly quenched in the

presence of other impurities. In the present work, we study the dynamics of absorption at possible oscillation wavelengths after excitation.

### 3.3 Sample Preparation and Experimental Setup

The samples used in this experiment were micro-plasma enhanced chemical vapor deposition (CVD) grown bulk diamonds from Element 6. Two diamond samples, designated as HD and LD, having different GR1 concentrations were utilized. The dimensions of the samples were  $4 \times 3 \times 1 \text{ mm}^3$ . The HD sample has all facets polished while LD has only  $4 \text{ mm} \times 3 \text{ mm}$  facet polished. Both diamond crystals had initial nitrogen concentration  $[N] \sim 0.15 \text{ ppm}$  and were essentially free from other impurities (type IIa). The samples were further irradiated using a 4.5 MeV electron source with a beam current of 20 mA and an estimated density of  $2.5 \times 10^{14} \text{ cm}^{-2}\text{s}^{-1}$ . The HD and LD samples were electron irradiated for about 10 hours and 4 hours, respectively. The absence of other donor and acceptor impurities in the crystal ensures the vacancies are predominantly in the neutral charge state ( $V^0$ ). The center imparts bluish-greenish coloration to the crystal.

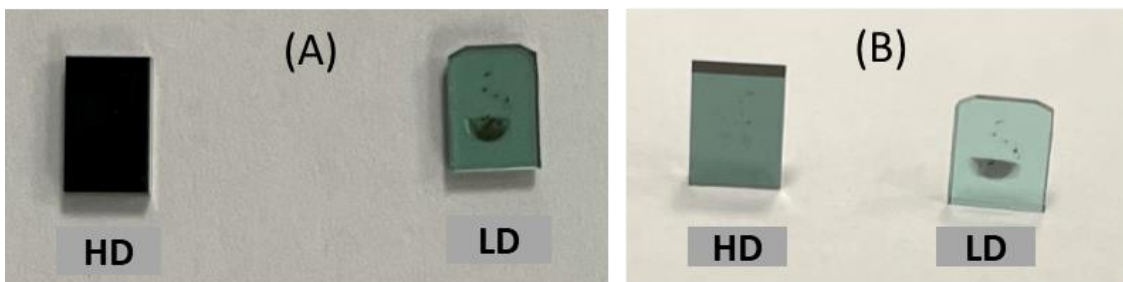


Figure 3.2. Photos of the HD and LD samples (A) from top view when samples were sitting on  $3 \times 3 \text{ mm}^2$  sides and (B) through view when samples were sitting on  $3 \times 1 \text{ mm}^2$  sides. The black spot seen on the LD sample was due to optical damage during intense optical excitation.

The transmission spectra were collected using a Shimadzu UV-Vis-NIR 3101-PC spectrophotometer at room temperature. The optical excitation and pump-probe experiments were carried out using 633 nm pump radiation (Deuterium Raman shifted radiation of a Q-switched 532 nm Nd:YAG laser operating at 10 Hz with a pulse duration of 4.5 ns). The PL signal was measured and detected using an Acton Research Corporation 750 spectrometer and R5108 photomultiplier tube from Hamamatsu and amplified using a gated boxcar integrator from Stanford Instruments. In the pump-probe experiments, CW radiation of 532 nm and 658 nm lasers with power  $\sim 15$  mW were used as probe beams.

### 3.4 Visible and NIR Absorption Spectra

Room temperature transmission spectra of two samples corresponding to the  ${}^1E \rightarrow {}^1T_2$  transition are depicted in Figure 3.3(A). The spectra were collected with a 1 nm spectral resolution at a slow scanning speed of 100 nm/min. The spectra show the GR1 characteristic ZPL absorption at 741 nm, along with the vibronic band extending from 500 nm to 780 nm. The CVD growth process was carried out in an atomic hydrogen-rich environment. The absorption lines near 900 nm and 1075 nm are similar to the sharp peaks observed in hydrogen-rich diamonds and this feature is attributed to hydrogen-related centers [5,82]. As one can see from Figure 3.3(A), the GR1 absorption band overlaps with additional parasitic centers with a band peak near 350 nm. Previously, similar features were reported in absorption spectra and ascribed to negative interstitial vacancy (ND1) centers in type I diamonds. The energy transfer process between ND1 and GR1 centers was triggered under thermal and optical excitation [8,83]. The 350 nm UV band studied in [83]

is very similar to what we observed in our absorption spectra. GR1 and ultra-violet bands are considered to be associated with irradiation-induced donor centers [84]. We believe that the absorption band near 350 nm is due to absorption of ND1 centers alone or other impurity centers originated due to irradiation may also present in addition to ND1 centers. To compare the relative strength of UV absorption bands in our samples, we normalized the LD absorption spectrum to the value of HD absorption at 630 nm, where GR1 absorption dominates. Figure 3.3(B) shows the absorption spectrum of the HD sample (red curve) as well as the absorption spectrum of the LD sample multiplied by factor 6.3 (blue dashed curve). We can see the evidence of another additional band with a peak around 480 nm and the relative concentration of this band is slightly different in HD and LD samples.

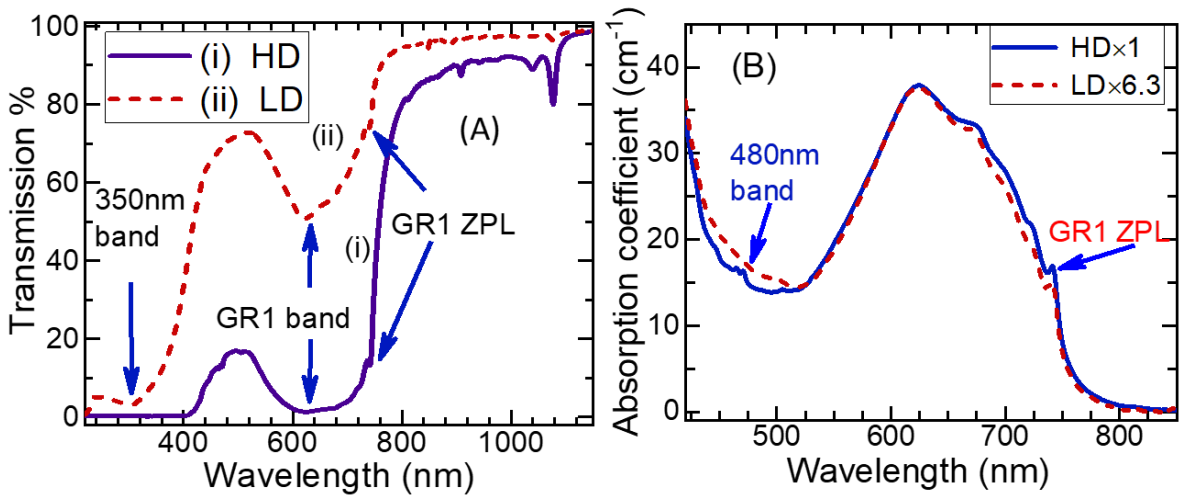


Figure 3.3. (A) Transmission spectra of HD (curve i) and LD (curve ii) samples at room temperature; (B) GR1 absorption spectra of the HD and LD samples normalized near 630 nm. There is an additional band near 480 nm, which may partially overlap with the GR1 absorption band.

### 3.5 Thermal Annealing of the Sample with GR1 centers

As we see the additional band with a band peak near 480 nm, it would be very difficult to separate the absorption band of GR1 centers only because it is not clear where this band tail would extend further in the GR1 absorption region. To study the nature and shape of the 480 nm band and obtain the true and correct absorption band of GR1, we annealed the HD sample in various steps and studied the change in the shape of this band. This experiment was done after the completion of all the experiments that will be discussed in the following sections. The thermal annealing was carried out in four different steps; (a) 1<sup>st</sup> annealing (530°C for 1 hour), (b) 2<sup>nd</sup> Annealing (530°C for 1 hour), (c) 3<sup>rd</sup> annealing (530°C for 2 hours), and (d) 4<sup>th</sup> annealing (650°C for 2 hours) and measured absorption spectra after each step which is shown in Figure 3.4. For all the stages of annealing, the furnace was preheated to the desired temperature and the vacuum-sealed ampoule with the sample was inserted into the furnace. The ampoule was cooled down rapidly by placing it in running tap water after annealing.

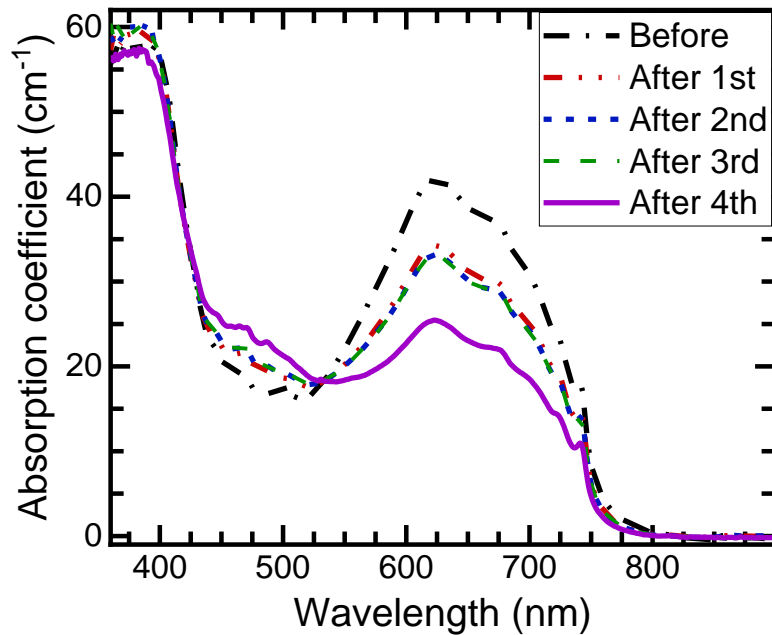


Figure 3.4 Absorption spectra of HD samples through 1 mm side before and after four different annealing steps to show the change in the distribution of color centers concentration.

The 1<sup>st</sup> annealing is accompanied by a decrease in absorption of the GR1 band and an increase in the 480 nm band. However, after 2<sup>nd</sup> and 3<sup>rd</sup> annealing, there were no further changes and the diffusion process reached saturation level (see red, blue, and green curves in Figure 3.4). The 4<sup>th</sup> stage of annealing was performed at a higher temperature (650°C) and carried out for 2 hours. it resulted in a further decrease (increase) of the GR1 (480 nm band) absorption.

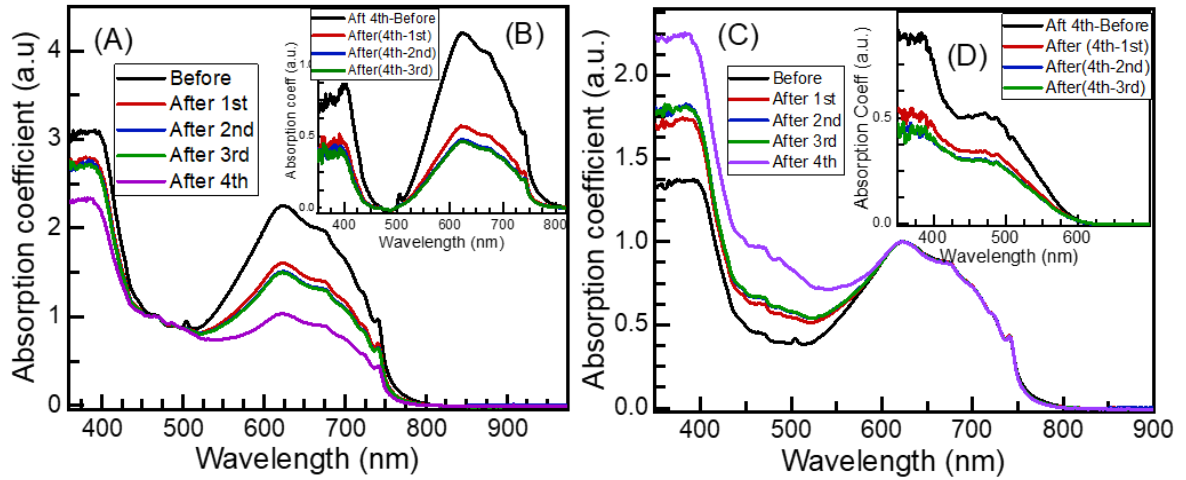


Figure 3.5 Absorption spectra (in arbitrary units) of HD sample before and after four different annealings (A) normalized at the maximum of 470 nm band, (B) their difference from the absorption after 4<sup>th</sup> annealing (to reveal true GR1 absorption band), (C) normalized at a maximum of GR1 absorption, and (D) their difference from the absorption spectra after 4<sup>th</sup> annealing (to reveal true 480 nm band).

We further treated spectra shown in Figure 3.4 to obtain the actual shape of GR1 and 480 nm bands and understand their overlapping. In Figure 3.5 (A), we can see absorption spectra normalized at 480 nm and the difference between each other would result in a true GR1 absorption band (see inset Figure 3.5 (B)). The GR1 absorption band extends from 500 nm to 780 nm. In addition to that, Figure 3.5 (C) shows spectra normalized near the maximum of GR1 absorption and the difference of each curve from that after 4<sup>th</sup> annealing reveals an additional 480 nm band and its shape (see Figure 3.5 (D)). Since the HD sample has a high concentration of vacancies, its annealing results in their aggregation bringing two adjacent vacancies together forming di-vacancy (TH5) centers that have an absorption band around 480 nm [85–88]. A similar effect was observed in [84] where at 600 °C the change produced in the type IIa diamond was a reduction in strength of the GR1 and ultra-violet bands, and the production of the TH5 absorption

system in the region 2.3-2.8 eV. This band extends up to 600 nm and partially overlaps with the absorption of the GR1 vibronic band.

### 3.6 Emission under Pulsed 633 nm Excitation

Excitation with 633 nm radiation resulted in a luminescence band spanning over the 700 nm - 870 nm range with a sharp ZPL at 741 nm as shown in Figure 3.6. The PL signal was strong and easily detectable even with the closed slits of the spectrometer. The emission band shown was calibrated with respect to the sensitivity of the spectrometer-detector combination using an Oriel standard calibration lamp (Model # 63358) and normalized to 1 (details are presented in Appendix on page 136). The pulse duration (~4.2 ns) is longer than the reported lifetime of  $^1T_2$  deactivation (1.1 ns) at room temperature [89]. Hence, the excited state lifetime cannot be directly measured with the current pump pulse.

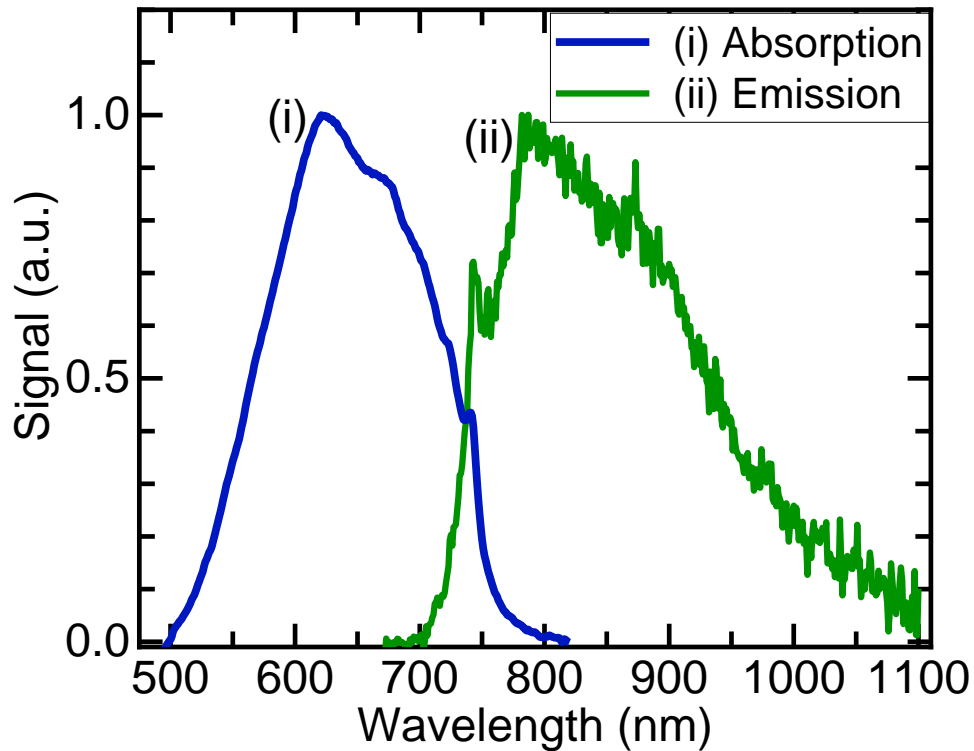


Figure 3.6. The normalized (i) absorption band and (ii) emission band of GR1 centers were measured under pulsed 633 nm excitation and calibrated with respect to the sensitivity of the spectrometer-detector system.

### 3.7 Pump-probe experiment under nanosecond excitation

The dynamics of excited states kinetics could, directly and indirectly, affect the population of the upper laser level and to examine that, in the present section, we utilized a pump-probe experiment. We studied the dynamics of absorption at possible oscillation wavelengths after excitation at room temperature. The performed pump-probe experiment was conducted with the use of two CW probe beams at 658 nm and 532 nm and the measured kinetics were compared for both diamond HD and LD samples. The experimental setup of the pump-probe measurement is shown in Figure 3.7. The red and green arrow

lines show the direction of the pump and probe beams, respectively. The steering mirrors (M1, M2, and M3) are used to direct, and folding mirrors (FM1 and FM2) are used to separate the pump and the probe beams. The pump and the probe beams were sent collinearly through the sample. An additional dichroic filter was used to remove the residual pump after FM2. The probe beam is directed to the fiber cable whose other end is attached at the entrance slit of the monochromator. The grating of the monochromator is adjusted at probe beam wavelength which was measured by the PMT 5108 mounted at the exit slit.

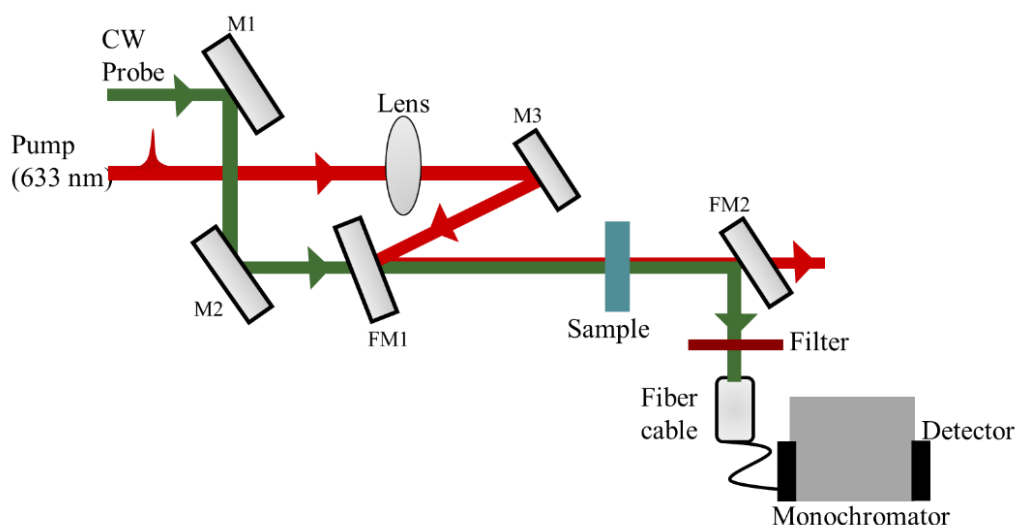


Figure 3.7. Experimental setup of the pump-probe experiment. Green and red arrow paths represent the probe and pump beams directions, which travelled collinearly through the sample. The mirror FM2 and a red dichroic filter separate the probe from the pump. The transmission of the probe is collected by fiber cable and directed to the monochromator - PMT combination.

In this case, the pump-induced change in transmission of the CW probe beam was measured. To investigate and explore the dynamics of the saturation and excited state

absorption at the probe beams, we plotted the normalized kinetics as  $-(k_0 - k(t))/k_0 = -\Delta k/k_0$ , where  $k_0$  is the initial absorption coefficient and  $k(t)$  represents its temporal evolution after pulse excitation at probe wavelength. In the case of a single excitation center without excited state absorption (ESA), this ratio does not depend on the absorption cross-section and should be the same for both probe beams. The ratio  $(\Delta k/k_0)$  is proportional to fractional population inversion  $(\Delta N/N_0)$  and gives the kinetics of population inversion and recovery of the centers to the original energy level. In this notation, a positive value corresponds to the saturation of the sample absorption due to bleaching of the ground level while a negative value indicates the presence of induced excited state absorption and/or photoionization.

The measurements were done for both HD and LD samples and results are depicted in Figure 3.8 (A), (B), and (C) for nanoseconds, microseconds, and milliseconds timescales. The graphs show the temporal profiles of the 658 nm probe beam recorded at different timescales for HD (green curves (i)) and LD (blue curves (ii)) samples. The time duration of the detection is much longer than the excited level lifetime of GR1 centers so the radiative channel involving photoluminescence can be neglected for this time frame. As one can see from Figure 3.8 (A), we see a decrease in absorption due to saturation for both samples. In the case of the LD sample, the saturation spike is seen at the beginning of kinetics followed by a slow relaxation to the initial stage with a lifetime of 220  $\mu\text{s}$ . The amplitude of the initial spikes is approximately the same as the amplitude of slow relaxation. It indicates that the relaxation from the  $^1\text{T}_2$  state occurs predominantly via the metastable state.

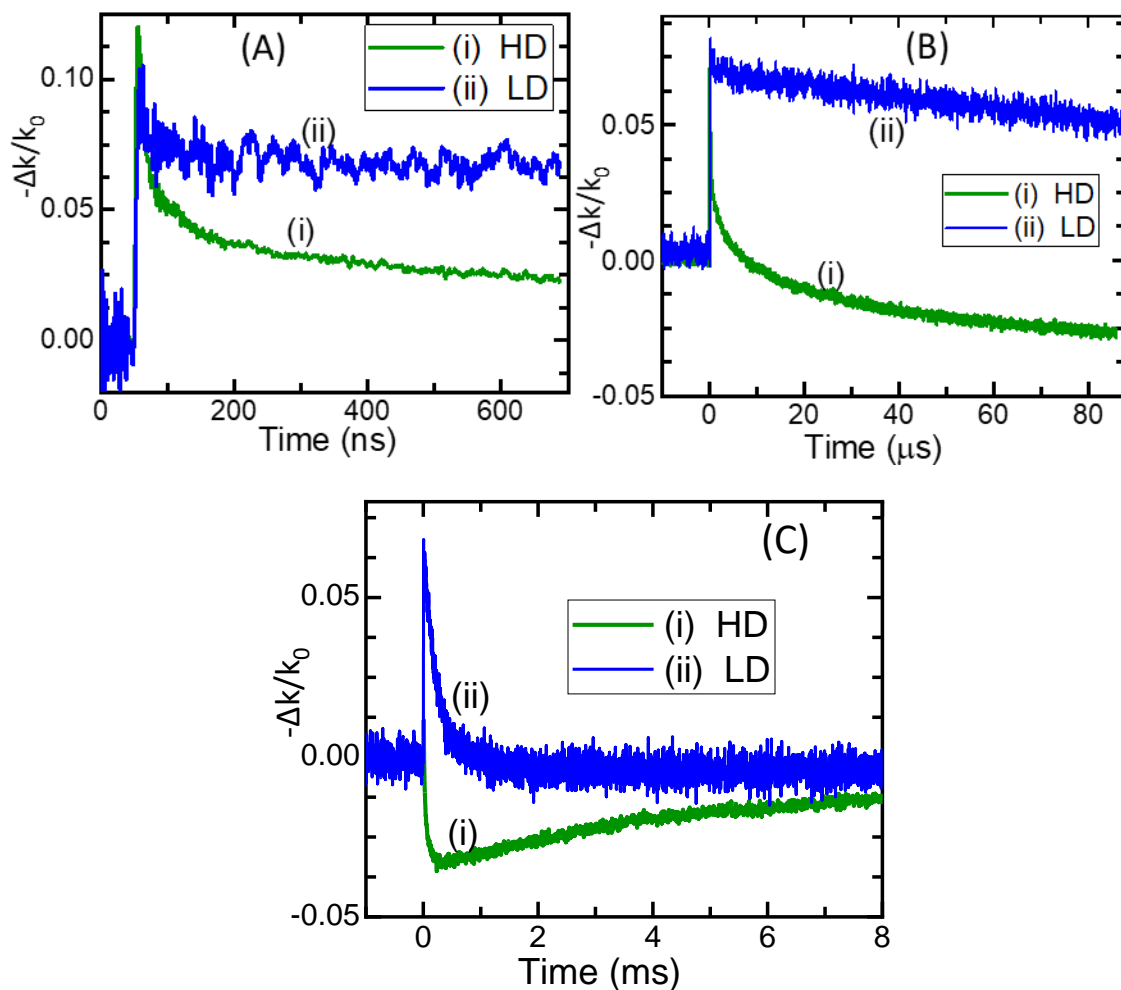


Figure 3.8. The kinetics of 658 nm CW probe beam at (A) nanosecond, (B) microsecond, and (C) millisecond timescales for HD and LD samples are shown in orange (curves (i)) and blue (curves (ii)), respectively.

The kinetics of the HD samples show a more complicated multi-exponential behavior. After initial saturation, we observed an induced absorption with a rise time of 44  $\mu$ s (see Figure 3.8 (A) and (B)) followed by a non-exponential decay with a lifetime close to several milliseconds (see Figure 3.8 (C)). The induced absorption was bigger than the ground state absorption that is why the curve (i) falls below zero. This signifies that the induced

absorption cross-section was larger than the absorption cross-section of GR1 CCs ground level at 658 nm. All the signals recover to the original level before another pulse (within 100 ms). No long-term bleaching or residual absorption at a 10 Hz repetition rate were measured. The rise time of induced absorption differs from the lifetime of the  $^1T_2$  state (1.1 ns) and the lifetime of the metastable state (220  $\mu$ s). Therefore, it could not be due to an energy transfer from the GR1 center to other CCs.

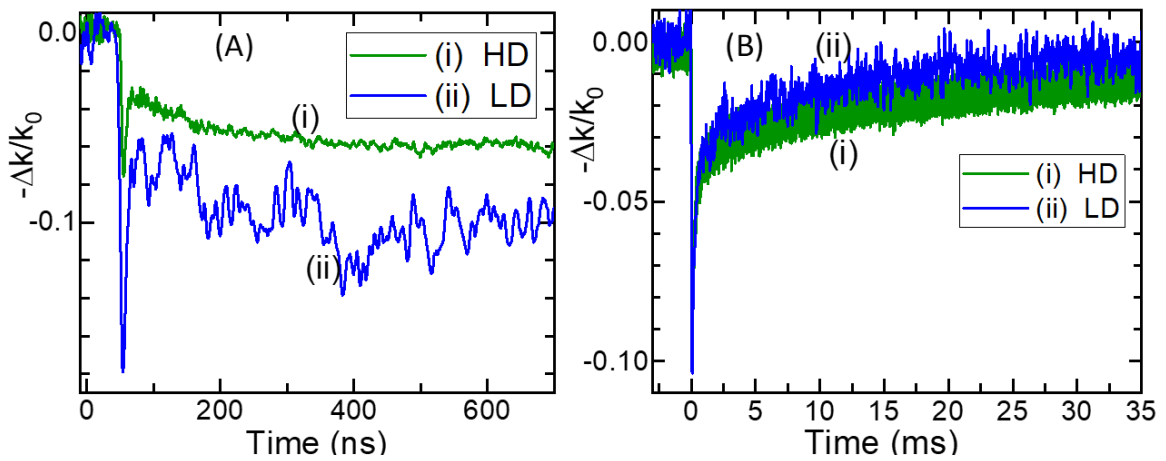


Figure 3.9. The kinetics of 532 nm CW probe beam at (A) nanoseconds and (B) millisecond timescales for HD (curves (i)) and LD (curves (ii)) samples.

Similarly, the kinetics of the 532 nm probe beam in the HD and LD samples were measured in the same fashion, and results are presented in Figure 3.9 (A) and (B), where curves (i) and (ii) are for HD and LD samples, respectively. The kinetics of both samples feature an increase in absorption and slow recovery after tens of milliseconds. In this case, the recovery time is slower than that for the 658 nm probe meaning the channels for slow relaxation are different. A short spike seen at the initial stage of the kinetics of both samples illustrates a strong ESA of GR1 centers with a short lifetime close to the pulse duration of the pump.

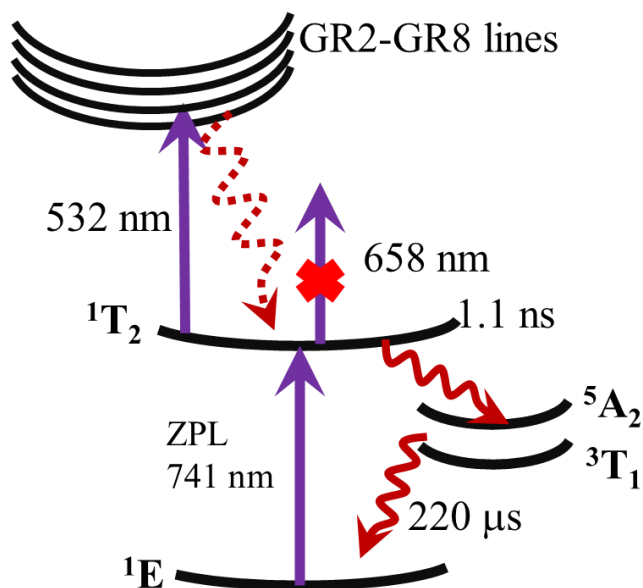


Figure 3.10. Energy level diagram of GR1 centers. The straight arrows show optical absorption, and the curly arrows show the possible relaxation channels involved in the recovery of the GR1 centers based on the model proposed using 658 nm and 532 nm probe kinetics profile of LD and HD samples.

Based on the probe kinetics at different wavelengths of GR1 centers two samples studied, Figure 3.10 represents the observed optical absorption and several possible relaxation channels involved in the recovery of the centers. The positive spikes at the initial stage of  $\Delta k/k_0$  kinetics at 658 nm show that there is a saturation of the absorption at 658 nm (see Figure 3.8(A)), while the negative spikes of several nanoseconds at 532 nm suggest an ESA from  $^1T_2$  level at this wavelength. We observed different kinetics behaviors and recovery times for 658 nm absorption in LD and HD samples. In LD samples, the absorption saturation decays with 220  $\mu s$  lifetime. Considering that the  $^1T_2$  level lifetime was documented to be 1.1 ns at RT [80], we assume that the relaxation of the excitation occurs via a metastable state. No indications of photoionization of GR1 centers at 658 nm

were detected in the LD sample with pump energy fluence up to 500 mJ/cm<sup>2</sup>. In the HD sample, an additional photo-induced absorption with a long non-exponential recovery (>1 ms) was measured.

The long non-exponential recovery time (tens of milliseconds) of the induced absorption at 532 nm wavelength (Figure 4) were measured in HD and LD samples. The most probable model for this absorption is the two-photon ionization of CCs with an absorption peak around 350 nm. The different decay times of the induced absorptions at 532 nm and 658 nm in the HD sample and the absence of induced absorption at 658 nm in the LD sample suggest that these absorptions result from photoionization of different impurity centers. However, the validation of the proposed model for induced absorption bands requires a more detailed study.

### 3.8 Absorption saturation under 633 nm pulsed excitation

The non-linear absorption saturation property of the  $^1E \rightarrow ^1T_2$  transition of the GR1 centers at room temperature was investigated using the setup shown in Figure 3.11 (A). The experiment was carried out under 633 nm pulsed excitation of LD and HD samples. The saturation of absorption of the GR1 centers in natural diamond under Q-switched Ruby laser excitation was previously reported in [39]. The samples used were natural diamonds with very high initial GR1 absorption. Also, it has been mentioned that the presence of N3 centers in the samples could manifest an additional absorption not related to the GR1 centers [39]. In our case, the pump laser was linearly polarized, and radiation attenuation was carried out by rotation of a Glan-Taylor prism and halfwave plate. The samples were

mounted on a translational stage and the incident and transmitted pump powers were measured by sliding the sample in and out of the laser beam path. A knife-edge measurement was done to estimate the beam diameter at the sample surface, measured to be approximately 1.2 mm at FWHM for Gaussian approximation and the crystal thickness was 1 mm. An iris with a width close to that of the pump was inserted to minimize the effect of the luminescence signal.

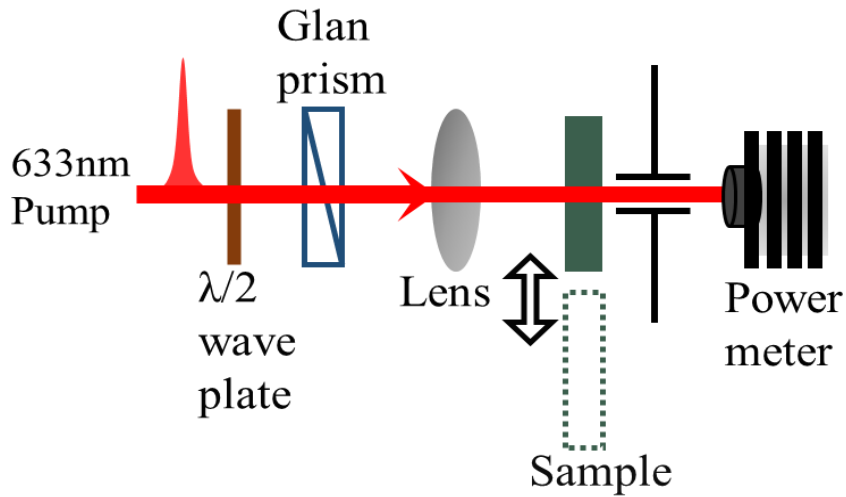


Figure 3.11 Experimental setup for absorption saturation measurement at 633 nm.

The resulting saturation measurement of the GR1 center adjusted for the Fresnel reflection from both facets is illustrated in Figure 3.11 with the big red dots and green circles for LD and HD, respectively. For LD, as the pump energy increases, the transmission increases from its initial value of  $T_0 \approx 55\%$  to the saturated level of  $T_s \approx 84\%$  for a high energy fluence. It illustrates excellent bleaching of the ground level. On the other hand, the HD sample revealed no noticeable saturation before the damage threshold was reached. We focused the beam to  $\sim 1$  mm diameter to get a high energy fluence of  $\sim 1$  J/cm<sup>2</sup>.

The transmission changed from an initial 2% to only 8%. It could be explained by a strong influence of the photoionization process identified in HD samples in the pump-probe experiment.

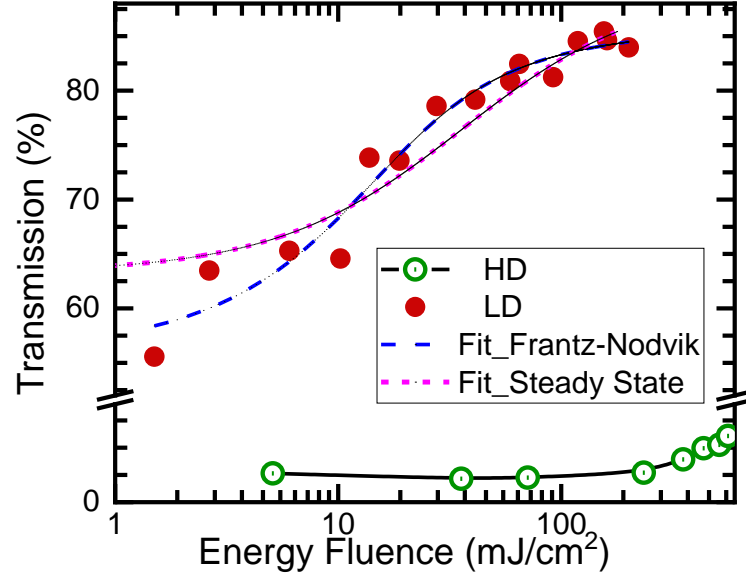


Figure 3.12 Measured transmission of the pump signal through the samples at different input energy fluence (shown by the orange circles for LD and purple circles for HD). The measured data for LD is fitted as a slow saturable absorber.

In order to interpret the absorption saturation measurement data, we used basic non-linear coupled equations that govern the excited state population and pump intensity kinetics in the absorbing medium represented by equations (3.1) and (3.2) below [90,91].

$$\frac{\partial N_2(z,t)}{\partial t} = (N_0 - N_2(z,t))\sigma_{ab}I_p(z,t) - N_2(z,t)\sigma_{em}I_p(z,t) - \frac{N_2(z,t)}{\tau_2} \quad (3.1)$$

$$\frac{\partial I_p(z,t)}{\partial z} = -[(N_0 - N_2(z,t))\sigma_{ab} + N_2(z,t)\sigma_{em}]I_p(z,t) - \alpha_{ns}I_p(z,t), \quad (3.2)$$

where  $N_0$  and  $N_2(z,t)$  are the number densities of total active atoms and those in the excited state, respectively.  $I_p(z,t)$  is the pump intensity,  $z$  is the distance from the absorber front surface,  $\sigma_{ab}$  and  $\sigma_{em}$  are ground state absorption cross-section and excited state emission cross-section, respectively,  $\tau_2$  is the excited state lifetime, and  $\alpha_{ns}$  is the non-saturated absorption coefficient. The coupled differential equations (1) and (2) cannot be solved analytically. However, solutions to these equations were derived for two different regimes of pumping. Frantz and Nodvik solved the above equations for slow-relaxing absorber and obtained solution for the flat top pump profile presented in the equation (3.3) [92], where  $E_{in}$  and  $E_s$  are input energy fluence and saturation energy fluence, correspondingly, and  $T_0$  being the initial transmission. It is valid for slow saturable absorber when pulse duration ( $\tau_p$ ) shorter than lifetime ( $\tau_2$ ) of the excited state (i.e.  $\tau_p \ll \tau_2$ ). The solution for another limiting case when relaxation rate of excited state atom is fast compared to pulse width is given in equation (3.4), where  $T$  is the steady-state transmission for an incident pump intensity  $I_{in}$  and  $I_s$  is the saturation intensity. In other words, is applicable for fast saturable absorber or steady-state case when the pulse duration is much longer than excited state lifetime (i.e.  $\tau_p \gg \tau_2$ ).

$$T = \frac{E_s}{E_{in}} \ln \left[ 1 + \left( e^{\frac{E_{in}}{E_s}} - 1 \right) T_0 \right] \quad (3.3)$$

$$\ln \left( \frac{T_0}{T} \right) + \frac{I_s}{I_{in}} (1 - T) = 0 \quad (3.4)$$

For the GR1 center, the excited state lifetime is shorter than the pump pulse duration, so the regime of pumping is intermediate in our case. However, in the pump-probe kinetics section, it was demonstrated that the relaxation process from the  $^1T_2$  level occurs predominantly via the metastable state with a lifetime much longer than the duration of the excitation pulse. The recovery time is 220  $\mu\text{s}$ , therefore the Frantz-Nodvik equation as a slow-relaxing absorber [92] could still be a good approximation for this experiment. To interpret our results and extract the relevant laser parameters associated with the optical transition, we fit our experimental data for the LD sample, in which saturation level was reached. The fitting was done for both transient case (equation (3.3)) and steady-state case (equation (3.4)) and shown in dashed and short-dashed curves, respectively, in Figure 3.12.

The transmission predicted by the Frantz-Nodvik equation, shown as a dashed line in Figure 3.12, nicely fits our experimental data with a saturation fluence  $E_s = 6.8 \text{ mJ/cm}^2$ . The absorption cross-section ( $\sigma_{ab} = h\nu/E_s$ ) at a pump wavelength of 633 nm was calculated to be  $4.5 \times 10^{-17} \text{ cm}^2$  using the obtained value of saturation fluence. Fitting with the fast relaxation model is shown in a short-dashed line in Figure 3.12 and gives saturation intensity of  $I_s = 6.4 \text{ MW/cm}^2$ . The intensity of saturation  $6.4 \text{ MW/cm}^2$  obtained after fitting the experimental data is two orders of magnitude smaller than the saturation intensity at 694 nm documented in the literature for GR1 centers in natural diamond [39]. Using the relation for saturation intensity  $\sigma_{ab} = h\nu/I_s\tau_2$  and plugging the literature value for excited state lifetime  $\tau_2 = 1.1 \text{ ns}$  at room temperature [89], the absorption cross-section is estimated to be  $4.6 \times 10^{-17} \text{ cm}^2$  at 633 nm. The estimated values of absorption cross-section for two limiting cases are essentially the same. Although a slow relaxation model fits better

with the experimental data, both methods yielded basically the same value for the absorption cross-section at the pump wavelength.

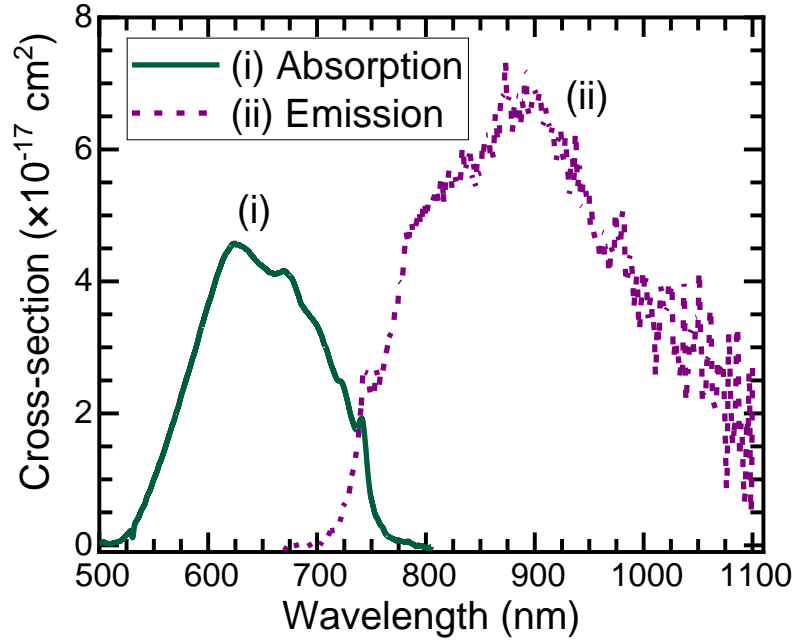


Figure 3.13. Room temperature (i) absorption cross-section and (ii) emission cross-section, where the emission cross-section was calculated using the reciprocity method and Füchtbauer–Ladenburg equation.

Using the absorption spectra and absorption cross-section at pump wavelength (633 nm), we calculated the absorption cross-section spectrum of the  ${}^1E \rightarrow {}^1T_2$  transition of the GR1 center which is shown as curve (i) in Figure 3.13. The cross-section curve was further utilized to calculate other spectroscopic parameters associated with the  ${}^1E \leftrightarrow {}^1T_2$  transition relevant to laser applications. We used an equation (3.5) to calculate the radiative lifetime of the excited level [93].

$$\frac{1}{\tau_{rad}} = \frac{g_l}{g_u} \frac{8\pi n^2}{c^2} \int \nu^2 \sigma_{ab}(\nu) d\nu \quad (3.5)$$

where  $g_l = 2$  and  $g_u = 3$  are orbital degeneracies of the ground and excited states [73], respectively,  $c$  is the speed of light and  $n$  is the refractive index of the diamond. The radiative lifetime was calculated to be  $\tau_{rad} = 7.8$  ns. The Fuchtbauer–Ladenburg relation (equation (3.6)) was used to calculate the emission cross-section for transition  ${}^1T_2 \rightarrow {}^1E$  and is depicted in Figure 3.13 (curve ii). The emission cross section near the maximum of the emission band (around 780 nm) is estimated to be  $\sigma_{em} \approx 7.6 \times 10^{-17} \text{ cm}^2$  [65,94]:

$$\sigma_{em}(\lambda) = \frac{\lambda^5}{8\pi cn^2 \tau_{rad}} \frac{I(\lambda)}{\int \lambda I(\lambda) d\lambda} \quad (3.6)$$

We have also estimated the quantum yield  $\phi = \tau_2/\tau_{rad}$  of GR1 centers as 14% at room temperature, where the lifetime of excited level ( $\tau_2$ ) is 1.1 ns at room temperature [79]. Previously reported values for a radiative lifetime and quantum yield ( $\phi = \tau_2/\tau_{rad}$ ; photons out per photons in) for GR1 centers in natural diamonds were 182 ns and 1.5%, respectively, at 77 K [89]. The radiative lifetime reported in [89] was estimated from the temperature dependent lifetime using the single-vibrational-coordinate model. It was very sensitive to the experimental error and the fitting parameters of the considered model introduced additional uncertainty. Therefore, we believe that the reported lifetime in [89] is overestimated by considering several internal conversion processes between states of the same spin in the equation. The radiative lifetime of GR1 centers estimated in our work is closer to the typical radiative lifetimes of other luminescent CCs in diamond, such as, for N3, H3,  $NV^-$ , and H4 centers 41 ns, 16 ns, 13 ns, 19 ns, respectively [95]. The authors in [95] used a very similar approach with Lorentz correction for the effective electric field to

calculate the radiative lifetimes. As one can easily estimate from Figure 3.13, the FWHM of the absorption and emission bands were measured to be  $\Delta\nu_{\text{abs}} \approx 3600 \text{ cm}^{-1}$  and  $\Delta\nu_{\text{em}} \approx 3700 \text{ cm}^{-1}$ , respectively. The concentration of the GR1 centers was estimated to be  $0.7 \times 10^{17} \text{ cm}^{-3}$  and  $5.5 \times 10^{17} \text{ cm}^{-3}$ , respectively, for the LD and HD samples.

Table 3-1. Various spectroscopic parameters for GR1 center estimated from the experiments.

<b>Spectroscopic Parameters</b>	<b>Symbol</b>	<b>Unit</b>	<b>Measured</b>	<b>Literature</b>
<b>Saturation intensity</b>	$I_s$	$\text{MW}/\text{cm}^2$	6.4 (@ 633 nm)	700 (@ 694 nm [39])
<b>Absorption cross-section at</b>	$\sigma_{\text{ab}}$	$\times 10^{-17} \text{ cm}^2$	4.5	NA
<b>Absorption bandwidth at FWHM</b>	$\Delta\nu_{\text{ab}}$	$\text{cm}^{-1}$	3600	
<b>Radiative lifetime</b>	$\tau_r$	ns	7.8	182 [89]
<b>Emission cross-section</b>	$\sigma_{\text{em}}$	$\times 10^{-17} \text{ cm}^2$	7.6	NA
<b>Emission bandwidth at FWHM</b>	$\Delta\nu_{\text{em}}$	$\text{cm}^{-1}$	3700	
<b>Quantum yield @ 300K</b>	$\phi$	%	14	0.5

### 3.9 Non-selective Fabry-Pérot cavity setup

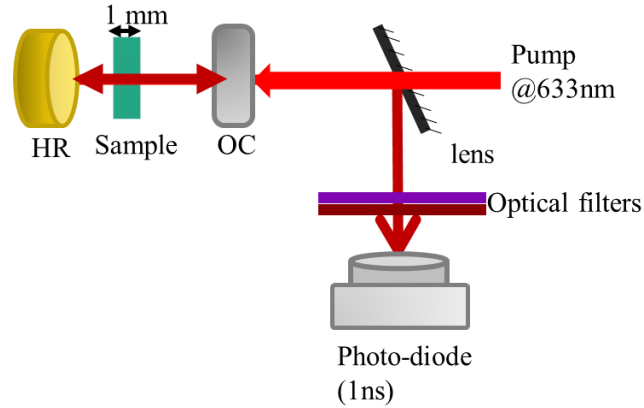


Figure 3.14. Non-selective cavity design to test lasing of GR1 centers under longitudinal 633 nm pumping by pulse pump laser at. The pump is focused by a spherical CaF<sub>2</sub> lens into the sample placed in a cavity formed by a high reflector (HR) and an output coupler (OC).

The HD and LD samples were further tested for possible stimulated emission using several non-selective Fabry-Perot cavities. The design shown in Figure 3.14 is formed by a gold-coated spherical mirror of 5cm radius and output coupler of various reflectivity ranging from 40% to ~99% over 650 nm to 1100 nm spectral range. The pump was focused by a spherical CaF<sub>2</sub> lens of 50 cm focal length in the longitudinal direction along the cavity axis. The pump was incident on the sample at normal incidence and the initial absorption was ~2.5% through a 1 mm long sample at the pump wavelength. The optical excitation was carried out using a 633 nm pump with a pulse duration of 4.3 ns at a 10 Hz repetition rate. The input pump power was adjusted by rotating the halfwave plate while fixing Glan-prism at a fixed polarization direction. The maximum pump density  $> 700 \text{ mJ/cm}^2$  was applied and the cavity output signal was measured by a Si-detector with rising time 1 ns and PMT5108. In addition to the red filter to block the pump, the purple color filter was

used to cut the 1<sup>st</sup> Stokes output of diamond at 690 nm under the 633 nm pump. We also measured the cavity output spectra at different pump intensities and compared FWHM to see any narrowing. We replaced HR and OC and worked with a flat-flat resonator as well, but we did not detect laser oscillations in both samples for this case.

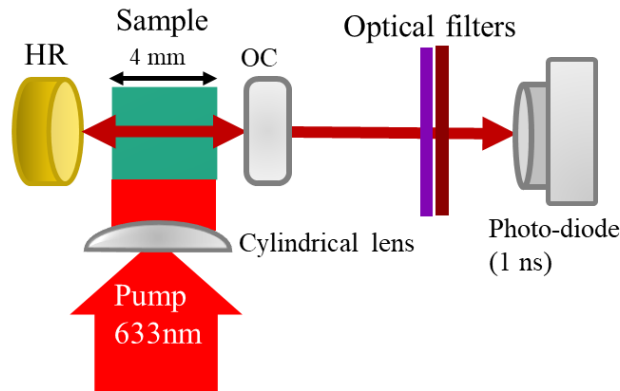


Figure 3.15. Non-selective cavity design to test lasing in GR1 centers for transverse pumping by pulses 633 nm pump laser. The pump is focused in a ~4mm line by cylindrical CaF<sub>2</sub> lens into the sample placed in a cavity formed by a high reflector (HR) and an output coupler (OC).

During the longitudinal pumping scheme, although the 1<sup>st</sup> Stokes of the diamond at 690 nm was cut by using a glass filter, 2<sup>nd</sup> Stokes lies at 760 nm which is near the maximum of GR1 emission band. To minimize this intrinsic issue associated with GR1 emission and 2<sup>nd</sup> Stokes overlap, we worked in transverse semi-confocal and flat-flat cavities depicted in Figure 3.15. The pump radiation was focused in a horizontal line on the 4 mm×3 mm side at normal incidence with the help of a cylindrical lens of 15 cm focal length. The length of the beam spanned the whole 4 mm crystal length and the width of the beam was adjusted up to 500 μm to match the cavity mode size. The temporal and spectral profiles at different

pump energies were measured and compared, however, no stimulated emission was detected.

After the multiple unsuccessful attempts at normal incidence, we positioned samples at Brewster angle  $68^\circ$  in a flat-flat cavity using two HR mirrors with  $R > 99\%$  over 650 nm to 1100 nm wavelength range. We worked on both collinear and quasi-collinear pumping regimes and collected scattered cavity signals from the side using a positive  $\text{CaF}_2$  lens ( $f = 5\text{cm}$ ). We again obtained the negative result no stimulated processes were detected.

After series of unsuccessful attempts to get lasing of GR1 even with the sample showing nice saturation sufficient for population inversion, we tested the performance of stabilized ( $\text{F}_2^{+**}$ ) color centers in LiF and used one of the samples fabricated ~20 years ago. These centers were laser-active and have shown laser oscillation under 532 nm and 633 nm pulse excitations. All the experimental details are presented in the following sections.

There could be several reasons why GR1 centers did not lase in our experiments. The main reason is the parasitic absorption and ionization of additional impurity centers with a wavelength in a shorter wavelength region. This process is even observed in absorption saturation and pump-probe kinetics of HD samples. On the other hand, the LD sample has a relatively small influence of parasitic centers and demonstrated nice saturation at high pump density but overall gain through the 1 mm side was lower than the threshold. The other facets of the LD samples cannot be used due to unpolished surfaces. The fabrication of laser gain media based on GR1 centers in diamonds requires special optimization of the

center concentration and crystal parameters to minimize the induced absorption at lasing wavelengths.

For laser-related applications, the centers need to be stable after irradiation with high intensity for a substantial time period. To detect any long-lived photoionization or bleaching of the centers, we measured the transmission before and immediately after (within less than a minute) illumination of the sample under 632 nm pump excitation. We irradiated the sample at sufficiently high energy fluence ( $>1.7 \text{ J/cm}^2/\text{pulse}$ ), which approaches the optical damage threshold. After irradiation with  $\sim 10^5$  pulses, our measurement showed no change in the transmission profile of both samples.

### 3.10 Laser Experiment with LiF: $F_2^{+**}$ Crystals

#### *3.10.1 Introduction*

$F_2^+$  centers in the ionic lattice (LiF) represent defect centers with an electron trapped by two neighboring anion vacancies as shown in Figure 3.16. LiF color center crystals feature a unique combination of spectroscopic, laser, thermo-optic, modulation, operational, and mechanical properties [96]. Besides that, due to its low hygroscopicity, and high durability, LiF crystals are special among all the alkali-halides.  $F_2^+$  CCs in LiF features a high quantum efficiency of luminescence at room temperature and have large absorption and luminescence cross-sections. However,  $F_2^+$  CCs in undoped LiF are thermally unstable and diffuse out at room temperature with a lifetime (half decay time) of 12 h [97,98].

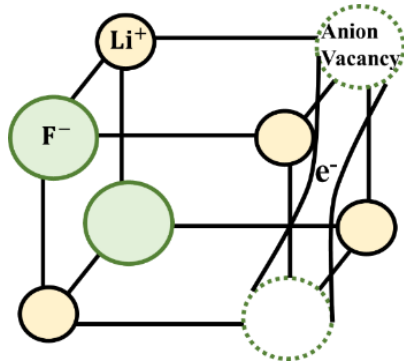


Figure 3.16.  $F_2^+$  center in ionic LiF lattice is a defect center with an electron trapped by two neighboring anion vacancies.

Co-doping of LiF crystals with anion and cation impurities and special procedures of ionizing treatment resulted in LiF with stabilized  $F_2^{+**}$  CCs (LiF: $F_2^{+**}$ ) that are stable at room temperature over periods of months and even years [99]. The  $F_2^{+**}$  CCs constitute pairs of adjacent anion vacancies with one captured electron ( $F_2^+$  center) further perturbed by neighboring anion impurities, cation impurities, and cation vacancies. Efficient room temperature (RT) stable lasing was demonstrated in [99]. Lasers based on LiF crystals containing stabilized  $F_2^{+**}$  color centers (CCs) are tunable over a 0.80-1.22  $\mu\text{m}$  spectral range and are proven to be very efficient and reliable sources of tunable near-infrared radiation [96,97]. Also, a two-stage oscillator amplifier was designed to yield pulse energies suitable for nonlinear optical applications while maintaining the spatial and spectral output characteristics of the tunable LiF: $F_2^{+**}$  CC laser [97].

The spectral position of absorption and emission bands of LiF: $F_2^{+**}$  and GR1 centers in diamond are roughly the same (absorption 500 nm to 800 nm and emission 720 nm to 1050 nm). We decided to test the laser performance of LiF: $F_2^{+**}$  centers using the exact same cavity setups that were used to test GR1 center lasing. This will allow us to

determine whether it is a technological and experimental issue or something of characteristic nature of centers itself for not getting GR1 lasing. Another aim of this experiment is to test the stability of the LiF:F<sub>2</sub><sup>+++</sup> color center crystals at room temperature over a long period of time (more than 20 years). For this, we evaluate the change in concentrations of color centers in LiF crystals with F<sub>2</sub><sup>+++</sup> and tested the laser capabilities of these samples after being stored at room temperature for more than 20 years from the time of irradiation.

### *3.10.2 Sample preparation and Experimental details*

For this study, LiF crystal was prepared by the Kyropulos method in an argon-filled atmosphere and doped with LiOH, Li<sub>2</sub>O, and MgF<sub>2</sub>. To obtain photo-thermal stability and high concentration of the F<sub>2</sub><sup>+++</sup> centers, the crystals doped with LiOH and MgF<sub>2</sub> were further subjected to a multistage Co<sup>60</sup> Gamma (γ)-irradiation treatment with a dose up to (2-5)×10<sup>7</sup> R. The multistage irradiation and temperature treatment of impurity center lower the concentration of colloids and parasitic aggregate CCs [100,101]. A detailed technological and physical processes that lead to the formation of stable F<sub>2</sub><sup>+++</sup> color centers in LiF crystals are widely understood and are discussed in Dergachev et al (1997) [101].

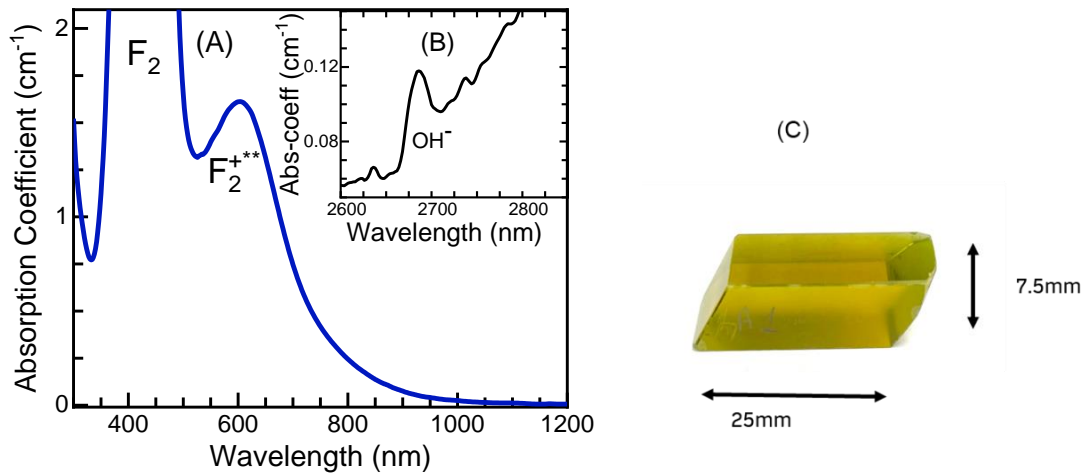


Figure 3.17 Absorption spectrum of the studied LiF sample which was irradiated in 1998 (A) showing absorption band of F<sub>2</sub><sup>+</sup> and F<sub>2</sub> centers, (B) absorption band of hydroxyl group OH<sup>-</sup>, measured in 1998, and (C) A current photo of the sample stored at room temperature for more than 20 years after irradiation.

F<sub>2</sub><sup>+</sup> color centers prepared by the method described in [101] collectively facilitate efficient thermal stabilization of F<sub>2</sub><sup>+</sup> like centers, high concentration of the centers, small optical loss, and reduced efficiency of formation of the other electron donor centers. These centers are proven to be photo and thermostable at room temperature over periods of months and even years, making them suitable for use in laser development. Figure 3.17 (A) and (B) shows the absorption spectrum of the studied sample, which was measured in 1998. Absorption band with maximum ~600 nm is due to F<sub>2</sub><sup>+</sup> centers with bandwidth  $\Delta\nu \approx 3550 \text{ cm}^{-1}$ . Also, a weak absorption band near 2685 nm is due to the hydroxyl group (OH<sup>-</sup>). Figure 3.17 (C) is the photo of the sample used for the current study, which was prepared and irradiated in 1998.

The transmission/absorption spectra were collected using a Shimadzu UV-Vis-NIR 3101-PC spectrophotometer at room temperature at slow speed. The optical pumping was

provided by a 10 Hz repetition rate Q-switched single-frequency Nd:YAG laser emitting pulses of ~4ns duration. The second harmonic of the Nd:YAG laser, at 532 nm, was Raman-shifted in a D2 Raman cell, yielding 633 nm light that was used to pump the CC laser. It is well known that the threshold wavelength for F<sub>2</sub> centers two-step photoionization in LiF is about 590 nm [97]. Thus, the 633nm pump wavelength is well within the suitable range for F<sub>2</sub><sup>+++</sup> centers where parasitic absorption and two-step photoionization of F<sub>2</sub> center is very small. The PL signal was detected using spectrometer SP750 from Acton Research Corporation, R5108 photomultiplier tube from Hamamatsu, and amplified using a gated boxcar integrator SR255 from Stanford Instruments. The measured luminescence spectra of the sample were calibrated with respect to the sensitivity of the detection platform using a standard quartz halogen lamp from Oriel Model # 63358.

### *3.10.3 Absorption of F<sub>2</sub><sup>+++</sup> centers in LiF*

The concentration of the centers increased exponentially over nine months period due to the thermal diffusion process as discussed in [97]. Figure 3.18 (A) shows the room temperature transmission and (B) absorption spectra of the studied single LiF crystal (doped and Gamma irradiated) measured in July 2003 and recently (April 2021) after storage at room temperature for roughly 18 years. The spectra were collected with 1 nm spectral resolution at a slow-scanning speed of 100 nm/min. The F<sub>2</sub><sup>+++</sup> and F<sub>2</sub> centers have partially overlapped absorption bands with peaks around 630 nm and 450 nm respectively. There is a significant change in the spectral profile and a decrease in the concentration of F<sub>2</sub> and F<sub>2</sub><sup>+++</sup> centers over time. Using the absorption cross-section of F<sub>2</sub><sup>+++</sup> at the maximum

(630 nm)  $0.75 \times 10^{-16} \text{ cm}^2$ , the approximate concentration first increases from  $2.1 \times 10^{16} \text{ cm}^{-3}$  in 2001 to  $2.4 \times 10^{16} \text{ cm}^{-3}$  in 2003 and reduced to  $1 \times 10^{16} \text{ cm}^{-3}$  in 2021.

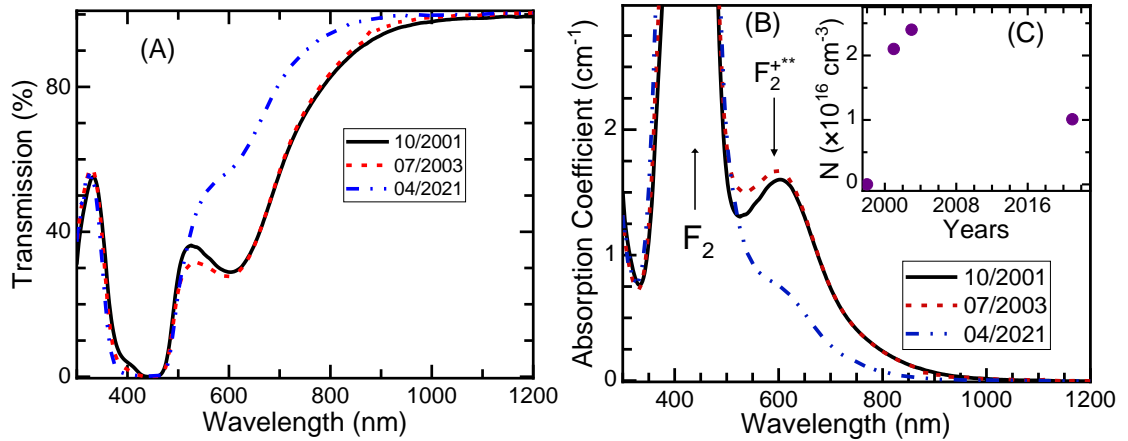


Figure 3.18. (A) Transmission and (B) absorption spectra of LiF crystal (doped and Gamma irradiated in 1998), and (C) change in concentration of  $F_2^{+**}$  CCs over the span of two decades.

The red curve in Figure 3.19 is the transmission spectra measured through the 7.5 mm path length of the sample. The simulated/calculated transmission through 25 mm path length is shown in the blue curve in Figure 3.19. The calculated optical density (OD) is  $\sim 1.5$  at pump wavelength through 25 mm length.

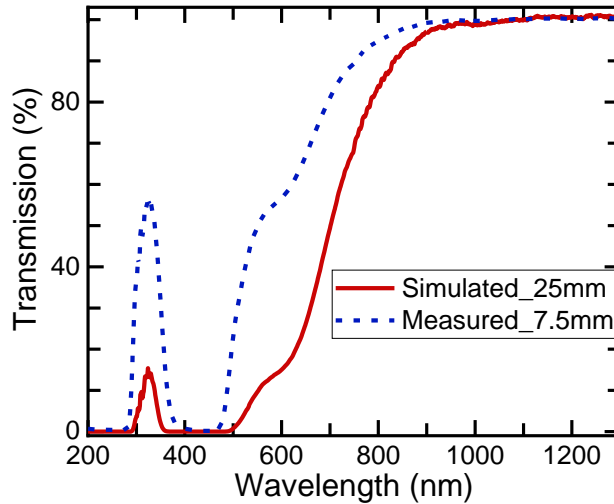


Figure 3.19. Transmission spectra of LiF sample (doped and Gamma irradiated) measured through 7.5mm side (blue curve) and simulated through 25mm side (red curve).

#### 3.10.4 Laser characterization of $F_2^{+**}$ CCs in LiF

The experimental setup to test the laser oscillation of the LiF sample after more than 20 years of irradiation is shown in Figure 3.20. Linear flat-flat resonator of 35 mm cavity length was used where the sample with Brewster cut facets (7.5 mm × 6 mm input aperture) and 25 mm length placed midway between two cavity mirrors. The sample has a maximum absorption of  $0.75 \text{ cm}^{-1}$ . The input mirror has transmission  $\sim 93\%$  at 633 nm and a reflection of  $>99\%$  from 680 nm to 1100 nm. Similarly, the back mirror has reflection  $>99\%$  from 620 nm to 1100 nm. The pump beam was focused by a spherical lens ( $f=50 \text{ cm}$ ) and the beam size at the front surface of the crystal was  $\sim 1.8 \text{ mm}$ . Pump power was controlled by using dielectric filters. The spectral profile of the signal was collected through a fiber cable attached to the entrance slit of spectrometer SP750 from Acton Research and measured and amplified by a photomultiplier (PMT) R5108 from Hamamatsu and gated Boxcar Integrator SR255 from Stanford Research. A collecting lens

of 5cm focal length was placed in the transverse direction to collect the signal from the cavity.

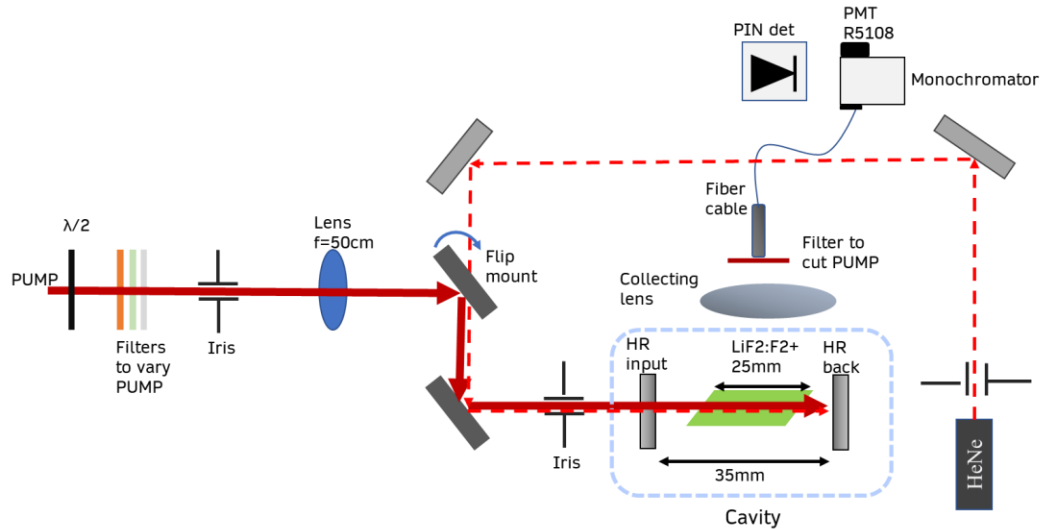


Figure 3.20. Schematic diagram of experiment used to demonstrate lasing in LiF crystal.

The luminescence (dash-dot line) and lasing (solid line) spectra of the non-selective cavity are shown in Figure 3.21(A) for the input of  $145 \text{ mJ/cm}^2$  pump density. The spectra are shown in Figure 3.21(A) were calibrated with respect to the sensitivity of the spectrometer-detector combination using an Oriel standard calibration lamp (model# 63358) and normalized to 1. The threshold for the lasing emission was around  $15 \text{ mJ/cm}^2$ . The back mirror was blocked to measure the luminescence signal without changing the setup alignment and the sensitivity of the detection platform. The PL emission band extends from 700 nm to 1050 nm with a maximum of around 880 nm. The lasing spectra of the output of the nonselective cavity have a maximum of around 920 nm with a bandwidth of 40 -50 nm. Figure 3.21(B) depicts the temporal profile of pump beam (solid line), luminescence (dash-dot line), and lasing (dot line) as measured by a fast Si-PIN

detector with 1ns resolution. The lifetime of the  $\text{LiF:F}_2^{+**}$  centers is measured to be 17 ns and FWHM of the lasing pulse is  $\sim 2.8$  ns.

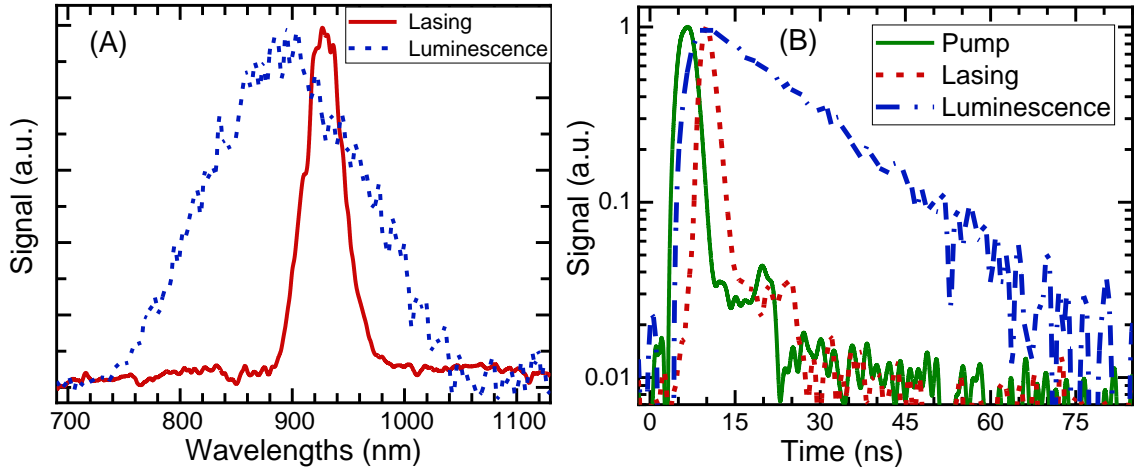


Figure 3.21. (A) Normalized and calibrated spectral profile of photoluminescence (dash-dot) and lasing (solid) and (B) Temporal profiles of the 633nm pump pulse (solid line) and output of the laser cavity (dot line) and photoluminescence (dash-dot) measured with a fast Si photodiode detector.

We investigated the excitation density dependence of the PL spectra of  $\text{LiF:F}_2^{+**}$  in the resonator, which is shown in Figure 3.22 (A). As one can see in Figure 3.22(A) curve ‘i’, the signal showing spontaneous emission spectra at low excitation density (near the threshold), and the progressive appearance of a narrow emission band around 920 nm as the excitation density increases (curves ‘ii’ to ‘iv’). The intensity of the lasing signal at different input pump energy densities is depicted in Figure 3.22(B). It increases almost linearly with the input pump density.

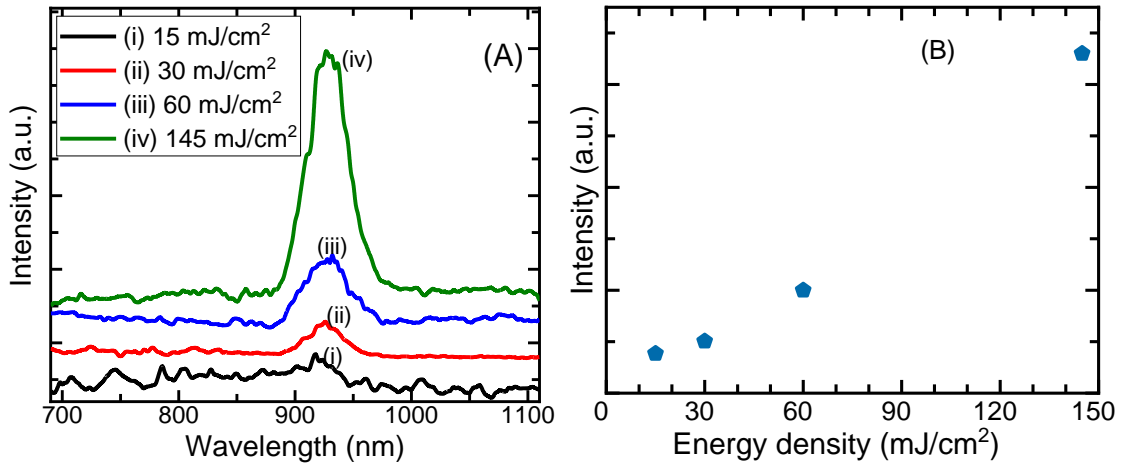


Figure 3.22. (A) Pump density-dependent spectral profile of lasing signal of LiF:  $F_2^{+**}$  from the cavity at room temperature. Spectra were collected by varying the pump excitation intensity. (B) Dependence of maximum signal near lasing wavelength 920 nm with input pump energy density.

In the current work, we tested the laser capabilities of the LiF:  $F_2^{+**}$  a sample stored at room temperature for more than 20 years after irradiation. After comparing the absorption spectra measured recently with the one measured in 2003,  $F_2^{+**}$  and  $F_2$  centers' absorption decreases significantly due to thermal diffusion and recombination of defect centers. However, the stabilized  $F_2^{+**}$  centers are still capable to lase at the 633 nm pumping. The experiment was conducted on the exact same setup that was used for laser experiments for the GR1 center and no lasing was seen for the latter case. This rules out the experimental discrepancy or inaccuracies and suggests more on issues with the intrinsic nature of centers present in the samples with GR1 centers tested for laser experiments.

### 3.11 Conclusions of CHAPTER 3

In summary, we performed a linear and non-linear optical characterization of GR1 (neutral vacancy) centers in CVD-grown bulk diamonds to explore their laser feasibility. Two samples with very high and moderate concentrations of GR1 centers were studied. A strong saturation of absorption under 4.2 ns pulses at 633 nm wavelength was demonstrated in diamond crystals with a moderate GR1 concentration ( $0.7 \times 10^{17} \text{ cm}^{-3}$ ). The saturation fluence  $E_s$  was estimated to be  $6.8 \text{ mJ/cm}^2$  at 633 nm. Irradiation under  $\sim 10^5$  pulses with a pulse peak power of  $300 \text{ MW/cm}^2$  revealed no long-term bleaching of the center. The spectroscopic characterization was carried out and the maximum absorption and emission cross-sections were estimated to be  $4.5 \times 10^{-17} \text{ cm}^2$  and  $7.6 \times 10^{-17} \text{ cm}^2$  at 630 nm and 780 nm, respectively. The radiative lifetime associated with  ${}^1\text{T}_2 \rightarrow {}^1\text{E}$  transition was calculated to be 7.8 ns. After excitation, the relaxation of the  ${}^1\text{T}_2$  excited level occurs predominantly via the metastable state through intersystem crossing with a lifetime of 220  $\mu\text{s}$ . There was no detection of ESA at 658 nm for a crystal with a GR1 concentration of  $0.7 \times 10^{17} \text{ cm}^{-3}$ . This result indicates that GR1 centers could be used as saturable absorbers. The main application of saturable absorber is passive mode-locking (i.e. for mode-locking devices) and for Q-switching of laser cavities (i.e. generation of short optical pulses) for system operating in a pulsed regime over the 550 - 750 nm spectral range (such as Alexandrite laser, Titanium Sapphire, Ruby lasers). However, in the case of CW laser applications, the metastable state of GR1 centers could hamper the lasing process. It is important to note that the induced absorption after excitation with pump radiation was measured at 658 nm and 532 nm wavelengths in the crystal with a GR1 concentration of  $5.5 \times 10^{17} \text{ cm}^{-3}$ . The

slow non-exponential decay of the induced absorption could arise from the recovery after photoionization of the impurity centers. The laser experiments conducted using several cavities and diamond crystals with GR1 centers as gain media resulted in no stimulated emission detected. Later the same cavity setup was used with LiF: F<sub>2</sub><sup>+</sup>\*\* color centers as the gain medium and lasing were successfully realized. That rules out the experimental fault and suggests that the fabrication of laser gain media based on GR1 centers in diamonds requires special optimization of the center concentration and crystal parameters to minimize the induced absorption at lasing wavelengths.

CHAPTER 4  
LASER APPLICATIONS OF DIAMOND

4.1 Introduction

Raman lasers are attractive ways to generate laser radiation at new frequencies and to generate high brightness Stokes beams [102,103]. The stimulated Raman scattering (SRS) in the gain medium is an inelastic scattering process where an incident pump beam passing through a Raman-active medium can generate a new frequency. When an incident pump laser radiation is scattered by the atom, the resulting scattered electromagnetic pump wave is downshifted (Stokes' line) and upshifted (Anti-Stokes line) by some characteristic frequency called Raman shift. The material properties most relevant to high power generation are the low thermal expansion coefficient ( $\alpha T$ ), small thermo-optic coefficient ( $dn/dT$ ), high laser-induced damage threshold. Diamond effectively meets these criteria and serves as a very compelling material platform for Raman laser operating over a wide spectral range. Robust thermo-optic properties, large frequency shift ( $1332\text{ cm}^{-1}$  or 40 THz), large Raman gain, wide transparency range (220 nm to 3  $\mu\text{m}$  and 5-100  $\mu\text{m}$ ), low thermal expansion coefficient ( $0.7 \times 10^{-6}$ ) [104], large thermal conductivity (2000 W/m/K) [105], and low thermo-optic coefficient ( $\frac{dn}{dT} = 7.9 \times 10^{-6}\text{ K}^{-1}$ ) [106] make it material of choice for generating very high power stokes beam with excellent beam quality. Raman conversion in diamond media has been investigated in the CW [13,32,34,36,107], nanosecond [108–110], picosecond [3,28,29] and femtoseconds regimes [31,46].

Reported diamond Raman lasers (DRL) are mostly based on the utilization of diamond crystal effective Raman media in various external cavities and intra-cavity schemes. Its performance in unique regimes of operation like stimulated Raman backscattering (SRB) and distributed feedback (DFB) are not fully studied to our knowledge. During the SRB process, once the backward stimulated Raman begins to grow, its temporal behavior is known to be quite different from that of the forward traveling pulse. This is because backward traveling pulse continuously encounters un-depleted pump pulse and its leading-edge can be amplified to the value in excess of pump intensity and resulting in pulse steepening or shortening. The threshold for the onset of this process is very high and is proven to be very efficient in a gaseous medium, however, it is difficult to arrange in a solid-state system because of thermal load and reaching the optical damage threshold at the sufficiently high pump density. Another method to obtain high efficiency is by creating dynamic gratings in the crystal which can be achieved using the interference of two equal laser beams of single longitudinal mode. In this case, a period of interference fringe can be controlled by adjusting the angle between the interfering beams. Thus, generated gain grating works like a combination of parallelly placed mirrors selectively reflecting only one wavelength, which results in higher amplification and narrow spectral linewidth.

In the present work, our focus is on using an undoped diamond crystal as a Raman gain material to test the feasibility of Raman laser in SRB collection geometry at normal incidence and DFB regime. Backscattering geometry provides means to obtain laser with very high efficiency and may involve effective shortening of the output pulse. Likewise, a relatively long diamond crystal arranged in the DFB regime and pumped with a single

frequency laser radiation would result in a highly efficient Raman laser with a very narrow spectral linewidth. Raman lasers in backscattering geometry in gas cells are very efficient (up to 80%-90% efficiency). However, it is difficult to achieve similar efficiencies in a solid-state Raman system. Many practical applications demand laser radiation with sub-nanosecond pulse durations, which is difficult to realize using Q-switching and mode-locking technologies. We want to utilize unique Raman properties of diamond crystal and single-frequency pump source and obtain high output energy using SRB and DFB operation regimes and simultaneously obtain pulse shortening to sub-nanosecond time scale. Moreover, we are also interested in characterizing the different linear cavity output, efficiencies, and temporal profiles of output pulses.

#### 4.2 Undoped Diamond Samples Description

To study the performance of Raman amplification in diamond, microwave plasma-enhanced CVD-grown single-crystal diamonds were used which were provided to us by Element6. We used three uncoated diamond samples namely (a) D1 (7 mm, parallel facets), (b) D2 (6 mm, wedged in one plane), and (c) D3 (7 mm, wedged in two planes). In fact, D1 and D2 represent the same sample before and after re-polishing it. The D1 sample had surface damage during the first couple of measurements and was sent for polishing off the damaged surface. After re-polishing, the length was reduced to 6 mm and the facets were slightly wedged in one plane, so we decided to denote it by D2 in this case. The input surface for all samples was  $2 \times 2 \text{ mm}^2$ . Single crystal diamond materials grown by element

6 are feature exceptional optical, thermal, and mechanical properties as well as low absorption and birefringence.

### 4.3 Multi-pass Amplification of Raman Stokes

The external plane-plane cavity of CVD-diamond Raman laser pumped by 8.3 ns single frequency 532 nm pump pulses of the 2<sup>nd</sup> harmonics of Nd:YAG Q-switched laser operating at 10 Hz repetition rate is depicted in Figure 4.1. The combination of the half-wave plate ( $\lambda/2$ ) and Glan-Taylor prism was used to change the power and polarization of the pump beam and the pump power was varied by rotating the half-wave plate while keeping Glan prism fixed. The pump beam was focused with the help of a spherical lens of 25 cm focal length and the beam size at the sample was  $\sim 1.2$  mm. The cavity containing a high reflector (HR), diamond sample at normal incidence, and an output coupler (OC) is shown in the dotted box in Figure 4.1. The reflectivities of HR and OC at the pump, 1<sup>st</sup> Stokes, and 2<sup>nd</sup> Stokes are given in Table 4-1. The input mirror is the HR mirror which transmits 70% of the pump and  $\sim 99\%$  of the 1<sup>st</sup> and 2<sup>nd</sup> Stokes. Similarly, the OC transmits 82% of the pump and reflects 64% and 66% of 1<sup>st</sup> and 2<sup>nd</sup> Stokes, respectively. Two cavity mirrors were placed very close to the sample so that the total cavity length was 1 cm. Several filters were inserted to cut out the pump. The output power was measured by a power meter from Ophir (Model 3P-SH powerheads) and the temporal profile was detected by a fast Si-detector with a rise time  $\sim 250$  ps with the help of an oscilloscope with 3GHz resolution.

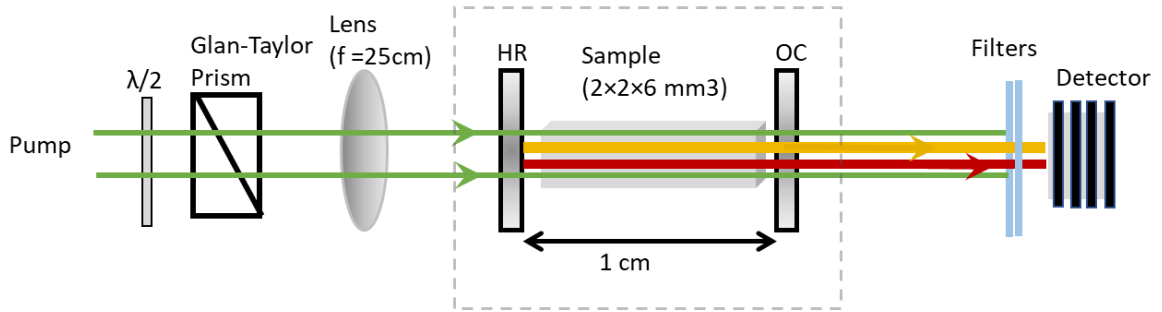


Figure 4.1. Experimental setup used for multi-pass amplification of the first and second Stokes at 573 nm and 620 nm, respectively, under 532 nm pumping.

Table 4-1. Transmission parameter of cavity mirrors used at the pump, first and second Stokes wavelengths.

<b>R%</b>	<b>Pump (532 nm)</b>	<b>1<sup>st</sup> Stokes (573 nm)</b>	<b>2<sup>nd</sup> Stokes (620 nm)</b>
HR	30%	99.9%	99.9%
OC	18%	64%	66%

We first started with the sample D2 (6 mm path length). The spectral output of the cavity is shown in Figure 4.2 (A). It is collected and measured by detector platform, containing SP 750 monochromator (1200 gmm grating) and PMT R928. The spectral positions of 532 nm pump, 573 nm 1<sup>st</sup> Stokes and 620 nm 2<sup>nd</sup> Stokes are clearly seen. Figure 4.2(B) demonstrates output-input characteristics of the cavity where the 1<sup>st</sup> Stokes output is presented (green triangles), the 2<sup>nd</sup> Stokes (orange circles), and the total of the first and second Stokes output (red solid circles). The total slope efficiency of 55% was achieved, while that for the 1<sup>st</sup> and 2<sup>nd</sup> Stokes was 38% and 17%, respectively. The maximum total conversion efficiency is 50% in this case. The total maximum energy reached ~ 6.2 mJ (4.2 mJ 1st Stokes and 2 mJ 2nd Stokes) under 12.3 mJ of pump energy.

Although there are various reports of tens of watts of average output in pulsed and close to kilowatts in CW regimes, the maximum to our knowledge documented single pulse Raman energy is in the order of not more than 3 mJ. In our case, even if the facets of the sample D2 were wedged in the longitudinal direction and the sample was uncoated, we were able to obtain more than 6 mJ of total output. Also, we witnessed an additional loss of the Stokes energy in the transverse direction due to positive feedback of crystal facets parallel in the transverse direction. We strongly believe that significant improvement in terms of efficiency and output pulse energies can be achieved with the use of AR-coated samples with parallel facets in the longitudinal direction with intentional wedging in the transverse direction.

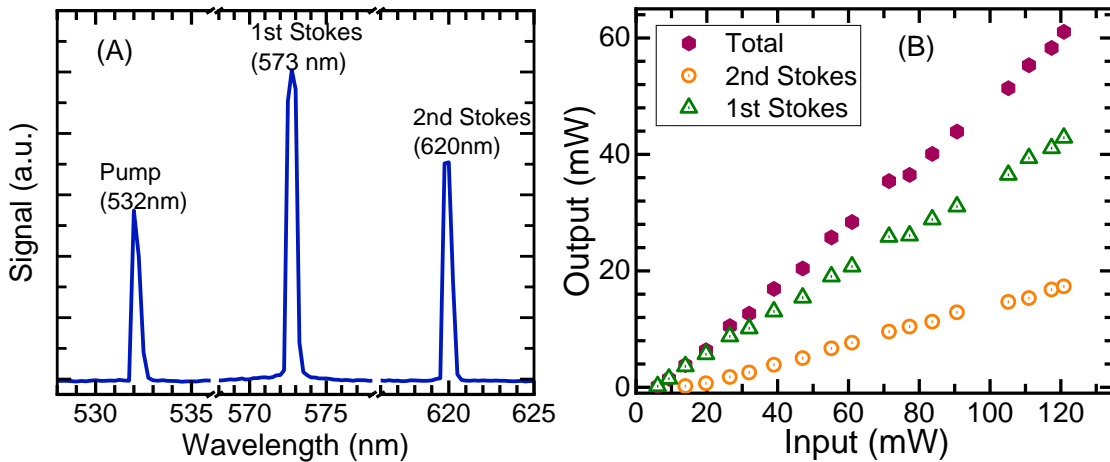


Figure 4.2. (A) The spectral position of pump, 1<sup>st</sup> Stokes, and 2<sup>nd</sup> Stokes. (B) Output-input characteristics for the first Stokes, the second Stokes, and the total output of the cavity for sample D2 (6 mm path length).

Temporal profiles of the pump and the Stokes pulses measured at 1.5 mJ of pump energy, close to the threshold of the 2<sup>nd</sup> Stokes, are presented in Figure 4.3. The pump pulse

duration at FWHM was 8.5 ns. The pulse durations for the 1<sup>st</sup> Stokes near-threshold was 2 ns with 20  $\mu$ J energy for 600  $\mu$ J pump and that of the 2<sup>nd</sup> Stokes was 0.7 ns for 15  $\mu$ J for 1.5 mJ of pumping, while FWHM of 1<sup>st</sup> Stokes was 3.8 ns for this case.

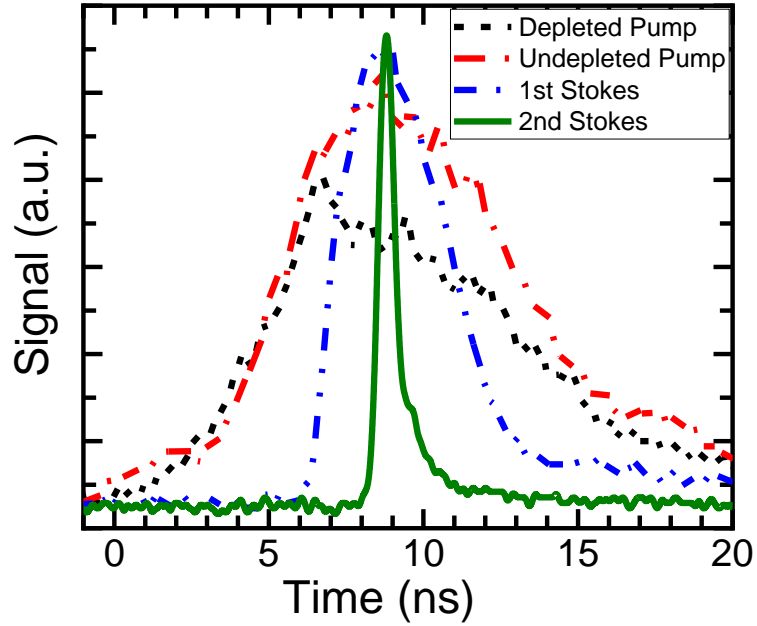


Figure 4.3. Temporal beam profiles of input un-depleted pump (red line), depleted pump (black line), 1<sup>st</sup> Stokes (blue line), and 2<sup>nd</sup> Stokes (green line) were measured near the threshold for the 2<sup>nd</sup> Stokes by 300 ps fast PIN detector.

We further compare the output-input performance of another sample D3 (7 mm, wedged in two planes) with that of the D2 sample (6 mm, wedged in one plane). Because of the wedged longitudinal facets, the output beam contains multiple beam spots as shown in Figure 4.4 (A) and (B). The total output-input characteristics are shown in Figure 4.4(C). The slope efficiencies for D2 and D3 crystals are 55% and 49%, respectively. Although the crystal length is longer for D3, the larger wedge angle between crystal facets resulted in smaller Raman efficiency.

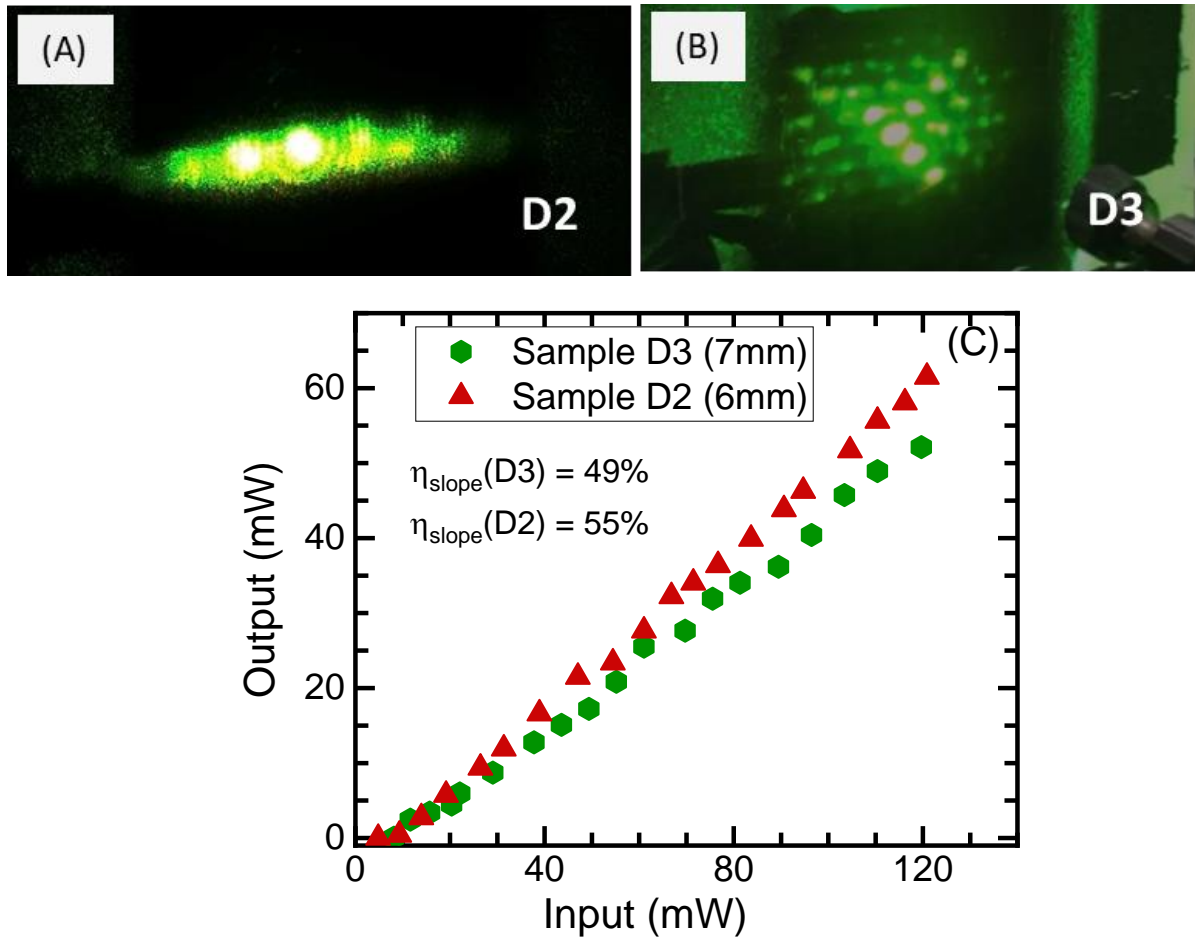


Figure 4.4. Photos of output beams of the 1<sup>st</sup> Stokes from the cavity for samples (A) D2 which is wedged in one plane and (B) D3 (which is wedged in both planes). (C) Total (1<sup>st</sup> and 2<sup>nd</sup> Stokes) output-input performance of D2 and D3 samples.

#### 4.4 Double Pass Amplification for the 1st Stokes

##### 4.4.1 Set-up With a Single Pass Pumping

We arranged another cavity to compare the stimulated Raman scattering of diamond for double-pass for the Stokes using the sample D3 (7 mm, parallel facets). Figure 4.5 depicts the experimental setup used for this purpose, which allows two-pass for the first

Stokes and a single-pass for the pump. The blue filter cuts out any residue of fundamental radiation of Nd:YAG. The experiment, as shown in Figure 4.5, was conducted under longitudinal pumping with the cavity was formed by Fresnel reflection (FR) from the uncoated crystal facet and back mirror (BM) (HR @ 573 nm and HT @ 532 nm). A spherical convex lens of focal length 20 cm focused the pump beam on the  $2 \times 2 \text{ mm}^2$  facet of the crystal. The width of the pump beam at the crystal incident facet was  $\sim 1.1 \text{ mm}$  and increased slightly through the crystal thickness since the focal point was in front of the sample. The folding mirror (FM) (HT @ 532 nm and HR @ 573 nm at  $30^\circ$  incidence) reflected Raman output and an additional high reflecting mirror (at 532 nm) was used to further separate the pump from the Raman laser output. Reflection from the uncoated crystal surface and BM provided necessary feedback for oscillation. The output and input powers were measured with 3A-SH powerheads produced by Ophir. Also, a fast pin detector from Newport with a rise time of 250 ps was used to measure the temporal profile of the DRL output and the data acquisition was carried out by a 3 GHz oscilloscope.

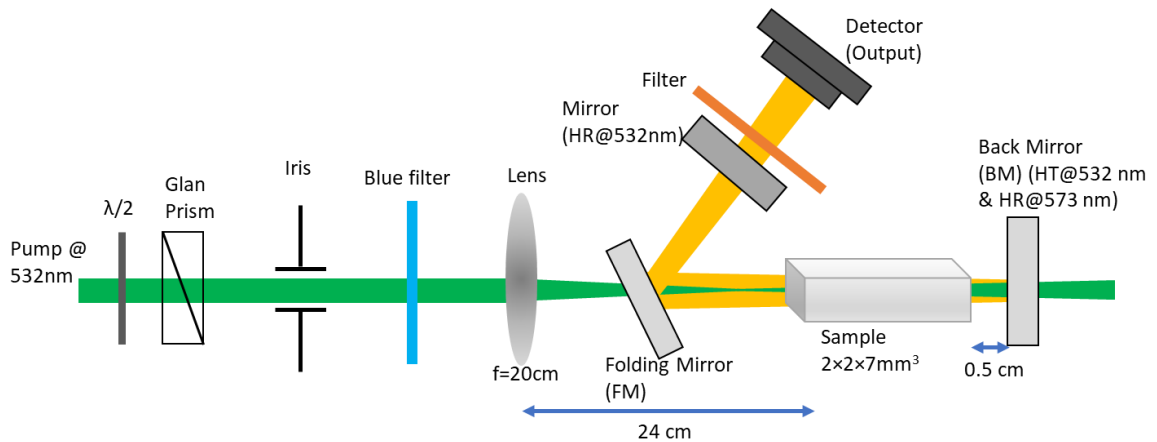


Figure 4.5. Experimental setup used for the two-pass (per round trip) 573 nm first Stokes amplification and a single-pass pumping.

The schematic of the resonator with all the cavity parameters is shown in Figure 4.5. For the given setup, BM reflectivity of the first Stokes is  $R_1 = 99\%$  and FR from input crystal face is  $R_2 = 17\%$ . An additional cavity loss of 17% is due to the reflection from the second facet of the diamond crystal. For threshold estimation, one can use a well-known equation for threshold condition for the round trip  $R_1 R_2 (1 - L) e^{2lg_R l_{th}} = 1$ , where, Raman gain ( $g_R$ ) is  $\sim 50$  cm/GW at 532 nm [111]. Using a 1.1 mm value for the beam size, 8.5 ns pump pulse duration, 10 Hz repetition rate, and the crystal length of 7 mm, the calculated threshold average pump power ( $P_{th}$ ) is  $\sim 31$  mW. Because of the uncoated surface of the crystal, some of the incident pumps would be lost and the actual threshold pump power is  $(31/(1 - 0.17))$  mW  $\approx 37$  mW. Figure 4.6 shows experimental data for the output-input dependence. As one can see, the measured threshold power is 40 mW, which is pretty close to the estimated value (37 mW). The slope efficiency is measured to be 5% and the maximum output was  $\sim 0.3$  mJ for 10 mJ of pumping.

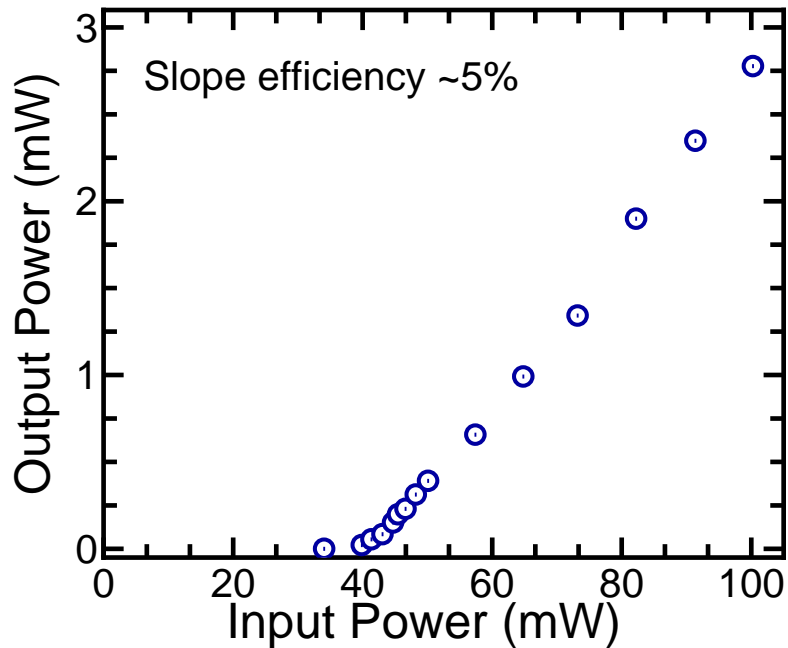


Figure 4.6. Output-input characteristic for double-pass first Stokes and single-pass pumping.

Similarly, Figure 4.7 (A) shows the temporal profile of the input pump pulses (before scattering) measured before the sample (red curve), output pulses of Raman laser operating near threshold under 4 mJ pumping (black curve), and output pulses of Raman laser operating above threshold under 9 mJ pumping (blue curve). As one can see, near the threshold the output pulse is shortened to  $\sim 1.1$  ns pulse duration (PD) at FWHM which is 7.5 times shorter than that of pump PD. In this case, we did not detect second Stokes. Figure 4.7 (b) depicts the dependence of PD of DRL at 573 nm vs input pump power. The minimum PD is 1.1 ns measured near the threshold and it increases almost linearly up to 1.6 ns with the increase of the pump power. Further increase of the pump power above 50 mW resulted in the formation of multiple 1<sup>st</sup> Stokes Raman pulses. We believe that the origin of multi-pulsing is due to cavity mode beating when several resonator modes

oscillate but have different built-up times. In Figure 4.7 (a), one can also see the build-up time starts to decrease as input pump power increases.

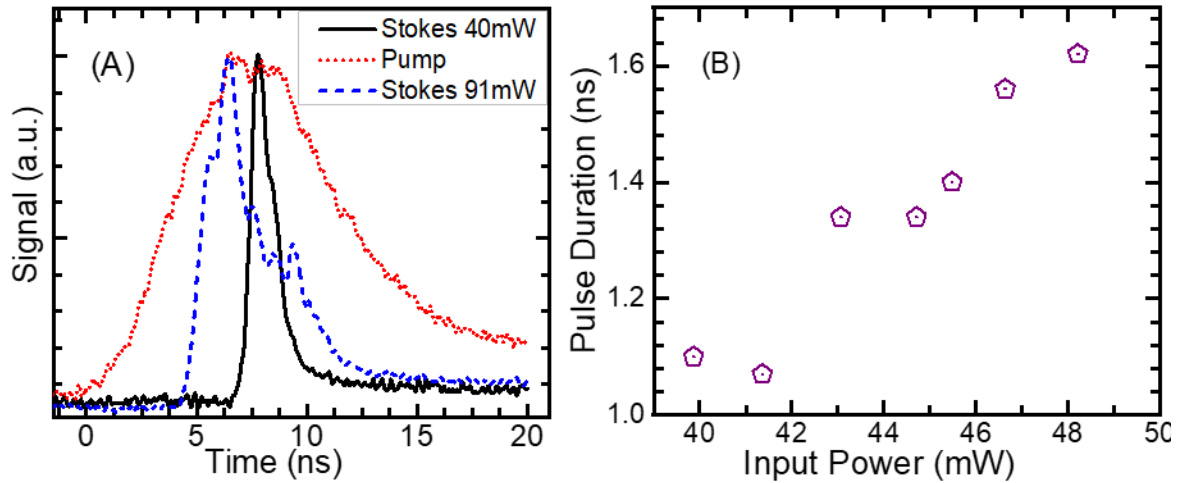


Figure 4.7. (A) Time profile of undistorted pump pulse (red line) first stokes near-threshold (black curve) and much above threshold (blue curve) as measured by 250 ps pin detector. (B) Dependence of pulse duration of single pulse first stokes vs input pump power.

#### 4.4.2 Set-up With a Double Pass Pumping

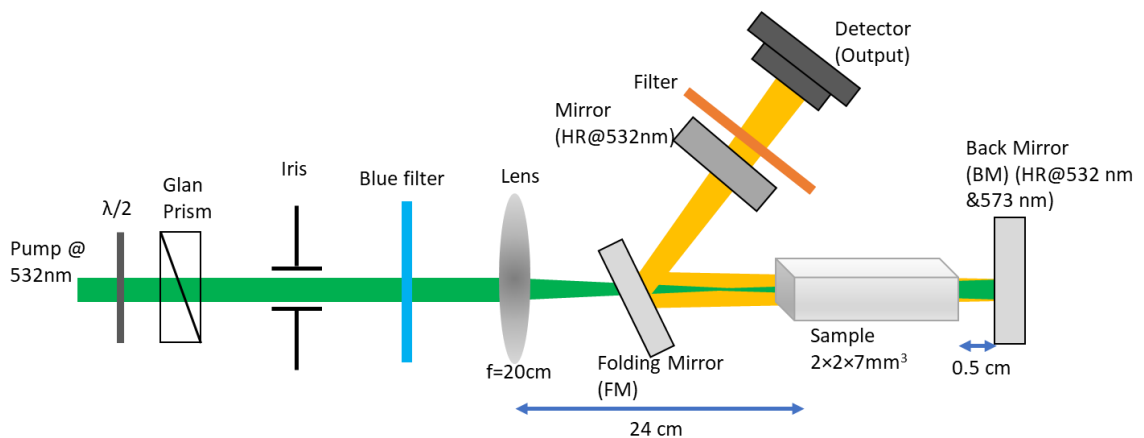


Figure 4.8. Experimental setup used for two-pass amplification for the first Stokes at 573 nm under double-pass 532 nm pumping.

In the next measurement, we replaced BM in Figure 4.5 with another BM, which has HR (~99 %) at both 532 nm and 573 nm to allow a double pass for the pump as well. Everything else was kept the same. The output-input characteristic is shown in Figure 4.9 where the threshold for this case is ~3.4 mJ and a maximum of 0.85 mJ of 1<sup>st</sup> Stokes at 573 nm was obtained for ~12 mJ pump energy. The corresponding slope efficiency is 10%. This time slope efficiency is about 10%, an almost 2-fold increase with respect to the use of single-pass pumping. These results indicate the two-pass amplification of the first Stokes.

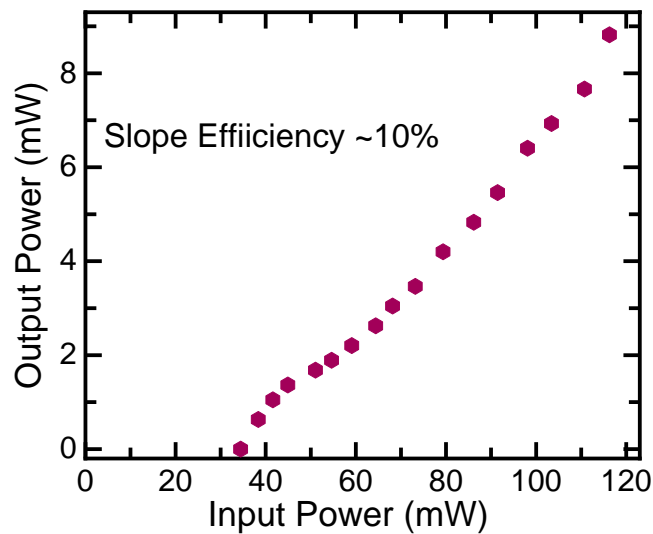


Figure 4.9. Output-input dependence of the DRL based on D3 sample (7 mm, parallel facets) in the cavity that enables double passes both for the pump and the 1<sup>st</sup> Stokes.

Temporal profiles of the input pump pulses (blue), 1<sup>st</sup> Stokes pulses near-threshold (black), and at much higher than threshold pumping (red) for the cavity (double-pass for pump and Stokes) are shown in Figure 4.10 (A). The minimum pulse duration of the 1<sup>st</sup> Stokes (17  $\mu$ J) corresponding to near-threshold (3 mJ) pump energy is ~1 ns. Figure 4.10

(B) shows the dependence of the 1<sup>st</sup> Stokes pulse duration as a function of the pump power. Above 4.4 mJ, pulses start to consist of multiple peaks.

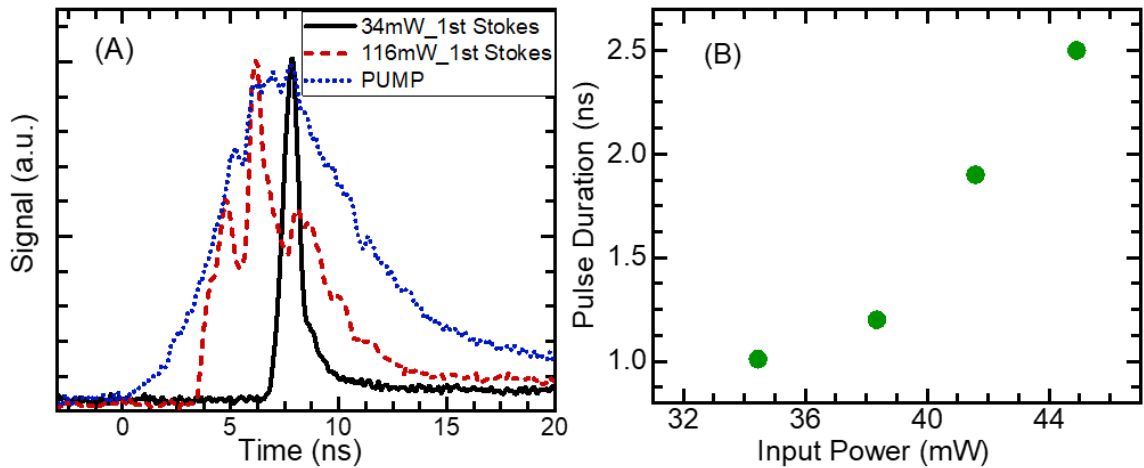


Figure 4.10 (A) Temporal profile of the input pump pulse (blue line), first Stokes near the threshold (34 mW) (black curve) and much above threshold 116 mW (red curve) as measured by 250 ps PIN detector. (B) Dependence of pulse duration of a single pulse of the first Stokes vs input pump power.

## 4.5 Single-pass for 1<sup>st</sup> Stokes

### 4.5.1 Normal Incidence for Backscattering Geometry

Further characterization was conducted for single-pass Raman laser in the backward and forward direction for normal incidence. This setup is designed to test the performance of DRL in backscattering geometry (BSG). The sample D2 (6 mm) was used for this case and the cavity arrangement is shown in Figure 4.11. Two folding mirrors (FMs) separate the pump and the Stokes output. For the detection, a sensitive power meter and 250 ps Newport Si-PIN diode were used. Since the facets of the sample D2 were not

parallel, the amplification of the Stokes from the crystal surface can be ignored. The outputs in the forward and backward direction were collected simultaneously. Wedged facets of the sample mitigate possible amplification due to Fresnel surface reflection.

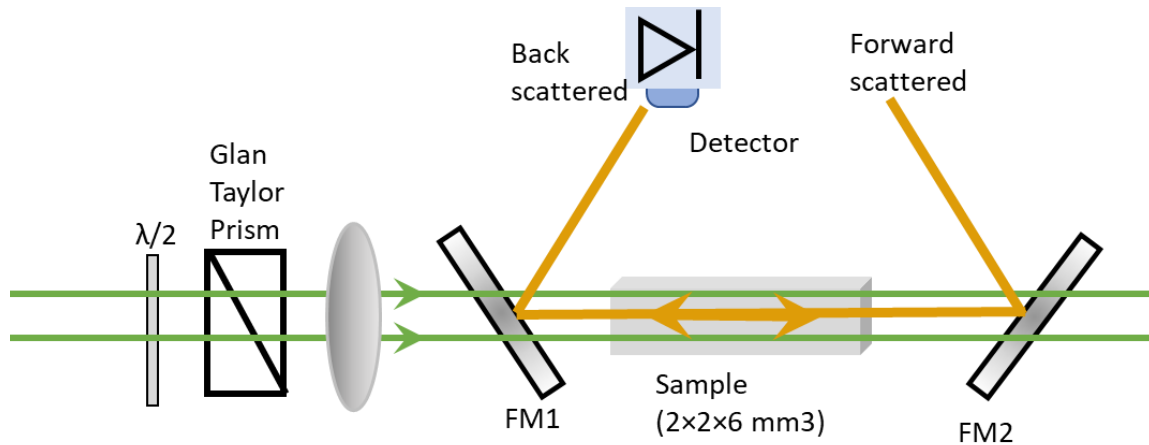


Figure 4.11. Experimental setup used for multi-pass amplification for the first Stokes at 573 nm and single-pass 532 nm pumping.

The output-input characteristics for single-pass Raman at normal incidence are shown in Figure 4.12. The threshold for the Raman generation, in this case, was  $\sim 5.2$  mJ. A slope efficiency of 1.5% was obtained in the backward direction and the total slope efficiency (on both sides) is expected to be  $\sim 1.5 - 3\%$  (without any external feedback mirror). This experiment was performed to test for the evidence of stimulated backscattering Raman (SBR) signal and efficiency is fairly small to what can be expected for SBR. It can be also described by a single pass amplification of the 1<sup>st</sup> Stokes.

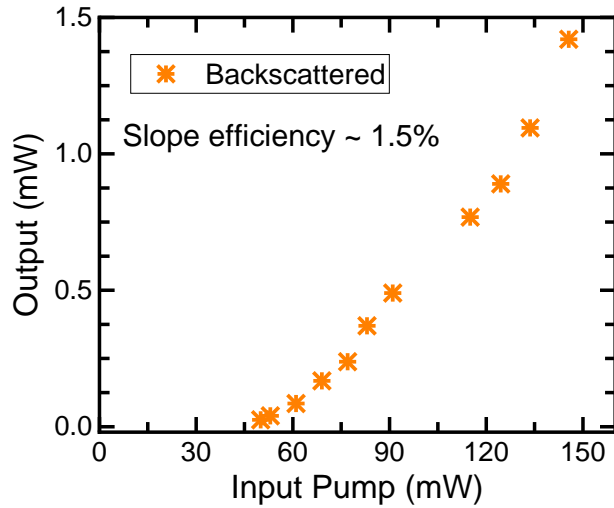


Figure 4.12. Output-input characteristics of DRL for the 1<sup>st</sup> Stokes single-pass amplification for normal incidence.

The temporal profiles of the 1<sup>st</sup> Stokes and pump pulses for backscattering geometry are shown in Figure 4.13 (A). The minimum first Stokes pulse duration of 420 ps in backward and 500 ps in forwarding directions were detected under 5.2 mJ of pump energy. Table 4-2 summarizes the pulse durations and the output energies obtained during this experiment. As one can see, we have achieved more than 20 times pulse shortening in comparison to the pump pulse (8.5 ns). Figure 4.13 (B) shows a single pulse duration dependence vs pump power. . We were able to obtain ~0.15 mJ 1<sup>st</sup> Stokes single pulses ~ 10 folds shortened to ~0.9 ns pulse duration under 9 mJ of pumping. Although the output power is relatively small, it can be used as a seed source for multistage amplification.

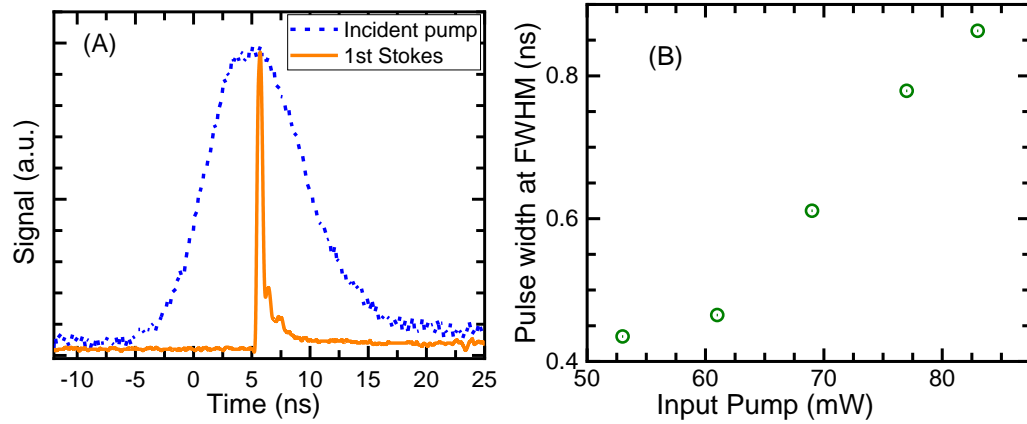


Figure 4.13. (A) Temporal profile of the input pump pulse (blue dash line) and the first Stokes near-threshold (orange curve) as measured by 250 ps pin detector. (B) Dependence of the pulse duration of the single pulse first Stokes on input pump power.

Table 4-2. Pulse durations and energies of the pump, and Raman laser in the forward and backward directions near threshold.

Input Pump		Output (1 <sup>st</sup> Stokes)			
		Backward pulse		Forward pulse	
PD	Energy	Min. PD	Energy	Min. PD	Energy
8.2 ns	5.2 mJ	420 ps	7.5 $\mu$ J	500 ps	9 $\mu$ J

#### 4.5.2 Non-normal Incidence for the Distributed Feedback Geometry

In general, Fabry-Perot lasers utilize two mirrors to obtain positive feedback, which is, in general, a required condition for laser oscillation. However, in distributed feedback lasers (DFB), the optical feedback is obtained by the periodic variation of a corrugated optical plane inside the laser gain medium. One of the methods to achieve this is by creating a dynamic grating within the medium. The periodic variation of index causes a wavelength-

selective reflection and the reflection from each plane of the grating provides positive feedback to the laser oscillation. This is the simplest scheme, which provides high gain and minimizes losses [112].

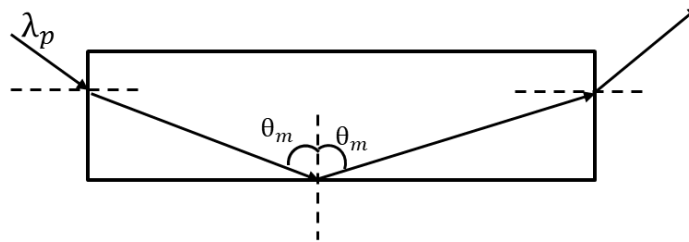


Figure 4.14 Interfering beams intersecting at an angle  $\theta_m$  inside the crystal to create the dynamic grating

The development of the dynamic grating in the crystal can be achieved by using the interference of two coherent laser beams overlapped at some angle as shown in Figure 4.14. The grating period ( $\Lambda$ ) required for a given wavelength ( $\lambda_L$ ) can be given as  $\Lambda = m\lambda_L/2n$ , where “n” is the refractive index and “m” is the order of diffraction. For the first Stokes,  $\lambda_L = 572$  nm the required grating period is 119 nm for the first-order diffraction [100]. The period of created interference fringes depends on the pump wavelength ( $\lambda_p$ ) and the angle of interference ( $\theta_m$ ) as follows  $\Lambda = \lambda_p / 2n \sin \theta_m$ .

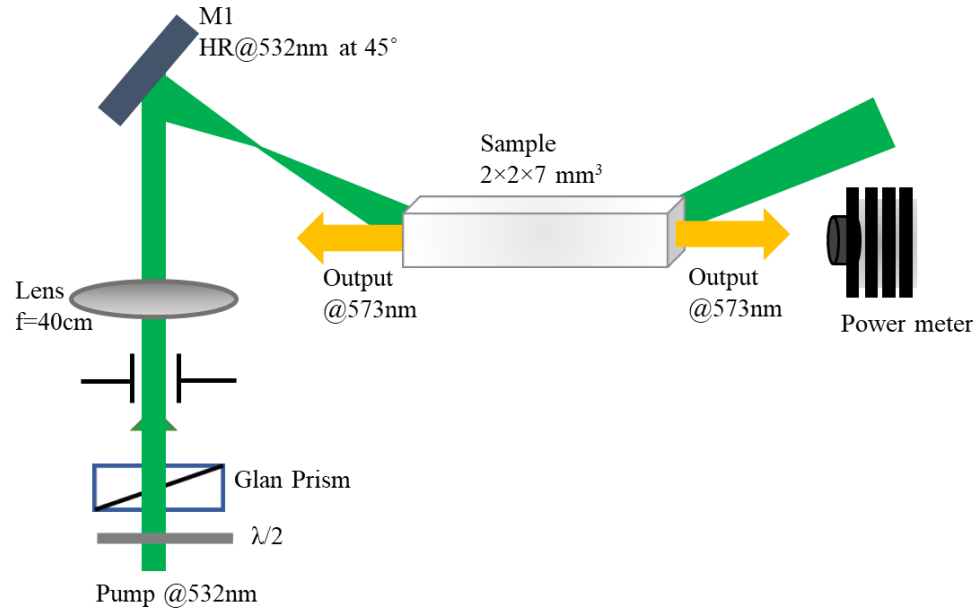


Figure 4.15. The setup was used to obtain a Raman laser at non-normal incidence.

The experimental setup is depicted in Figure 4.15. The pump laser at 532 nm was focused through a convex lens and directed to the sample D1 (7 mm, parallel facets) at an angle of incidence (AOI)  $27^\circ$  with the help of steering mirror M1. The beam diameter was 1.2 mm. No additional mirror was used to provide external feedback. The output power was measured by a 3A-SH powerhead from Ophir. The temporal profiles of pulses were measured with the fast pin detector and oscilloscope with an overall instrumental response time of 300 ps. For the given setup shown in Figure 4.15, the grating period created was 114 nm for the given angle of incidence.

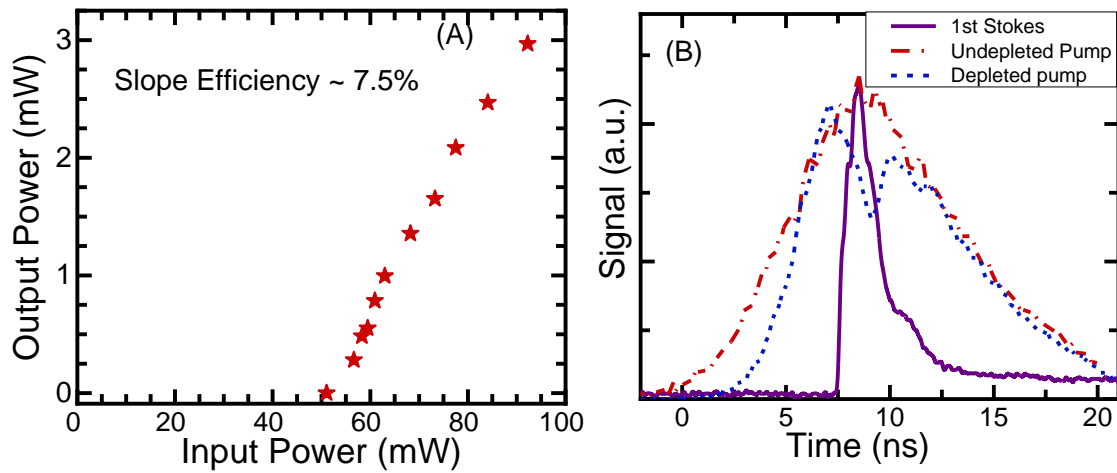


Figure 4.16 (A) Output-input characteristic of the DRL setup used in Figure 15. (b) Temporal profile of un-depleted pump (red dashed-dotted line), depleted pump (blue dotted line), and first Stokes (solid black line).

The 1<sup>st</sup> Stokes Raman laser of visually equal intensities was seen on both sides of the crystal, but the output power as shown in Figure 4.15 was measured from only one side. The slope efficiency was increased to 7.5% for lasing measured in one direction and to 15% if output in two directions is taken into account. The maximum total output energy reached 0.6 mJ for 9.5mJ of pumping. The measured threshold was ~5 mJ, roughly the same as in a normal incidence case.

Temporal profiles of the un-depleted pump (before Raman scattering), depleted pump (after Raman scattering through the sample), and output Raman laser pulses are shown in Figure 4.16 (B). Again, a minimum pulse duration of 1.1 ns was measured near the threshold, and pulse duration increases to ~1.6 ns at ~6.4 mJ pump energy. After that point, pulses started to have multiple peaks.

We further used another sample D3 of identical in size and grown by the same method but with non-parallel facets and ran the same experiment shown in Figure 4.15. Unfortunately, no evidence of Raman laser was detected. We tested at a different angle of incidence including the one required for resonant first-order diffraction grating (AOI =  $64^\circ$ ) and pump very hard ( $>17$  mJ) and no Raman laser oscillation was observed. If the oscillation measured before was due to distributed feedback in the crystal alone, then it should not depend on the orientation of planes of the output facets. Upon comparing the efficiency of single-pass Raman at normal incidence, the total efficiency is much higher (5 times) and 3 times higher than for double pass amplification efficiency. That indicates that some feedback could have been provided due to grating created in addition to the feedback from the surface reflection. For the used  $27^\circ$  angle of incidence, the feedback due to gain grating may be slightly away from the resonant condition but definitely have provided some feedback for amplification. The additional process that might have a positive contribution could be a higher than at normal incidence geometry effective pump volume inside the sample. The above results conclude that dynamic grating may have been created and in combination with feedback from the facets reflection enabled almost 5-fold higher slope efficiency.

#### 4.6 Conclusion of Chapter 4

In summary, we studied the Raman output performance and output pulses temporal profiles at various cavity settings. The possibility to capitalize on the excellent properties of diamond and obtain effective amplification in backscattering and distributed feedback

geometries have been evaluated. For the plane-plane cavity containing a high reflector and ~65% output coupler at the 1<sup>st</sup> and 2<sup>nd</sup> Stokes wavelengths, we obtained record energy of 6.2 mJ total (4.2 mJ of 1<sup>st</sup> Stokes at 573 nm and 2 mJ of 2<sup>nd</sup> Stokes at 620 nm) was for 12.3 mJ of pumping. The total efficiency was 55% and the corresponding conversion efficiency was around 50% for this case. The minimum 1<sup>st</sup> Stokes pulse of 2 ns and 2<sup>nd</sup> Stokes pulse of 0.7 ns was detected near the threshold of 0.6 mJ and 1.5 mJ, respectively. Similarly, the slope efficiencies of 5% and 10% were measured for the cavities that provided two passes for the 573 nm and one and two passes, respectively, for the pump.

Lasing was tested for the single-pass Raman at normal and non-normal incidence to see the evidence of possible amplification due to backscattering and distributed feedback geometries. For the normal incidence, the efficiency of 573 nm output in forward and backward is essentially the same (1.5%). Also, we detected the minimum pulse duration of 420 ps and 500 ps, respectively, for Raman pulse in backward and forward for 5.2 mJ pump. That suggests no evidence of pulse compression and signal amplification because of two counter-propagating laser pulses (pump and the Stokes) and, hence, no backscattered stimulated Raman process. However, ~20-fold pulse shortening (420 ps of output under 8.5 ns of the pump) is very important and such systems can be used as seed sources for multistage amplifiers. For the single-pass Raman laser at non-normal incidence (angle of incidence 32 degrees), we obtained 15% slope efficiency without any external feedback mirror. For further verification similar sample with mismatched facets was tested and obtained no output in this case. Given the fact that 15% efficiency is higher than that compared to that for a single-pass at normal incidence and no output for the sample with

wedged facets indicates that there was positive feedback due to distributed gain but not sufficient for reaching the threshold for the given sample. The other samples with longer lengths and bigger input facets could provide sufficient feedback and gain to be above the threshold. In almost all cases, we observed a significant near-threshold pulse shortening. The pulse duration increased with the increase of the input pump power and start to feature multiple peaks and overall larger pulse durations due to multimode oscillations.

## CHAPTER 5

### CONCLUSIONS

#### 5.1 Summary of the Results and Conclusions

The following is the summary of the experiments conducted.

We have measured absorption and emission spectra of  $NV^-$  centers in CVD grown diamond samples at room temperature and estimated the absorption and emission cross-sections to be  $2.8 \times 10^{-17} \text{ cm}^2$  and  $4.3 \times 10^{-17} \text{ cm}^2$  at the maximum of absorption and emission bands, respectively, which is in a close agreement with values documented in the literature. We observed the appearance of ZPL of  $NV^0$  at 575nm along with a broad PSB under pulsed excitation due to photoionization of  $NV^-$  to  $NV^0$ . We also estimated the decay lifetime of the excited state of  $NV^-$  to be 12 ns from PL kinetics at room temperature.

Saturated transmission of 532 nm pump pulse is only ~10% even at energy flux much higher than saturation level. There was no induced long-term bleaching of the centers. In a pump-probe experiment, the transmission kinetics at 632 nm reveal a “fast” decay process with recovery time ~250 ns and a “slow” decay process with recovery time ~12  $\mu\text{s}$ . On the other hand, only a “slow” (recovery time 24  $\mu\text{s}$ ) decay channel appears in the kinetics of transmission at 670 nm. This indicates different decay channels involved after photoionization of  $NV^-$  centers under green excitation. Centers recover to the steady-state level between the pulses showing no residual absorption or long-lived bleaching for a 10Hz repetition rate. We did not detect long-lived photoionization or bleaching of the centers after irradiating under a large 532 nm pump

density. Transmission saturates to ~48% under 633 nm pump, which was much better saturation than that under 532nm pumping. Pumping at 633 nm with sufficiently high intensity leads to the accumulation of electrons in the metastable state of the NV<sup>0</sup> center resulting in higher saturation of transmission. We set up a resonator using a polished facet of the sample and gold-plated concave mirror and measured spectral profile at different intensities. We did not measure the notable change in FWHM of the emission band. That implies the population of the excited state of NV<sup>-</sup> is still small since we do not see the stimulated process or lasing. However, additional experiments are required to estimate the ratio of excited and ionized color centers.

Detailed spectroscopic characterization of GR1 centers in diamond was performed and spectroscopic parameters associated with <sup>1</sup>E↔<sup>1</sup>T<sub>2</sub> transitions were explored. Additional absorption bands with a maximum of around 480 nm (di-vacancy TH5) and 350 nm (negative vacancy ND1) were observed. GR1 absorption extends from 500 nm to 780 nm and partially overlaps with the TH5 absorption band. The overlapping of GR1 and TH5 absorption becomes more noticeable after thermal annealing. Thermal annealing results in the decrease of the GR1 absorption which is accompanied by the increase in TH5 absorption which was exploited to extract the true shape of the GR1 absorption band. Emission spectra ranging from 720 nm to 1100 nm were collected under 633 nm pulsed excitation.

The saturation measurements of the GR1 center show an increase in the transmission (after adjusting for Fresnel reflection) from 55% to 83%. The saturation energy fluence obtained after fitting is 6 mJ/cm<sup>2</sup>. Also estimated radiative lifetime and quantum yield are about 7.8 ns and 14%, correspondingly. The absorption and emission cross-sections were calculated to be  $4.5 \times 10^{-17} \text{ cm}^2$  and  $7.6 \times 10^{-17} \text{ cm}^2$  at the maxima

of vibronic bands at 630 nm and 760 nm, respectively. We here demonstrated excellent saturation of 633 nm pump with low saturation intensity and high transmission modulation depth. We presented the results associated with the characterization of NV centers in international conferences like *SPIE PW 2018* [113], *ASSL 2018* [114], and published them in digital libraries of respective conferences. Later, all the results were combined and published in *Optical Material Express* [47].

Pump and probe experiments were performed for two samples, which had very high and very low GR1 concentrations, and the pump-induced change in CW probe beam transmission was measured. For the LD sample, the saturation spike at the beginning of kinetics followed by a slow relaxation to the initial stage with a lifetime of 220  $\mu\text{s}$ . The amplitude of the initial spikes is approximately the same as the amplitude of slow relaxation. It indicates that the relaxation from the  $^1\text{T}_2$  state occurs predominantly via the metastable state. After initial saturation, an induced absorption with a rise time of 44  $\mu\text{s}$  was followed by a non-exponential decay with a lifetime close to several milliseconds. The induced absorption was bigger than the ground state absorption. We have demonstrated that there are no indications of photoionization of GR1 centers at 658 nm for GR1 with pump energy fluence up to 500  $\text{mJ}/\text{cm}^2$ . After excitation to  $^1\text{T}_2$  level, the relaxation occurs predominately via metastable level with a lifetime of 220  $\mu\text{s}$ . Two-step photoionization was observed at 532 nm from the  $^1\text{T}_2$  level of GR1 centers. Different decay times of the induced absorptions at 532 nm and 658 nm in the HD sample and the absence of induced absorption at 658 nm in the LD sample suggest the photoionization of different impurity centers with absorption peaks around 480 nm and 350 nm.

Several experiments were carried out to test the lasing in GR1 centers under ns-pulsed 633 nm excitation using different linear cavity schemes (collinear for normal and Brewster incidence, quasi-collinear, and transverse pumping). No sign of lasing was detected in all experiments. However, we utilized a LiF:F<sub>2</sub><sup>+\*</sup> color center crystal (fabricated more than 20 years ago) in the same cavity setup which was used for GR1 centers. We demonstrated a strong laser oscillation near 920 nm with small lasing threshold. It suggests that the experimental setup was capable to meet the lasing condition and additional optimization of GR1 centers concentration might be required for lasing. Laser-spectroscopic characterization of LiF:F<sub>2</sub><sup>+\*</sup> samples also revealed the longtime stability of the F<sub>2</sub><sup>+\*</sup> centers. After more than 20 years of storage at room temperature, these centers are still capable to lase with only small degradation of the center's concentrations.

Fabrication of laser gain media based on GR1 centers in diamonds requires special optimization of the center concentration and crystal parameters to minimize the induced absorption at lasing wavelengths. This result indicates that these centers could be used as gain media or passive Q-switchers for laser cavities operating in a pulsed regime over the 550 - 750 nm spectral range (such as Alexandrite laser, Titanium Sapphire, Ruby lasers). The results associated with GR1 centers characterization were presented in SPIE 2020, ASSL 2020, 2021, and CLEO 2021 [115–117] and later published in *Optical Material Express* [118].

Diamond Raman lasing in different cavities and pumping schemes was realized. For the plane-plane resonator containing HR and 65% OC at the 1<sup>st</sup> and 2<sup>nd</sup> Stokes wavelengths, the total output energy of 6.2 mJ was demonstrated at 12.3 mJ of pump energy. The total conversion efficiency was 51%. Output Raman pulses as short as 2 ns

and 0.7 ns were detected near thresholds for the 1<sup>st</sup> and 2<sup>nd</sup> Stokes. For the double pass Raman amplification, the slope efficiencies of 10% and 5%, respectively, were measured for cavities allowing double pass and single pass for the pump. The smallest pulse duration of 1 ns was measured in a single pulse. For a single pass at normal incidence near the threshold, the 1<sup>st</sup> Stokes was 20  $\mu$ J (2 ns) energy for 600  $\mu$ J (8.2 ns) pump. In a single pass setup, the smallest 1<sup>st</sup> Stokes pulse duration of 420 ps was realized in the backward direction for 8.2 ns of pumping, which corresponds to ~20-fold shortening. The slope efficiency was 1.5% in this case. The output pulse was shortened to the picosecond scale, however, the output pulse duration increased with the increase of the input pump power. At non-normal pump incidence, the efficiency was almost 5 times higher than that for normal incidence single pass. Upon comparing the performance of two similar samples one with parallel and the other one with wedged facets, we concluded that the feedback by the creation of wavelength-selective gain grating and surface reflection partially contributed to the higher efficiency (5 times). This work was presented in SPIE PW 2021 [119].

## 5.2 Future implementation

The NV centers have shown strong photoionization which rate for ns-pulse excitation depends on both intensity and the pumping wavelength with the recovery time is several hundreds of nanoseconds. In the future, picosecond pulse excitation at a suitable wavelength and in low temperature at which photoionization is smaller can be tested for laser oscillation.

GR1 centers possess a high absorption cross-section and small saturation intensity. We have demonstrated excellent saturation of absorption of GR1 centers

under 633 nm pump pulses (4.2 ns at 10 Hz). GR1 centers in a diamond can serve as excellent saturable absorbers and can be used for passive Q-switching of cavities of solid-state lasers operating over 500-750 nm spectral range. In the future, an experiment for Q-switching of Alexandrite laser operating over 725-750 nm spectral range using GR1 centers in diamond as saturable absorber can be carried out. Pump-probe kinetics show that highly concentrated GR1 samples have additional photoionization due to other color centers not associated with the GR1 center. A sample with a suitable GR1 concentration and minimum or apparently no other overlapping color centers can be tested for lasing.

External cavity diamond Raman laser has demonstrated high output energy even with the use of uncoated gain elements with wedged facets. A significant improvement in output energy and beam profile can be achieved for the gain elements with parallel facets in the longitudinal direction and wedged facets in transverse directions. A single-pass Raman output can be used as a seed source for additional amplifier stages and a high-energy output of picosecond 573 nm Raman laser can be realized using a very simple optical setup. Furthermore, narrow bandwidth distributed feedback diamond Raman laser could still be possible with the use of a single crystal diamond sample of longer path length.

## APPENDIX A

### A.1. Calibration of Photoluminescence Spectra

The PL spectra measured in different experimental configurations may differ from the actual shape. The PMTs do not have a constant responsivity and the spectral dependence of the response of the detector should be taken into account. Other components that shift the apparent spectral profiles are the transmission of the dichroic filters and lenses used and monochromator sensitivity at different wavelengths. Since the wavelength of interest for all the experiments is below 1100 nm, we can ignore water-vapor absorption bands due to humidity along with the optical axis environment. To compensate and eliminate this shift, the sensitivity profiles were measured for each experimental and detection configuration.

For the calibration purpose, a 45 W tungsten-filament quartz halogen lamp (Oriel Model # 63358 lamp) supplied as the standard of spectral irradiance for the wide spectral range was used. The supply current used for the lamp was 6.5A which is recommended by Oriel as a standard operating current. Before each measurement, the lamp was turned on for about 20 minutes to 30 minutes to warm up before measurements. The lamp spectrum was measured using the same monochromator setting, grating, and the same combinations of filters, lenses, and detectors that were used to measure the PL spectra. Then the measured lamp spectra ( $L_{Meas}$ ) were compared

with the standard lamp spectra ( $L_{Std}$ ) to obtain calibration factor (C) at each wavelength as follows:

$$C(\lambda) = \frac{L_{Std}(\lambda)}{L_{Meas}(\lambda)} \times T_{Filter}, \quad (i)$$

where  $T_{Filter}$  is the total transmission of the dichroic filters used to block the pump signal for different experiments. These sensitivity curves were used to correct all PL measured spectra using the following relationship;

$$PL_{Std}(\lambda) = PL_{Meas}(\lambda)C(\lambda), \quad (ii)$$

where  $PL_{Std}(\lambda)$  and  $PL_{Meas}(\lambda)$  are the calibrated and measured PL spectra.

#### *A.1.1 NV<sup>-</sup> PL Spectra Calibration*

We employed the above-mentioned procedure to extract the corrected PL spectrum of NV centers under CW excitation. All the spectra utilized for the calculations are depicted in Figure A.1. We can see a non-flat response of the detection platform (PMT 928 and two orange filters) including a monochromator if we compare the measured lamp spectra with the standard lamp spectrum. After calibration, the corrected PL signal of NV centers is shifted further towards the longer wavelength region, however, there is a very small change in the short wavelength side of the emission band.

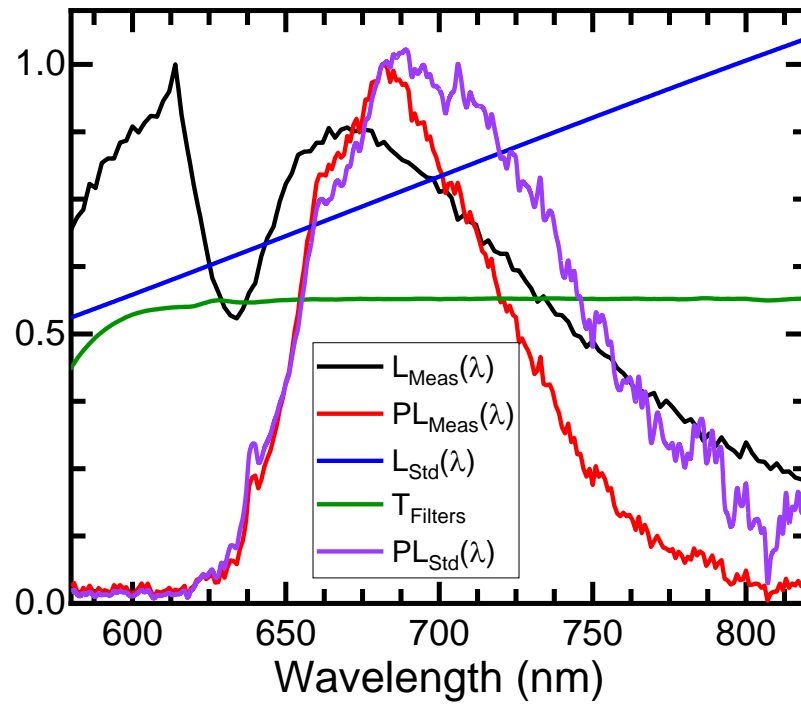


Figure A.1 Graph showing the spectra of the lamp measured (black curve) and standard (blue curve), the total transmission of the two orange filters (green curve), and photoluminescence of the NV centers measured (red curve) and calibrated (purple curve).

### A.1.2 GR1 PL spectra calibration

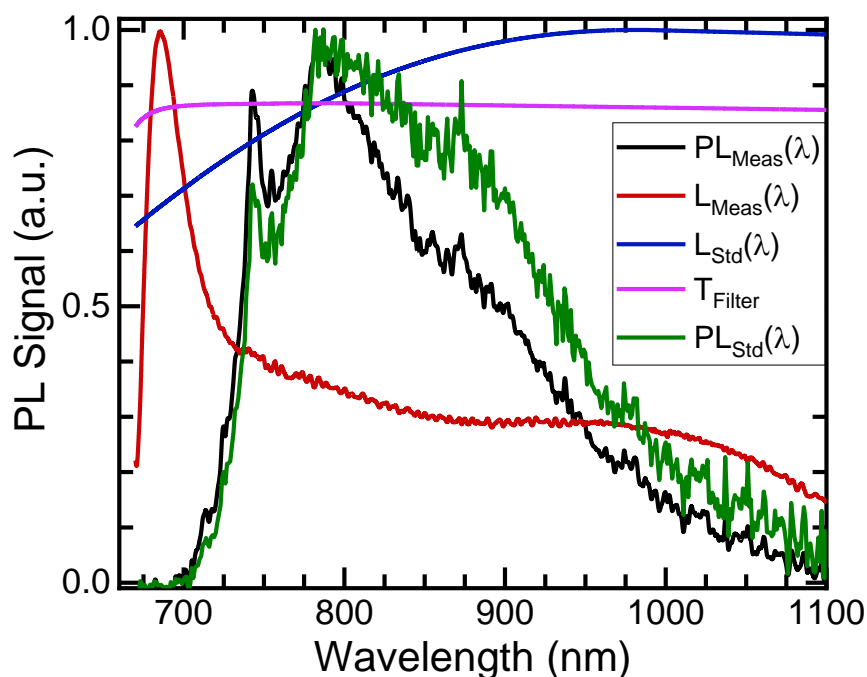


Figure A.2 Graph showing the spectra of the lamp measured (red curve) and standard (blue curve), the transmission of the filter (pink curve), and photoluminescence of the GR1 centers measured (black curve) and calibrated (green curve).

A very similar procedure was carried out to calculate the corrected PL spectrum of the GR1 centers and all the spectra are presented in Figure A.2. In this case, the lamp spectrum was measured in the same arrangement that was used to measure GR1 PL spectra. The signal was collected at the entrance of the fiber cable and directed to the monochromator PMT R5108 combination. A dichroic red filter was used to block the pump and its spectrum is shown by the pink curve in Figure A.2. In this case, the calibrated PL spectrum of GR1 centers has slightly increased bandwidth.

## LIST OF REFERENCES

1. P. E. Barclay, K.-M. Fu, F. Jelezko, and M. Loncar, "Diamond photonics: introduction," *J. Opt. Soc. Am. B* **33**(4), DP1 (2016).
2. B. J. M. Hausmann, I. Bulu, V. Venkataraman, P. Deotare, and M. Loncar, "Diamond nonlinear photonics," *Nat. Photonics* **8**(5), 369–374 (2014).
3. J. Nikkinen, S. Reilly, V. Savitski, A. Härkönen, A. Kemp, and M. Guina, "Yellow picosecond diamond raman laser," in *Optics InfoBase Conference Papers* (2017), **Part F82-C**, p. paper CA\_11\_1.
4. M. Seal and W. J. P. van Enkevort, "Applications Of Diamond In Optics," in *Diamond Optics* (SPIE, 1989), **0969**, p. 144.
5. A. M. Zaitsev, *Optical Properties of Diamond: A Data Handbook* (Springer Verlag, 2001).
6. P. Kehayias, "Exploring Basic Properties and Applications of Nitrogen-Vacancy Color Centers in Diamond," University of California, Berkeley Committee (2015).
7. K. Iakoubovskii, G. J. Adriaenssens, and M. Nesladek, "Photochromism of vacancy-related centres in diamond," *J. Phys. Condens. Matter* **12**(2), 189–199 (2000).
8. J. Walker, "Optical absorption and luminescence in diamond," *Reports Prog. Phys.* **42**(10), 1605–1659 (1979).
9. C. D. Clark and J. Walker, "The neutral vacancy in diamond," in *Proceedings of the Royal Society of London. A. Mathematical and Physical Sciences* (1973), **334**(1597), pp. 241–257.

10. Y. Mita, Y. Nisida, K. Suito, A. Onodera, and S. Yazu, "Photochromism of H2 and H3 centres in synthetic type Ib diamonds," *J. Phys. Condens. Matter* **2**(43), 8567–8574 (1990).
11. L. F. Bruce, M. G. Kopylova, M. Longo, J. Ryder, and L. F. Dobrzhinetskaya, "Luminescence of diamonds from metamorphic rocks," *Am. Mineral.* **96**(1), 14–22 (2011).
12. V. Acosta and P. Hemmer, "Nitrogen-vacancy centers: Physics and applications," *MRS Bull.* **38**(2), 127–130 (2013).
13. W. Lubeigt, G. M. Bonner, J. E. Hastie, M. D. Dawson, D. Burns, and A. J. Kemp, "Continuous-wave diamond Raman laser," *Opt. Lett.* **35**(17), 2994 (2010).
14. S. Reilly, "Characterisation and Implementation of Synthetic Diamond as a Raman Laser Material," University of Strathclyde (2015).
15. J. E. Lowther, "The form of different charge states of the vacancy in diamond," *J. Phys. Chem. Solids* **45**(2), 127–131 (1984).
16. S. J. Breuer and P. R. Briddon, "Ab initio investigation of the native defects in diamond and self-diffusion," *Phys. Rev. B* **51**(11), 6984–6994 (1995).
17. B. Henderson and R. H. Bartram, *Crystal-Field Engineering of Solid-State Laser Materials* (Cambridge University Press, 2000).
18. R. J. Williams, O. Kitzler, Z. Bai, S. Sarang, H. Jasbeer, A. McKay, S. Antipov, A. Sabella, O. Lux, D. J. Spence, and R. P. Mildren, "High Power Diamond Raman Lasers," *IEEE J. Sel. Top. Quantum Electron.* **24**(5), 1–14 (2018).
19. P. Millar, A. J. Kemp, F. van Loon, A. J. Maclean, and D. Burns, "Synthetic diamond as an intracavity heatspreader in compact solid-state lasers," in *2007 European Conference on Lasers and Electro-Optics and the International Quantum*

*Electronics Conference* (IEEE, 2007), pp. 1–1.

20. A. K. McQuillan, W. R. L. Clements, and B. P. Stoicheff, "Stimulated Raman emission in diamond: Spectrum, gain, and angular distribution of intensity," *Phys. Rev. A* **1**(3), 628–635 (1970).
21. G. Eckhardt, D. P. Bortfeld, and M. Geller, "Stimulated emission of stokes and anti-stokes raman lines from diamond, calcite, and -sulfur single crystals," *Appl. Phys. Lett.* **3**(8), 137–138 (1963).
22. A. A. Kaminskii, V. G. Ralchenko, and V. I. Konov, "Observation of stimulated raman scattering in CVD-diamond," *JETP Lett.* **80**(4), 267–270 (2004).
23. A. A. Demidovich, A. S. Grabtchihov, V. A. Orlovich, M. B. Danailov, and W. Kiefer, "Diode pumped diamond Raman microchip laser," in *Conference on Lasers and Electro-Optics Europe - Technical Digest* (2005), p. 251.
24. R. P. Mildren, J. E. Butler, and J. R. Rabeau, "CVD-diamond external cavity Raman laser at 573 nm," *Opt. Express* **16**(23), 18950 (2008).
25. R. P. Mildren and A. Sabella, "Highly efficient diamond Raman laser," *Opt. Lett.* **34**(18), 2811 (2009).
26. A. Sabella, J. A. Piper, and R. P. Mildren, "1240 nm diamond Raman laser operating near the quantum limit," *Opt. Lett.* **35**(23), 3874 (2010).
27. J.-P. M. Feve, K. E. Shortoff, M. J. Bohn, and J. K. Brasseur, "High average power diamond Raman laser," *Opt. Express* **19**(2), 913 (2011).
28. D. J. Spence, E. Granados, and R. P. Mildren, "Mode-locked picosecond diamond Raman laser," *Opt. Lett.* **35**(4), 556 (2010).
29. J. Nikkinen, V. Savitski, S. Reilly, L. Dziechciarzyk, A. Harkonen, A. Kemp, and M. Guina, "Sub-100 ps monolithic diamond raman laser emitting at 573 nm," *IEEE*

- Photonics Technol. Lett. **30**(11), 981–984 (2018).
30. A. M. Warriar, J. Lin, H. M. Pask, R. P. Mildren, D. W. Coutts, and D. J. Spence, "Highly efficient picosecond diamond Raman laser at 1240 and 1485 nm," *Opt. Express* **22**(3), 3325 (2014).
  31. M. Murtagh, J. Lin, R. P. Mildren, G. McConnell, and D. J. Spence, "Efficient diamond Raman laser generating 65 fs pulses," *Opt. Express* **23**(12), 15504 (2015).
  32. W. Lubeigt, V. G. Savitski, G. M. Bonner, S. L. Geoghegan, I. Friel, J. E. Hastie, M. D. Dawson, D. Burns, and A. J. Kemp, "1.6 W continuous-wave Raman laser using low-loss synthetic diamond," *Opt. Express* **19**(7), 6938 (2011).
  33. O. Kitzler, A. McKay, and R. P. Mildren, "Continuous-wave wavelength conversion for high-power applications using an external cavity diamond Raman laser," *Opt. Lett.* **37**(14), 2790 (2012).
  34. S. Antipov, A. Sabella, S. Sarang, R. J. Williams, D. J. Spence, and R. P. Mildren, "A 900-watt quasi-CW diamond Raman laser," in *Optics InfoBase Conference Papers* (OSA, 2018), **Part F113-**, p. Th4D.6.
  35. M. Li, P. Li, X. Zhang, and X. Chen, "21.8 W CW second-Stokes CVD-diamond Raman laser at 1516 nm," *Appl. Phys. B Lasers Opt.* **124**(8), (2018).
  36. S. Antipov, A. Sabella, R. J. Williams, O. Kitzler, D. J. Spence, and R. P. Mildren, "1.2 kW quasi-steady-state diamond Raman laser pumped by an M2 = 15 beam," *Opt. Lett.* **44**(10), 2506 (2019).
  37. S. C. Rand and L. G. DeShazer, "Visible color-center laser in diamond," *Opt. Lett.* **10**(10), 481 (1985).
  38. T. Nakashima and S. Yazu, "Optical properties and laser action of H3 center in synthetic diamond," in *Proceedings Volume 1325, Diamond Optics III* (1990),

(December 1990), pp. 10–16.

39. V. P. Mironov, E. F. Martinovich, and V. A. Grigorov, "Laser materials based on diamond with GR1 centers," *Diam. Relat. Mater.* **3**(4–6), 936–938 (1994).
40. J. Jeske, D. W. M. Lau, X. Vidal, L. P. McGuinness, P. Reineck, B. C. Johnson, M. W. Doherty, J. C. McCallum, S. Onoda, F. Jelezko, T. Ohshima, T. Volz, J. H. Cole, B. C. Gibson, and A. D. Greentree, "Stimulated emission from nitrogen-vacancy centres in diamond," *Nat. Commun.* **8**(:14000), (2017).
41. S. Raman Nair, L. J. Rogers, X. Vidal, R. P. Roberts, H. Abe, T. Ohshima, T. Yatsui, A. D. Greentree, J. Jeske, and T. Volz, "Amplification by stimulated emission of nitrogen-vacancy centres in a diamond-loaded fibre cavity," *Nanophotonics* **9**(15), 4505–4518 (2020).
42. E. Fraczek, V. G. Savitski, M. Dale, B. G. Breeze, P. Diggle, M. Markham, A. Bennett, H. Dhillon, M. E. Newton, and A. J. Kemp, "Laser spectroscopy of NV- and NV0 colour centres in synthetic diamond," *Opt. Mater. Express* **7**(7), 2571 (2017).
43. J. Anderegg, "Multiwatt visible lasers," in *SPIE Newsroom* (2010).
44. K. Beha, A. Batalov, N. B. Manson, R. Bratschitsch, and A. Leitenstorfer, "Optimum photoluminescence excitation and recharging cycle of single nitrogen-vacancy centers in ultrapure diamond," *Phys. Rev. Lett.* **109**(9), 1–5 (2012).
45. N. B. Manson and J. P. Harrison, "Photo-ionization of the nitrogen-vacancy center in diamond," *Diam. Relat. Mater.* **14**(10), 1705–1710 (2005).
46. J. Lin and D. J. Spence, "Diamond raman laser generating 25.5 fs pulses," in *Advanced Solid State Lasers, ASSL 2015* (2015).
47. S. D. Subedi, V. V. Fedorov, J. Peppers, D. V. Martyshkin, S. B. Mirov, L. Shao,

- and M. Loncar, " Laser spectroscopic characterization of negatively charged nitrogen-vacancy (NV<sup>-</sup>) centers in diamond ," *Opt. Mater. Express* **9**(5), 2076 (2019).
48. M. Zhang, B. Y. Li, and J. Liu, "Monitoring dark-state dynamics of a single nitrogen-vacancy center in nanodiamond by auto-correlation spectroscopy: Photonionization and recharging," *Nanomaterials* **11**(4), (2021).
  49. Á. Gali, "Ab initio theory of the nitrogen-vacancy center in diamond," *Nanophotonics* **8**(11), 1907–1943 (2019).
  50. P. Siyushev, H. Pinto, M. Vörös, A. Gali, F. Jelezko, and J. Wrachtrup, "Optically controlled switching of the charge state of a single nitrogen-vacancy center in diamond at cryogenic temperatures," *Phys. Rev. Lett.* **110**(16), (2013).
  51. A. Gruber, A. Dräbenstedt, C. Tietz, L. Fleury, J. Wrachtrup, and C. Von Borczyskowski, "Scanning confocal optical microscopy and magnetic resonance on single defect centers," *Science* (80-. ). **276**(5321), 2012–2014 (1997).
  52. F. Pedroza-Montero, K. Santacruz-Gómez, M. Acosta-Elías, E. Silva-Campa, D. Meza-Figueroa, D. Soto-Puebla, B. Castaneda, E. Urrutia-Bañuelos, O. Álvarez-Bajo, S. Navarro-Espinoza, R. Riera, and M. Pedroza-Montero, "Thermometric Characterization of Fluorescent Nanodiamonds Suitable for Biomedical Applications," *Appl. Sci.* **11**(9), 4065 (2021).
  53. N. Aslam, G. Waldherr, P. Neumann, F. Jelezko, and J. Wrachtrup, "Photo-induced ionization dynamics of the nitrogen vacancy defect in diamond investigated by single-shot charge state detection," *New J. Phys.* **15**, (2013).
  54. L. J. Rogers, M. W. Doherty, M. S. J. Barson, S. Onoda, T. Ohshima, and N. B. Manson, "Singlet levels of the NV<sup>-</sup> centre in diamond," *New J. Phys.* **17**(1), 13048 (2015).

55. S. Rand, "Synthetic Diamond for Color Center Lasers," in *Tunable Solid-State Lasers II: Springer Series in Optical Sciences* (Springer, Berlin, Heidelberg, 2017), pp. 276–280.
56. A. T. Collins, M. F. Thomaz, and M. I. B. Jorge, "Luminescence decay time of the 1.945 eV centre in type Ib diamond," *J. Phys. C Solid State Phys.* **16**(11), 2177–2181 (1983).
57. E. Bourgeois, A. Jarmola, P. Siyushev, M. Gulka, J. Hruby, F. Jelezko, D. Budker, and M. Nesladek, "Photoelectric detection of electron spin resonance of nitrogen-vacancy centres in diamond," *Nat. Commun.* **6**, (2015).
58. L. Hacquebard and L. Childress, "Charge-state dynamics during excitation and depletion of the nitrogen-vacancy center in diamond," *Phys. Rev. A* **97**(6), (2018).
59. L.-T. S. Lin, M. A. Prelas, and G. Popovici, "Laser Modes in Diamond," in *Wide Band Gap Electronic Materials* (1995), pp. 187–206.
60. F. Jelezko, C. Tietz, A. Gruber, I. Popa, A. Nizovtsev, S. Kilin, and J. Wrachtrup, "Spectroscopy of single N-V centers in diamond," *Single Mol.* **2**(4), (2001).
61. E. Fraczek, V. G. Savitski, M. Dale, B. G. Breeze, P. Diggle, M. Markham, A. Bennett, H. Dhillon, M. E. Newton, and A. J. Kemp, "Laser spectroscopy of NV- and NV0 colour centres in synthetic diamond," *Opt. Mater. Express* **7**(7), 2571 (2017).
62. V. G. Vins and E. V. Pestryakov, "Color centers in diamond crystals: Their potential use in tunable and femtosecond lasers," *Diam. Relat. Mater.* **15**(4–8), 569–571 (2006).
63. O. Shenderova and D. M. Gruen, *Ultrananocrystalline Diamond: Synthesis, Properties, and Applications of UNCD*, 2nd ed. (Elsevier, Oxford, UK, 2006).

64. H.-C. Lu, Y.-C. Peng, M.-Y. Lin, S.-L. Chou, J.-I. Lo, and B.-M. Cheng, "Photoluminescence of a CVD Diamond Excited with VUV Light from a Synchrotron," *Opt. Photonics J.* **03**(06), 25–28 (2013).
65. C. C. Davis, *Lasers and Electro-Optics, Second Edition* (Cambridge University Press, 2013).
66. T. L. Wee, Y. K. Tzeng, C. C. Han, H. C. Chang, W. Fann, J. H. Hsu, K. M. Chen, and E. C. Yu, "Two-photon excited fluorescence of nitrogen-vacancy centers in proton-irradiated type Ib diamond," *J. Phys. Chem. A* **111**(38), 9379–9386 (2007).
67. V. M. Acosta, A. Jarmola, E. Bauch, and D. Budker, "Optical properties of the nitrogen-vacancy singlet levels in diamond," *Phys. Rev. B - Condens. Matter Mater. Phys.* **82**(20), 1–5 (2010).
68. W. Koechner, *Solid-State Laser Engineering - 6th Edition* (2014).
69. A. G. Mathewson and H. P. Myers, "The optical absorption of the neutral vacancy in diamond," *J. Phys. C Solid State Phys.* **5**(17), 2503–2510 (1972).
70. S. Eaton-Magaña, "Comparison of luminescence lifetimes from natural and laboratory irradiated diamonds," *Diam. Relat. Mater.* **58**, 94–102 (2015).
71. J. C. A. Prentice, B. Monserrat, and R. J. Needs, "First-principles study of the dynamic Jahn-Teller distortion of the neutral vacancy in diamond," *Phys. Rev. B* **95**(1), (2017).
72. C. A. Coulson and F. P. Larkins, "Isolated single vacancy in diamond-I. Electronic structure," *J. Phys. Chem. Solids* **32**(9), 2245–2257 (1971).
73. J. E. Lowther, "Jahn-Teller coupling at ND1 and GR1 centres in diamond," *J. Phys. C Solid State Phys.* **11**(9), 3–6 (1978).
74. A. M. Stoneham, "The low-lying levels of the GR 1 centre in diamond," *Solid State*

- Commun. **21**(4), 339–341 (1977).
75. M. Lannoo and A. M. Stoneham, "The optical absorption of the neutral vacancy in diamond," *J. Phys. Chem. Solids* **29**(11), 1987–2000 (1968).
  76. A. T. Collins, "Fine structure in the GR1 cathodoluminescence from natural semiconducting diamond," *J. Phys. C Solid State Phys.* **11**(12), 2453–2463 (1978).
  77. G. Davies and A. T. Collins, "Vacancy complexes in diamond," *Diam. Relat. Mater.* **2**(2–4), 80–86 (1993).
  78. A. T. Collins, "High-resolution luminescence-excitation spectra of the GR defect in diamond," *J. Phys. C Solid State Phys.* **14**(3), 289–294 (1981).
  79. A. T. Collins, J. Szechi, and S. Tavender, "Resonant excitation of the GR centre in diamond," *J. Phys. C Solid State Phys.* **21**(7), L161–L164 (1988).
  80. G. Davies, M. F. Thomazs, M. H. Nazares, M. Martin, and D. Shaw, "Vacancy in Diamond," **13**, 1–6 (1987).
  81. S. D. Subedi, V. V. Fedorov, J. Peppers, D. V. Martyshkin, S. B. Mirov, L. Shao, and M. Loncar, "Laser spectroscopic characterization of negatively charged nitrogen-vacancy (NV<sup>-</sup>) centers in diamond," *Opt. Mater. Express* **9**(5), 2076 (2019).
  82. E. Fritsch and K. V. G. Scarratt, "Optical Properties Of Some Natural Diamonds With High Hydrogen Content," in *Diamond Optics II* (1990), **1146**, p. 201.
  83. H. B. Dyer and L. D. U. Preez, "Irradiation damage in type I diamond," *J. Chem. Phys.* **42**(6), 1898–1906 (1965).
  84. H. B. Dyer and P. Ferdinando, "The optical absorption of electron-irradiated semiconducting diamond," *Br. J. Appl. Phys.* **17**(3), 419–420 (1966).

85. L. S. Hounsome, R. Jones, P. M. Martineau, M. J. Shaw, P. R. Briddon, S. Öberg, A. T. Blumenau, and N. Fujita, "Optical properties of vacancy related defects in diamond," in *Physica Status Solidi (A) Applications and Materials Science* (John Wiley & Sons, Ltd, 2005), **202**(11), pp. 2182–2187.
86. P. Deák, B. Aradi, M. Kaviani, T. Frauenheim, and A. Gali, "Formation of NV centers in diamond: A theoretical study based on calculated transitions and migration of nitrogen and vacancy related defects," *Phys. Rev. B - Condens. Matter Mater. Phys.* **89**(7), 1–20 (2014).
87. J. M. Baker, D. C. Hunt, M. E. Newton, and D. J. Twitchen, "Centres involving two vacancies in diamond," *Radiat. Eff. Defects Solids* **149**(1–4 pt 1), 233–237 (1999).
88. M. A. Lea-Wilson, J. N. Lomer, and J. A. Van Wyk, "Electron spin resonance of the R4/W6 defect in irradiated diamond," *Philos. Mag. B Phys. Condens. Matter; Stat. Mech. Electron. Opt. Magn. Prop.* **72**(1), 81–89 (1995).
89. G. Davies, M. F. Thomazs, M. H. Nazares, M. Martin, and D. Shaw, "The radiative decay time of luminescence from the vacancy in diamond," *J. Phys. C Solid State Phys.* **20**, 1–6 (1987).
90. M. Hercher, "An Analysis of Saturable Absorbers," *Appl. Opt.* **6**(5), 947 (1967).
91. Z. Burshtein, P. Blau, Y. Kalisky, Y. Shimony, and M. R. Kokta, "Excited-state absorption studies of Cr<sup>4+</sup> ions in several garnet host crystals," *IEEE J. Quantum Electron.* **34**(2), 292–299 (1998).
92. L. M. Frantz and J. S. Nodvik, "Theory of pulse propagation in a laser amplifier," *J. Appl. Phys.* **34**(8), 2346–2349 (1963).
93. O. Svelto, *Principles of Lasers*, 5th ed. (Springer, 2010).
94. S. A. Payne, L. L. Chase, L. K. Smith, W. L. Kway, and W. F. Wyers, "Infrared

- Cross-Section Measurements for Crystals Doped with  $\text{Er}^{3+}$ ,  $\text{Tm}^{3+}$ , and  $\text{Ho}^{3+}$ ," IEEE J. Quantum Electron. **28**(11), 2619–2630 (1992).
95. G. Liaugaudas, A. T. Collins, K. Suhling, G. Davies, and R. Heintzmann, "Luminescence-lifetime mapping in diamond," J. Phys. Condens. Matter **21**(36), (2009).
  96. S. B. Mirov and A. Y. Dergachev, "Powerful room-temperature stable  $\text{LiF:F}_2^{+**}$  tunable laser," in *Solid State Lasers VI* (1997), **2986**(March 1997), p. 162.
  97. A. G. V. Spivey, V. V. Fedorov, M. M. McKerns, C. M. Lawson, and S. B. Mirov, "Amplification of narrow line  $\text{LiF:F}_2^{+**}$  color center laser oscillation," Opt. Commun. **254**(4–6), 290–298 (2005).
  98. V. V. Ter-Mikirtychev, "Stable, efficient room-temperature  $\text{LiF:F}_2^{+**}$  laser, tunable in the 820-1200 nm region, pumped by a  $\text{YAG:Nd}^{3+}$  laser with an injection seeded solid-state wavelength convertor," Opt. Laser Technol. **30**(3–4), 229–233 (1998).
  99. S. Ma, H. Tu, D. Lu, Z. Hu, N. Jiang, X. Wang, and J. Wang, "Efficient Raman red laser with second-order stokes effect of diamond crystal," Opt. Commun. **478**, 126399 (2021).
  100. D. V. Martyshkin, J. G. Parker, V. V. Fedorov, and S. B. Mirov, "Tunable distributed feedback color center laser using stabilized  $\text{F}_2^{+**}$  color centers in LiF crystal," Appl. Phys. Lett. **84**(16), (2004).
  101. A. Y. Dergachev and S. B. Mirov, "Efficient room temperature  $\text{LiF:F}_2^{+**}$  color center laser tunable in 820-1210 nm range," Opt. Commun. **147**(1–3), 107–111 (1998).
  102. J. Reintjes, R. H. Lehmberg, R. S. F. Chang, M. T. Duignan, and G. Calame, "Beam cleanup with stimulated Raman scattering in the intensity-averaging regime," J. Opt. Soc. Am. B **3**(10), 1408 (1986).

103. J.-P. M. Feve, K. E. Shortoff, M. J. Bohn, and J. K. Brasseur, "High average power diamond Raman laser," *Opt. Express* **19**(2), 913 (2011).
104. C. Moelle, S. Klose, F. Szücs, H. J. Fecht, C. Johnston, P. R. Chalker, and M. Werner, "Measurement and calculation of the thermal expansion coefficient of diamond," *Diam. Relat. Mater.* **6**(5–7), 839–842 (1997).
105. J. R. Olson, R. O. Pohl, J. W. Vandersande, A. Zoltan, T. R. Anthony, and W. F. Banholzer, "Thermal conductivity of diamond between 170 and 1200 K and the isotope effect," *Phys. Rev. B* **47**(22), 14850–14856 (1993).
106. T. Ruf, M. Cardona, C. S. J. Pickles, and R. Sussmann, "Temperature dependence of the refractive index of diamond up to 925 K," *Phys. Rev. B - Condens. Matter Mater. Phys.* **62**(24), 16578–16581 (2000).
107. A. A. Demidovich, A. S. Grabtchikov, V. A. Lisinetskii, V. N. Burakevich, V. A. Orlovich, and W. Kiefer, "Continuous-wave Raman generation in a diode-pumped Nd<sup>3+</sup>:KGd(WO<sub>4</sub>)<sub>2</sub> laser," *Opt. Lett.* **30**(13), 1701 (2005).
108. R. P. Mildren, J. E. Butler, and J. R. Rabeau, "CVD-diamond external cavity Raman laser at 573 nm," *Opt. Express* **16**(23), 18950 (2008).
109. Y. F. Chen, "Compact efficient self-frequency Raman conversion in diode-pumped passively Q-switched Nd:GdVO<sub>4</sub> laser," *Appl. Phys. B Lasers Opt.* **78**(6), 685–687 (2004).
110. Y. Li, Z. Bai, H. Chen, D. Jin, X. Yang, Y. Qi, J. Ding, Y. Wang, and Z. Lu, "Eye-safe diamond Raman laser," *Results Phys.* **16**, 102853 (2020).
111. T. T. Basiev, A. A. Sobol, P. G. Zverev, V. V. Osiko, and R. C. Powell, "Comparative spontaneous Raman spectroscopy of crystals for Raman lasers," *Appl. Opt.* **38**(3), 594 (1999).

112. H. Kogelnik and C. V. Shank, "Coupled-wave theory of distributed feedback lasers," *J. Appl. Phys.* **43**(5), 2327–2335 (1972).
113. S. Subedi, J. Peppers, S. B. Mirov, V. V. Federov, D. V. Martyshkin, L. Shao, and M. Loncar, "Laser spectroscopy of highly doped NV<sup>-</sup> centers in diamond," in *Solid State Lasers XXVII: Technology and Devices; 105112D* (SPIE-Intl Soc Optical Eng, 2018), p. 84.
114. S. D. Subedi, V. V. Fedorov, S. B. Mirov, L. Shao, and M. Loncar, "Saturation spectroscopy of NV<sup>-</sup> centers in diamond," in *Optics InfoBase Conference Papers* (OSA - The Optical Society, 2018), **Part F121**-.
115. S. D. Subedi, V. V. Fedorov, S. Mirov, and M. Markham, "Study of relaxation dynamics of excited state of GR1 centers in diamond," in *Solid State Lasers XXX: Technology and Devices; 116640K* (SPIE-Intl Soc Optical Eng, 2021), p. 15.
116. S. D. Subedi, V. V. Fedorov, S. B. Mirov, and M. Markham, "Nonlinear optical absorption and relaxation kinetics of GR1 centers in diamond," in *Optics InfoBase Conference Papers* (The Optical Society, 2020).
117. S. D. Subedi, V. V. Fedorov, S. Mirov, and M. Markham, "Laser spectroscopic and saturation properties of GR1 centers in synthetic diamond," in *Solid State Lasers XXIX: Technology and Devices; 1125928* (SPIE-Intl Soc Optical Eng, 2020), p. 79.
118. S. Subedi, V. Fedorov, S. Mirov, and M. Markham, "Spectroscopy of GR1 centers in synthetic diamonds," *Opt. Mater. Express* **11**(3), 757 (2021).
119. S. D. Subedi, V. V. Fedorov, S. Mirov, and M. Markham, "Efficient nanosecond diamond Raman laser at 573 nm," in *Solid State Lasers XXX: Technology and Devices; 116640H* (SPIE-Intl Soc Optical Eng, 2021), p. 12.